

DISCLAIMER

The views expressed in this thesis are those of the student and do not necessarily express the views of Aarhus University.

The quality of text and figures are as they were when the thesis was handed in for evaluation. Comments received in the evaluation process have not been incorporated.

Master's thesis

Line Meldgaard Madsen

An analysis of Cole-Cole parameters for time-domain DC and IP data using Markov chain Monte Carlo

Academic advisors:

Esben Auken
Gianluca Fiandaca
Anders Vest Christiansen

Submitted: 01.06.2016

Preface

This master's thesis (45 ECTS) concludes my MSc in Geophysics at Aarhus University, Denmark. The thesis is written in cooperation with the HydroGeophysics Group (HGG) at the Department of Geoscience with supervisors: Esben Auken, Gianluca Fiandaca and Anders Vest Christiansen.

As a supplement to the thesis, a conference abstract presented at the 4th International Workshop on Induced Polarization is enclosed in the back:

Madsen, L. M., Kirkegaard, C., Fiandaca, G., Christiansen, A. V., Auken, E. (2016): An Analysis of Cole-Cole parameters for IP data using Markov chain Monte Carlo. Proceedings for the 4th International Workshop on Induced Polarization, Aarhus, Denmark 2016.

Additionally, an USB stick is handed in, which contains the programming carried out as part of the project.

Department of Geoscience

Aarhus University

01.06.2016

Line Meldgaard Madsen

linemeldgaard@gmail.com

Acknowledgements

I would like to thank my supervisor Esben Auken for introducing me to the field of hydrogeophysics and for the many discussions we have had. I would like to thank my co-supervisor, Anders Vest Christiansen, for his support in the project and for always patiently answering all my questions on the inner working of AarhusInv. I especially wish to stress my gratitude to co-supervisor Gianluca Fiandaca, who with great enthusiasm has introduced me to the world of DCIP and who always has been helpful with ideas and problem solutions.

I am grateful to Casper Kirkegaard for providing me the MCMC algorithm and for passing on his Fortran programming skills and to Thue Sylvester Bording for his assistance with the algorithm and the project in general.

Finally, I thank Rasmus Rune Pedersen and Mads Schmidt Christiansen for their support and interest in the project and my office mates – Helle Holm, Simon Makwarth, Andy Heineth and Thomas Daugbjerg – for many fruitful discussions during our countless coffee breaks.

Abstract

A Markov chain Monte Carlo (MCMC) inversion algorithm is used to make a full nonlinear analysis of spectral Cole-Cole parameters obtained from time-domain direct current (DC) and induced polarization (IP) data. A novel random-walk algorithm samples models from a probability distribution based on a realization of an estimated covariance matrix, which allows the algorithm to vary step lengths according to parameter uncertainty. The novel algorithm converges over one hundred times faster than a standard Metropolis-Hastings algorithm.

Synthetic time-domain DCIP data are inverted using the algorithm. The results show that the Cole-Cole parameters can be resolved from time-domain data and that their posterior probability distributions are unimodal and approximately Gaussian in the logarithmic space. The resolution of the parameters is found to be limited by the applied acquisition range of the IP signal and the values of the chargeability, m_0 , and the frequency exponent, C , which have a direct influence on the signal-to-noise ratio of the IP signal. In the studied models, the Cole-Cole parameters could not be resolved for $m_0 < 10$ mV/V. To obtain useable results, a minimal acquisition range must approximate the standard used at the HydroGeophysics Group, Aarhus University, which is 2.59-4000 ms.

The MCMC studies show that the Cole-Cole parameters are correlated and a strong m_0 - C anti-correlation is observed in most models. The correlations are linear in the logarithmic space for resolved models, but as the resolution decreases, the relations become nonlinear. A comparative analysis of the MCMC results and results from a linearized inversion approach shows that the two methods find equivalent solutions and that a linearized estimated uncertainty analysis is justified for resolved parameters, but when the parameters become unresolved the linearized approach tends to underestimate the uncertainties.

Resume

Ved brug af en Markov chain Monte Carlo (MCMC) algoritme er der lavet en ikke-lineær usikkerhedsanalyse af spektrale Cole-Cole parametre, som er bestemt ud fra tidsdomæne jævnstrøms- (DC) og induceret polarisationsdata (IP). En nyudviklet algoritme indsamler modeller fra en sandsynlighedsfordeling baseret på en realisering af den estimerede kovariansmatrix, som lader algoritmen variere skridtlængden i henhold til modelparametrenes usikkerheder. Den nye algoritme når en ligevægt over hundrede gange hurtigere end en standard Metropolis-Hastings algoritme.

Syntetisk data er blevet inverteret med algoritmen. Resultaterne viser, at Cole-Cole paramenterne kan opløses fra tidsdomænedata, samt at deres betingede sandsynlighedsfordelinger er unimodale og tilnærmelsesvis klokkeformede i det logaritmiske rum. Opløseligheden af parametrene viser sig at være begrænset af, hvor længe IP signalet er blevet målt og hvor meget af signalet, der anvendes i inversionen samt værdierne af ladningsevnen, m_0 , og frekvenseksponenten, C , som har en direkte indflydelse på signalstøj-forholdet. I de undersøgte modeller kunne Cole-Cole paramenterne ikke opløses for m_0 under 10 mV/V. For at opnå brugbare resultater skal anvendelsestiden af IP signal, som minimum svare til den standard, der anvendes i HydroGeofysikgruppen ved Aarhus Universitet, som er 2.59-4000 ms.

Cole-Cole paramenterne har vist sig at være korreleret, og en tydeligt m_0 - C antikorrelation er blevet observeret i de fleste modeller. For opløste modeller er korrelationerne lineære i det logaritmiske rum, men når opløseligheden falder, begynder korrelationerne at blive mere ikke-lineære. En sammenligning af MCMC inversionsresultater og resultater fra en lineariseret inversionsmetode viser, at de to metoder finder den samme løsning, og at den lineariserede estimerede usikkerhedsanalyse er en god tilnærmelse af den faktiske usikkerhed for opløste modeller, mens der for uopløste parametre er en tendens til, at den lineariserede metode undervurderer usikkerhederne.

Contents

Preface	i
Acknowledgements	ii
Abstract.....	iii
Resume	iv
Contents	v

1 INTRODUCTION..... 1

2 THEORY 4

2.1 Basic principles of DCIP.....	4
2.1.1 Apparent resistivity.....	4
2.1.2 Chargeability	5
2.1.3 The DCIP signal.....	5
2.1.4 Gating, waveform, and stacking	7
2.1.5 Data quality	8
2.2 Induced polarization.....	9
2.2.1 Membrane polarization	9
2.2.1 Grain polarization	10
2.3 The Cole-Cole model	11
2.3.1 Time-domain.....	11
2.3.2 Application of Cole-Cole parameters	13
2.4 Basic inversion theory	13
2.4.1 Inversion of DCIP data	13
2.4.2 Linear problems	14
2.4.3 Nonlinear problems	15
2.5 Linearized inversion in AarhusInv	15
2.5.1 Forward mapping.....	15
2.5.2 Inversion.....	16
2.5.3 Limits of the linearized approach.....	17
2.6 Introduction to Monte Carlo methods	17
2.6.1 Probabilistic formulation.....	18
2.6.2 Markov chain Monte Carlo	18
2.6.3 Metropolis-Hastings	18

3 METHOD - MCMC ALGORITHM..... 20

3.1 MCMC algorithm.....	20
3.1.1 Parameterization in AarhusInv	20
3.1.2 MCMC inversion algorithm	20
3.1.3 Initialization	21
3.1.4 Proposer algorithm	23
3.1.5 Acceptance criterion	23
3.2 Synthetic data	24
3.2.1 Electrode configuration	24
3.2.2 Gating.....	25
3.2.3 Noise model	25

4	METHOD - DCIP STUDIES	27
4.1	Study of proposer algorithm	27
4.1.1	Gaussian model proposer	27
4.1.2	Comparative analysis	27
4.2	Study of a homogenous half-space	28
4.2.1	Convergence study for a homogenous half-space	28
4.2.2	Sensitivity analysis of a homogenous half-space	28
4.3	Study of Ghorbani <i>et al.</i> (2007).....	29
4.4	Study of acquisition ranges	30
4.5	Study of layered models	31
4.5.1	Parameter correlation	32
4.6	Study of resistivity equivalence.....	33
4.7	Study of IP.....	34
4.8	Field example.....	35
5	RESULTS.....	37
5.1	Proposer algorithms	37
5.2	Homogenous half-space.....	38
5.2.1	Convergence of a homogenous half-spaces	38
5.2.2	Sensitivity analysis of a homogenous half-space	40
5.3	Models from Ghorbani <i>et al.</i> (2007).....	44
5.4	Acquisition range	46
5.5	Layered models.....	50
5.5.1	Three-layer model.....	50
5.5.2	Five-layer model.....	53
5.6	Resistivity equivalence.....	56
5.6.1	High resistivity equivalence.....	56
5.6.2	Low resistivity equivalence.....	60
5.7	Information from IP	63
5.7.1	Chargeability	64
5.7.2	Time constant.....	66
5.7.3	Frequency exponent.....	67
5.8	Field example.....	69
6	DISCUSSION.....	73
6.1	The MCMC algorithm	73
6.1.1	General implementation issues.....	73
6.1.2	Scaling of model perturbation.....	73
6.1.3	High dimensions	74
6.2	Resolution of Cole-Cole parameters.....	75
6.2.1	Uncertainty analyses.....	75
6.2.2	Model from Ghorbani <i>et al.</i> (2007).....	79
6.2.3	Acquisition range	80
6.2.4	Parameter correlation	81
6.2.5	Field data	82
6.3	Linearity of the DCIP problem	83
6.3.1	Posterior probability distributions.....	83
6.3.2	Linearized inversion results	84
6.4	Information from IP	85
6.4.1	Resistivity equivalences	85
6.4.2	Resolution of layer boundaries.....	86
6.5	Prospects and further work	86
7	CONCLUSION.....	88

8 REFERENCES	90
---------------------------	-----------

APPENDIXES.....	1
A.1 Proposer algorithms	2
A.2 MATLAB scripts	3
A.3 Comparison of proposer algorithms	5
A.4 Ghorbani <i>et al.</i> (2007).....	8
A.5 Acquisition range	13
A.6 Three-layer model.....	14
A.7 Correlation matrixes.....	20
A.8 Field data	23
Conference abstract	26

1 Introduction

In 2010, the United Nations declared clean drinking water a human right¹. Even though 70% of the planet is covered by water, only 2% of it is fresh and most of this is locked in icecaps and glaciers (Marshak, 2007). It is therefore essential that we protect the fresh water resources we have, so we also in the future can accommodate the human right to drinking water.

In Denmark, most drinking water comes from groundwater aquifers. The water has a good quality and only little treatment is required. In the future, however, this will change if the aquifers become polluted. The Geological Survey of Denmark and Greenland (GEUS) has found traces of pesticides or high levels of nitrate in over 25% of the production wells in Denmark (Thorling *et al.*, 2015). Furthermore, contaminated plumes related to old landfills have been detected several places in Denmark, e.g. Gazoty *et al.* (2012). To protect the groundwater, it is important that contaminations like these can be mapped in the subsurface, so the migration of the contamination can be predicted. These predictions are important when planning the protection of the fresh water resources in the future.

A way of mapping the subsurface is by applying the geoelectric methods referred to as direct current (DC) and induced polarization (IP), or in combination DCIP. The methods involve measurements of the resistivity and the chargeability of the near subsurface and are increasingly applied in environmental investigations. Typical applications include lithological discrimination, e.g. Slater and Lesmes (2002) and Kemna *et al.* (2004), and landfill characterization, e.g. Gazoty *et al.* (2012).

A DCIP signal contains spectral information about the subsurface, which can be parametrized using the Cole-Cole model (Pelton *et al.*, 1978b). The Cole-Cole model includes the DC resistivity and three IP parameters describing the polarization effects of the ground. Studies have shown that the IP parameters can be linked to well-known physical properties such as grain size and grain size distributions (Pelton *et al.*, 1978a).

The resistivity of the subsurface is often used to discriminate geological lithologies. However, different lithologies does not have a unique resistivity, e.g. a heavy clay formation may have the same resistivity as a salt water saturated sand formation (Dinesen, 1962). By applying the IP parameters, it is possible to discriminate between formations with different capacitive properties. Clay with a high chargeability may thus be discriminated from salt water saturated sands. The presences of contaminants is also known to enhance the chargeability of the subsurface, why the IP method is increasingly applied for detection of contaminated plumes in environmental investigations.

The IP phenomenon has in the last decade been investigated in both frequency-domain and time-domain by different research groups (Fiandaca *et al.*, 2013). This thesis applies the time-domain DCIP method, which is the standard approach used at the HydroGeophysics Group at Aarhus University. Here, the high dimensional nonlinear

¹ Resolution 64/292: Resolution adopted by the UN General Assembly on 28 July 2010. www.un.org/es/comnu/docs/?symbol=A/RES/64/292&lang=E

problem of DCIP is normally inverted with a linearized approach using the inversion software, AarhusInv, developed at the university (Auken *et al.*, 2014).

Even though the combined DCIP methods is gaining a foothold among methods for environmental investigations, the information from the IP signal is still questioned. Studies, comparing frequency-domain and time-domain data, also question the ability of time-domain measurement to resolve the spectral Cole-Cole parameters (e.g. Ghorbani *et al.* (2007)). It is also argued that the problem of inverting time-domain IP is too nonlinear to justify a linearization and the use of least-squares methods.

In this thesis, I will study Cole-Cole parameters obtained from inversion of time-domain DCIP signal. The objectives are to understand how well spectral Cole-Cole parameters can be resolved from time-domain data, to understand the contribution from the IP signal, and to understand the limits of the DCIP methods in general.

The analyses are primarily based on inversion results of synthetic time-domain DCIP data. The inversion is carried out using a novel Markov chain Monte Carlo (MCMC) algorithm. The MCMC approach allows for studies of nonlinear parameter correlations, model equivalences and uncertainties, which cannot be obtained with a linearized approach. MCMC is a well-known method for inversion of nonlinear problems, however, to me and my academic advisors's knowledge, this is the first time that time-domain DCIP data and models have been analyzed using MCMC.

To start with, a stability study of the novel MCMC algorithm is carried out. This is done to ensure convergence and consistency of the inversion results.

Hereafter, a full uncertainty analysis of the Cole-Cole parameters is carried out. This includes a study of probability distributions for the individual Cole-Cole parameters. The study will show how well the spectral Cole-Cole parameters can be retrieved from time-domain data.

The acquisition range used for recording the IP signal varies in the scientific community. Here, it is investigated what influence the acquisition range have on the resolution of the Cole-Cole parameters. This is done by testing five different acquisition ranges on synthetic data.

To explore more complex Cole-Cole models, synthetic three and five-layer models are analyzed. Here, the parameter correlations are studied together with parameter uncertainty. Resistivity equivalences are tested by inverting DCIP and DC data generated on models with high- and low resistivity equivalences. In this way, it can be studied whether the IP part of the signal adds any information to the DC data.

Throughout the thesis, the studies of parameter correlation, parameter uncertainty and parameter distributions are used to investigate the degree of linearity of the time-domain DCIP method. MCMC inversion results and uncertainty analysis are also compared to the linearized inversion approach normally used in AarhusInv. This, combined, will indicate if a linearization of the DCIP inversion problem is justified. This is of large significance for the confidence in the results and uncertainty analyses produced by AarhusInv.

In the following, I will give an introduction to the time-domain DCIP method including a descriptions of the IP phenomenon and the Cole-Cole model. I will describe the forward modelling and inversion of DCIP data. The focus here is on the MCMC approach in general. The specific MCMC algorithm used in this thesis is described in the first part of the method section. The second part describes how the studies introduced above are carried out. The results of the studies are presented in the same order as the methods are describes. The results and the discussion of these are presented in individual chapters following the research questions.

2 Theory

Direct current (DC) and induced polarization (IP) are geoelectric methods used to describe the electrical properties of the subsurface. The methods are often applied as a combination referred to as the DCIP method. Resistivity and chargeability data are gathered in the field and the data are processed and inverted to retrieve the Cole-Cole parameters, which describe a geoelectric model of the subsurface.

In the following section (Section 2.1), the general terms used in the DCIP method and the DCIP signal are introduced. Section 2.2 introduces the Cole-Cole model and Section 2.3 presents the principles of inversion.

2.1 Basic principles of DCIP

The electrical properties of the subsurface can be studied by injecting a current into the ground and measuring the resulting potential. A four-electrode approach, also called a quadrupole, is used to carry out the measurements (Figure 2.1). Two of the electrodes, A and B , function as source and sink for a current, I , to create an electric circuit in the ground. Between the remaining two electrodes, M and N , the potential difference, ΔV , is measured. The data parameters, apparent resistivity and chargeability, are then computed from the measured potential.

2.1.1 Apparent resistivity

Electrical conductivity, σ , is a measure of a material's ability to conduct an electric current. The corresponding unit is Siemens per meter [S/m]. The inverse of conductivity is electrical resistivity, ρ , which is a measure of how strongly a material opposes a flow of an electric current. The unit of resistivity is Ohm meter [Ωm].

If a current is sent through a electrode into a homogenous and isotropic half-space and a second electrode is infinitely far away, then the current will flow radially into the ground. In this case the resulting potential in the ground can be expressed as

$$V(r) = \frac{\rho I}{2\pi r}, \quad (2.1)$$

where I is the current, ρ is the resistivity of the ground, and r is the distance from the source electrode to the observation point (Christensen 2012). For a setup like the one in Figure 2.1, the potential difference between the two electrodes is given as

$$\Delta V = V_M - V_N = \rho \frac{I}{K}, \quad (2.2)$$

where K is a geometric factor depending on the spacing between the electrodes:

$$K = 2\pi \left[\frac{1}{|AM|} - \frac{1}{|BM|} - \frac{1}{|AN|} + \frac{1}{|BN|} \right]^{-1}. \quad (2.3)$$

For any four-electrode configuration, Eq. (2.2) is used to determine the apparent resistivity,

$$\rho_a = \frac{\Delta V}{I} K . \quad (2.4)$$

The apparent resistivity reflects the average resistivity of the subsurface volume where the current flows. In other words, the apparent resistivity is the resistivity a homogenous half-space should have to give the same response as the actual subsurface.

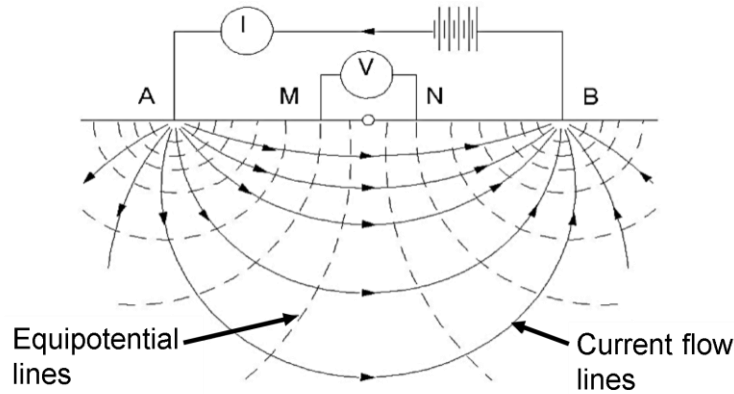


Figure 2.1: Sketch of current injection into a homogenous isotropic half-space. An electric circuit is created between electrode *A* and *B*. The resulting potential difference is measured between electrode *M* and *N*. The figure is modified from Christensen (2012).

2.1.2 Chargeability

The chargeability, M , quantifies a material's ability to remain charged after a forcing current is removed. The signal of the chargeability is analyzed in either time-domain or frequency-domain. In frequency-domain, the signal is characterized by a phase shift between the injected current and the measured potential (Ghorbani *et al.*, 2007). In time-domain, the signal is the decay curve of the transient potential (Figure 2.2). The chargeability is computed from the potential decay in the DCIP signal as described in the following section.

2.1.3 The DCIP signal

Figure 2.2a shows the signal of the injected current together with the measured potential. As the current is injected into the ground, the potential, $V(t)$, starts to rise across the potential electrodes (Gazoty *et al.*, 2012). The rise of the potential is delayed compared to the signal of the injected current. This is the charge-up effect. The effect is caused by the capacitive properties of the subsurface, which are related to induced polarization effects. The origin of the IP effect is described in Section 2.2.

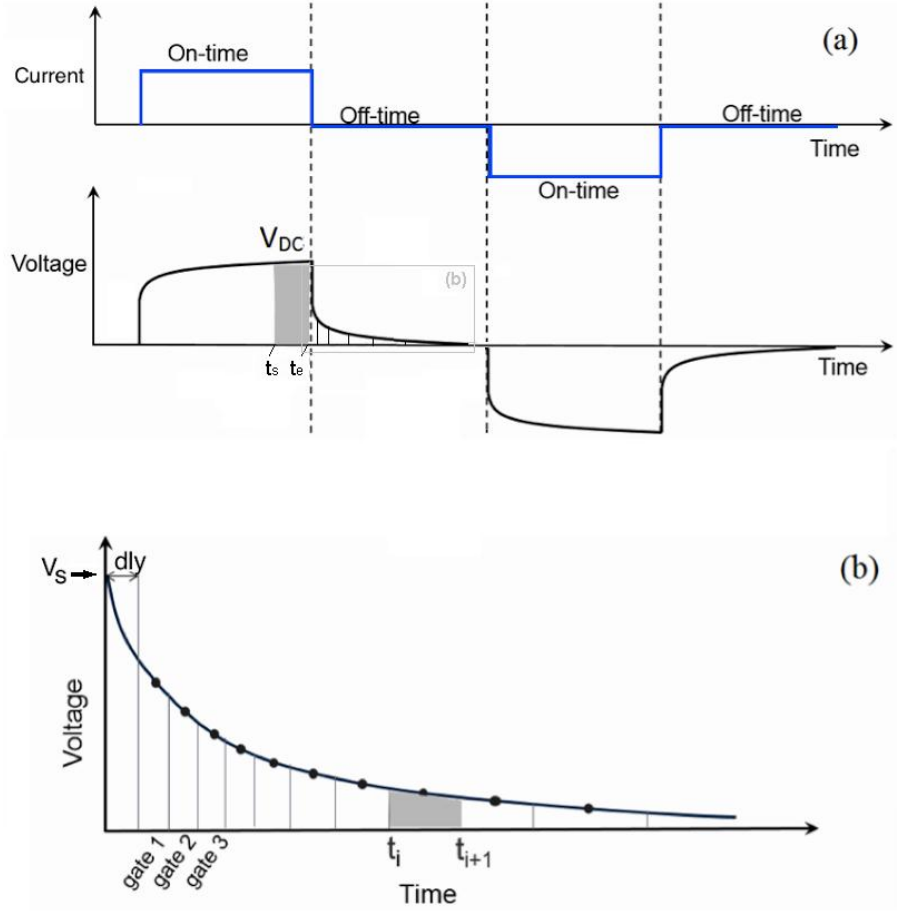


Figure 2.2: Sketch of the time-domain DCIP signal. Figure (a) shows an injected current (blue line) and the resulting potential, $V(t')$, in the plot below. V_{DC} indicates where the resistivity is computed, by averaging the integrated potential between t_s and t_e . Figure (b) is an enlargement of the IP decay, where the chargeability is computed. V_s is the level of the secondary potential and dly is the acquisition delay before the first measurement. The decay is divided into gates, where the i 'th gate goes from t_i to t_{i+1} . The figure is modified from Gazoty et al. (2012).

The DC potential, V_{DC} , which is used to compute the apparent resistivity, is measured just before the current is turned off. Here, the potential signal, $V(t')$, is close to being stationary and the ratio between the potential and the current is almost constant. V_{DC} is computed as

$$V_{DC} = \frac{\int_{t_s}^{t_e} V(t') dt'}{(t_e - t_s)}, \quad (2.5)$$

where $V(t')$ is the measured potential and t_s and t_e are the start and end time of the averaging interval on the potential curve (Fiandaca *et al.*, 2012).

When the current is turned off, the potential drops to a secondary level V_s . The IP effect now causes $V(t')$ to decay with time. Previously, only the integrated IP decay was used to compute the chargeability. This corresponds to only analyzing one frequency in the frequency-domain and the spectral content of the signal is therefore disregarded. Today, the entire decay is used. The decay is divided into time gates as seen in Figure 2.2b and

the chargeability is computed by integrating $V(t')$ in each gate. The IP potential, V_{IP} , of the i 'th gate is

$$V_{IP,i} = \frac{\int_{t_i}^{t_{i+1}} V(t') dt'}{(t_{i+1} - t_i)}, \quad (2.6)$$

where t_i and t_{i+1} are the start and end time of the i 'th gate.. The chargeability, M_i [mV/V], of the i 'th gate is now given as the IP potential normalized by the DC potential (Slater & Lesmes, 2002),

$$M_i = \frac{V_{IP,i}}{V_{DC}} \cdot 1000. \quad (2.7)$$

The normalization makes the chargeability independent of the DC resistivity.

2.1.4 Gating, waveform, and stacking

There are different ways of dividing the potential decay into gates. If linearly distributed gates are used, the decay of the potential will cause the signal-to-noise ratio to decrease with time, because the magnitude of the signal approaches the magnitude of the noise (Fiandaca *et al.*, 2012). Instead, the gates may be distributed so the width of the gates increases logarithmically with time. In this way, a better signal-to-noise ratio is obtained at the late times, because the noise is averaged out. If the gates, however, become too long at the late times, there is a risk of losing information about the decay, because the signal is averaged out as well.

The signal presented in Figure 2.2 has a 50% duty cycle waveform. This means that the waveform of the injected current has a positive pulse, which is followed by a current off-time, which again is followed by a negative pulse. V_{bc} is then measured during the current on-time and the IP decay is measured during the current off-time. This approach is traditionally applied in DCIP, e.g. Dahlin *et al.* (2002), Gazoty *et al.* (2012) and Doetsch *et al.* (2015).

Dahlin & Leroux (2010) suggested the use of a 100% duty cycle. Here, a positive pulse is directly followed by a negative pulse without turning the current off (Figure 2.3). The IP decay is thus measured during the current on-time. Olsson *et al.* (2015) showed that the 100% duty cycle increases the signal-to-noise ratio, because the magnitude of the potential increases from the superposition of the potential decay and the ongoing current injection.

To increase the signal-to-noise ratio, the waveforms are stacked by subtracting the pulses with opposite signs (Fiandaca *et al.*, 2012). The 100% duty cycle makes twice as many stacks as a 50% duty cycle during the same acquisition time, because the duration of one waveform is shorter for the 100% (Figure 2.3). In this way, the application of the 100% duty cycle reduces the acquisition time to half.

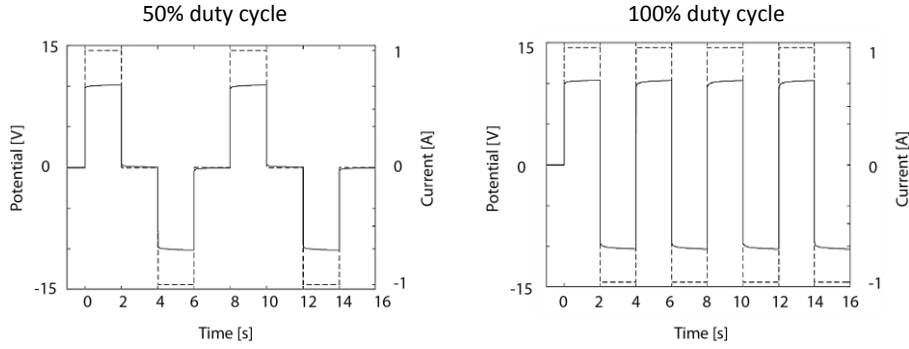


Figure 2.3: Modelled waveform for a 50% and a 100% duty cycle showing the injected current (dashed line) and measured potential (solid line). The signal from 0-16 s corresponds to four stacks for the 100% duty cycle; twice as many as achieved with a 50% duty cycle with the same acquisition time. The figure is modified from Olsson et al. (2015).

2.1.5 Data quality

The IP potential, V_{IP} , has a very low magnitude, which is often below one percent of the magnitude of the DC potential. It is therefore important to optimize the data quality in order to get an acceptable signal-to-noise ratio for the IP potential. It is well known for all geoelectric methods that the signal-to-noise ratio decreases with depth, thus the resolution will also decrease with depth (Christensen, 2012). From Eq. (2.7) the IP potential can be described as

$$V_{IP,i} = \frac{V_{DC} M_i}{1000}. \quad (2.8)$$

From Eq. (2.4) we have that the DC potential may be described by the apparent resistivity, ρ_a , the injected current, I , and the geometric factor, K , so

$$V_{DC} = \frac{\rho_a I}{K} \quad (2.9)$$

may be substituted into Eq. (2.8) to get

$$V_{IP,i} = \frac{\rho_a I}{K} \frac{M_i}{1000}. \quad (2.10)$$

Eq. 2.10 shows that the best signal-to-noise ratio of the IP potential is obtained by minimizing the geometric factor and by increasing the current.

Several other factors also influence the signal quality, where caution must be taken regarding self-potential (SP), electrochemical potentials, galvanic coupling, and capacitive coupling (Christensen, 2012). Capacitive coupling occurs between cables used for measurements and the ground, where galvanic coupling can arise from coupling between the wires inside the cables or from coupling with power lines or electric fences. SP in the ground is caused by the magnetic field of the Earth as well as power lines and electronic devices. SP can show up in the signal as a single offset or as a tendency. The harmonic noise from household supplies can, however, easily be removed during data processing, and is therefore of little influence to the final result. The same holds for removal of spikes in the signal due to coupling.

2.2 Induced polarization

The charge-up effect and the potential decay in the DCIP signal are caused by induced polarization in the subsurface. The exact origin of the IP effect is a complex matter, and is not fully understood yet (Kemna *et al.*, 2012). In general, induced polarization arises from transport and accumulation of charged ions and electrons in the pore space of a rock matrix. The origin of the IP effect is here explained by the main mechanisms: Membrane polarization and grain polarization.

2.2.1 Membrane polarization

Membrane polarization is caused by either constriction within a pore space or the presence of clay minerals (Reynolds, 1997). The net charges at the interface of rock minerals are negative, as shown in Figure 2.4. Therefore, positive charges in the pore fluid are attached to the wall of the pores creating a positively charged layer (i.e. an electrical double layer is created). If the diameter of the pore is smaller than the thickness of the positive layer, it will block the flow of ions when a current is applied. When the applied current is turned off again, the ions will diffuse back to an equilibrium position, and the potential difference across the pore blockage decays with time. This is seen as the potential decay in the DCIP signal.

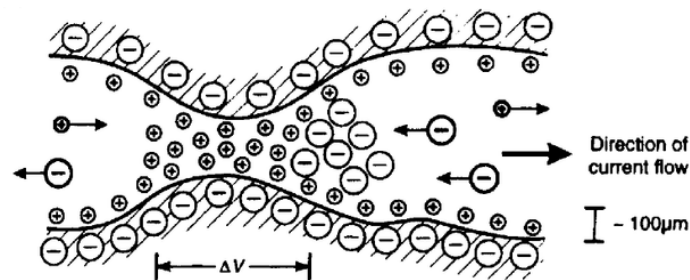


Figure 2.4: Development of membrane polarization. When a current is applied to a rock matrix in the subsurface, ions can create a barrier in a pore channel if the electrical double layer is wider than the channel. A potential gradient builds up and is released again when the current is turned off. This is one of the mechanisms causing the IP effect. Figure from Reynolds (1997).

Clay minerals can also cause membrane polarization (Marshall & Madden, 1959). Clays have a negative surface charge, which attracts positive ions from the pore fluid creating an electrical double layer (Figure 2.5). The cloud of ions acts as a membrane between adjacent grains of a rock matrix. The membrane enhances the transport of small positive ions relative to the larger negative ions when an electric current is applied (Figure 2.6). This produces a local difference in the ion concentration (Fraser *et al.*, 1964). When the current is turned off, the ions will redistribute themselves back to an equilibrium position and the local imbalance in the ion concentration will decay with time.

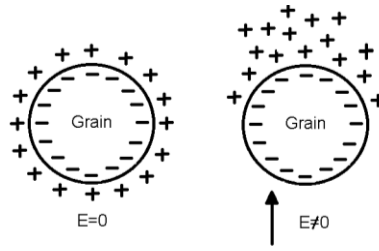


Figure 2.5: Sketch of polarization of an electrical double layer around a single mineral grain, e.g. clay. When an external current is applied, the positive ions around the grain will be displaced. When the current is turned off, the ions will diffuse back to their equilibrium position. The figure is modified from Christiansen (2012).

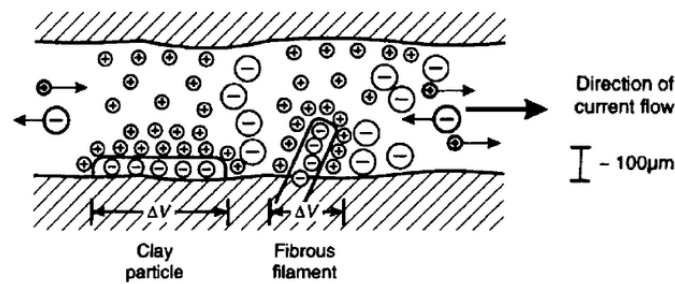


Figure 2.6: Development of membrane polarization in the pore space of a rock matrix due to negatively charged clay minerals. Figure from Reynolds (1997).

2.2.1 Grain polarization

If a conductive grain blocks the pore space, where the injected current is conducted, a charge will build up on the surface on both sides of the grain and the electrical double layer will become polarized as shown in Figure 2.7 (Reynolds, 1997). When the current is turned off, the ions diffuse back to an equilibrium stage and the potential difference across the grain decays with time.

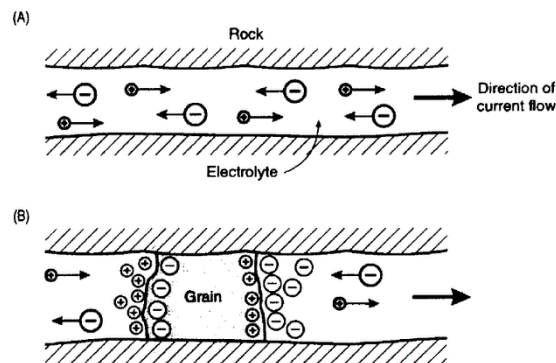


Figure 2.7: Grain polarization. (A) Electrolytic flow in an open pore space with no restrictions. The large arrow indicates the direction of the injected current. (B) Polarization of a conductive grain, blocking a channel in a pore or small fracture. Figure from Reynolds (1997).

2.3 The Cole-Cole model

The Cole-Cole model is an empirical extension of a Debye relaxation model (Cole & Cole, 1941). Pelton *et al.* (1978b) rewrote the model so it could be applied for DCIP, where the electrical complex resistivity (ζ_i) of a i 'th layer is given by:

$$\zeta_i(\omega) = \rho_i \left[1 - m_{0i} \left(1 - \frac{1}{1 + (i\omega\tau_i)^{c_i}} \right) \right]. \quad (2.11)$$

In frequency-domain, the chargeability, m_0 , describes the magnitude of the polarization as defined by Seigel (1959). The model parameter τ [s] is a time constant describing the physical relaxation time of the potential decay and C is the Cole-Cole exponent describing the frequency dependence. C typically varies between 0.1 and 0.6 (Pelton *et al.*, 1978a). The variable ω [s^{-1}] is the angular frequency.

The model parameters are visualized in Figure 2.8. The figures shows that C controls the spread of the phase response. Low values of C indicate a widely spread response. m_0 controls the height of the peak and τ the location. The frequency, where the phase response peaks, is referred to as the peak frequency, ω_{peak} . This frequency controls which part of the frequency spectrum that contains information about IP.

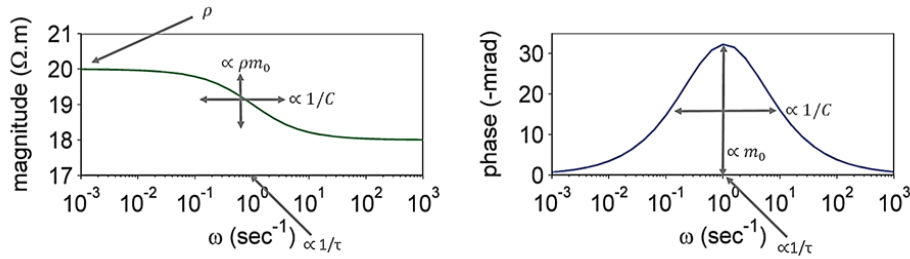


Figure 2.8: Frequency-domain: Visualization of the Cole-Cole parameters (ρ , m_0 , τ and C) for a frequency-domain response. Left: The magnitude of the IP effect as function of the angular frequency. This is the real part of the complex resistivity. Right: The phase shift as function of the angular frequency, which is the imaginary part of the complex resistivity. The peak frequency, ω_{peak} , is $1 s^{-1}$. The figure is modified from Christiansen (2012).

2.3.1 Time-domain

In time-domain, the chargeability takes the following form (Pelton *et al.*, 1978b),

$$M_i(t) = m_{0i} \sum_{n=0}^{\infty} \frac{(-1)^n \left(\frac{t}{\tau_i}\right)^{nc_i}}{\Gamma(1 + nc_i)}, \quad (2.12)$$

where $\Gamma(x)$ is the gamma function and the remaining variables are defined as for Eq. (2.11). The spectral Cole-Cole parameters are more difficult to visualize in time-domain compared to frequency-domain. The chargeability, m_0 , is the magnitude of M taken at $t = t_0$, i.e. the first time point on the IP decay after the acquisition delay, dly (see Figure 2.2). The time constant, τ , controls the length of the IP decay and C controls the shape as well as the length of the decay.

Figure 2.9 to Figure 2.11 show IP decays simulated on a homogenous half-space with the geophysical properties $\rho = 100 \Omega\text{m}$, $m_0 = 50 \text{ mV/V}$, $\tau = 0.1 \text{ s}$ and $C = 0.4$. In Figure 2.9, the value of m_0 is varied from 5 mV/V to 500 mV/V. As m_0 increases the magnitude of the signal increases. In Figure 2.10, τ is varied from 0.001 s to 10 s. For a small τ , the decay of the IP signal happens at early times and for a large τ the decay happens at late times. Figure 2.11 shows that an increasing value of C increases the magnitude of the IP signal. A change in the DC resistivity, ρ , does not have an influence on the IP decays because of the normalization in Eq. (2.7)

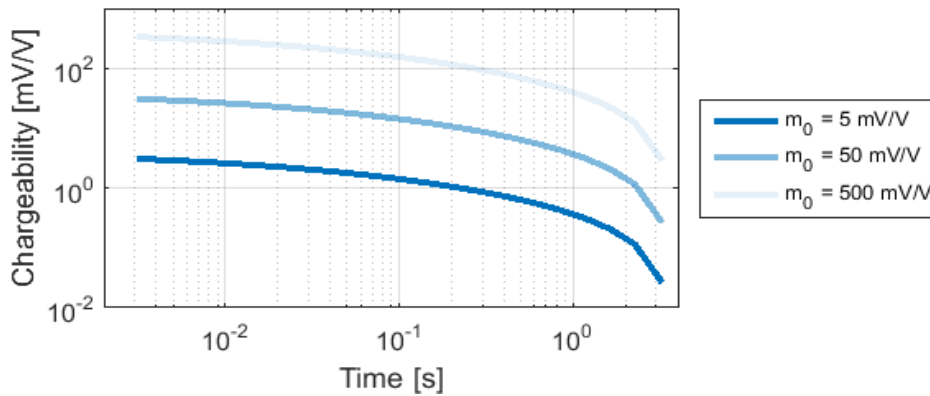


Figure 2.9: Time-domain: The influence of chargeability, m_0 , on the IP decay. The decays are modelled on a homogenous half-space with the model parameters: $\rho = 100 \Omega\text{m}$, $\tau = 0.1 \text{ s}$, and $C = 0.4$.

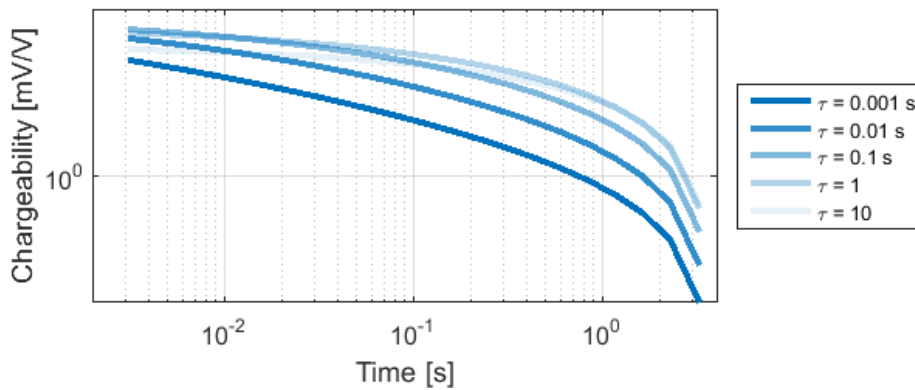


Figure 2.10: Time-domain: The influence of time constant, τ , on the IP decay. The decays are modelled on a homogenous half-space with the model parameters: $\rho = 100 \Omega\text{m}$, $m_0 = 50 \text{ mV/V}$, and $C = 0.4$.

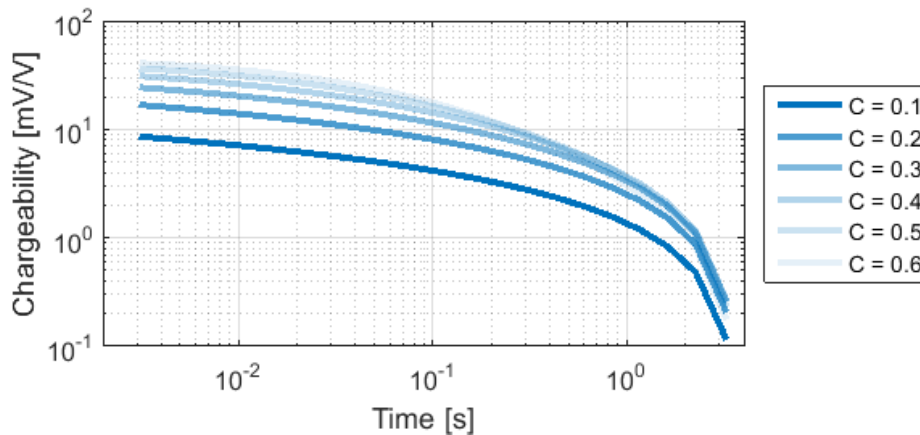


Figure 2.11: Time-domain: The influence of the frequency exponent, C , on the IP decay. The decays are modelled on a homogenous half-space with the model parameters: $\rho = 100 \Omega\text{m}$, $m_0 = 50 \text{ mV/V}$, and $\tau = 0.1$.

2.3.2 Application of Cole-Cole parameters

The spectral Cole-Cole parameters are related to well-known physical properties of the subsurface (Christiansen, 2012). The magnitude of the IP effect depends on the quantity of polarizable element in the ground. If organic material or hydrocarbons are present in the formation, coating of the rock matrix surface and general increase in ion density will in some cases enhance the chargeability.

The time constant, τ , is directly related to the size of the conductive grains in the mineralized rock (Pelton *et al.*, 1978a) as well as the volume of the pore space (e.g. Titov *et al.* (2002) and Slater (2007)). The frequency exponent, C , depends on the size distribution of the polarizable elements (Vanhala, 1997).

2.4 Basic inversion theory

When the data parameters, apparent resistivity and chargeabilities, have been computed from field measurements, the next step of the DCIP method is to invert the data to obtain the spectral information of the subsurface parameterized by the Cole-Cole model.

The fundamentals of inversion theory will be presented in this section. In the Section 2.5, the linearized inversion method in AarhusInv will be introduced.

2.4.1 Inversion of DCIP data

Inverse problem theory describes how information of a parameterized physical system can be derived from observational data. This is the opposite of a forward (or direct) problem, where data are computed on a physical model. Inversion theory is often applied in geophysics, where the aim is to obtain information about the subsurface from surface measurements.

For the time-domain DCIP method, the apparent resistivity and the chargeabilities represent the observational data. For one DCIP measurement, the data vector \mathbf{d}_{obs} is

$$\begin{aligned} \mathbf{d}_{obs} &= [\rho_a, M_i]; \\ i &= 1 \dots N_{gates}. \end{aligned} \quad (2.13)$$

The Cole-Cole parameters describe the model we want to find from the inversion. For a 1D model with one layer, the true model vector, \mathbf{m}_{true} , is given as

$$\mathbf{m}_{true} = [\rho_{true}, m_{0,true}, \tau_{true}, C_{true}]. \quad (2.14)$$

The computation of \mathbf{d}_{obs} from the Cole-Cole parameters is a forward problem. Going the opposite way, i.e. computing the Cole-Cole parameters from apparent resistivity and chargeability, is the inverse problem.

2.4.2 Linear problems

The introduction to linear and nonlinear problems follows the terminology of Jacobsen (2010). The linear forward problem can be expressed as

$$\mathbf{d}_{obs} = \mathbf{G} \cdot \mathbf{m}_{true} + \mathbf{e}_{obs}, \quad (2.15)$$

where the observational error, \mathbf{e}_{obs} , is assumed to be a stochastic vector with the covariance matrix:

$$\mathbf{C}_{obs} = cov(\mathbf{e}_{obs}). \quad (2.16)$$

If $\mathbf{m} \in \mathbb{R}^N$ and $\mathbf{d} \in \mathbb{R}^M$, then \mathbf{G} is a N by M matrix representing a linear transformation from model space to data space:

$$\mathbf{G}: \mathbf{m} \in \mathbb{R}^N \mapsto \mathbf{d} \in \mathbb{R}^M. \quad (2.17)$$

So, since the forward computation of \mathbf{m}_{true} leads to the true data without noise, \mathbf{d}_{true} , Eq. (2.15) can be rewritten as

$$\mathbf{d}_{obs} = \mathbf{d}_{true} + \mathbf{e}_{obs}. \quad (2.18)$$

An estimate of the true model, \mathbf{m}_{est} , can be found by inversion. If \mathbf{G} is squared (i.e. $M = N$) and invertible, then the estimate of \mathbf{m}_{true} is given as

$$\mathbf{m}_{est} = \mathbf{G}^{-1} \mathbf{d}_{obs}. \quad (2.19)$$

If \mathbf{G} is not square, Eq. (2.19) does not hold. In that case, the best model estimate is defined as the model that minimizes a specified misfit criterion, Q . A well-known misfit criterion is the sum of squared residuals between the observed data and the model response, \mathbf{Gm} , expressed as

$$Q_{lsq} = \|\mathbf{d}_{obs} - \mathbf{Gm}\|^2. \quad (2.20)$$

Closely related is the maximum likelihood estimation, where the least squares criterion is weighted by the observational errors in the form of the covariance matrix. In this case, the misfit criterion is given by

$$Q_{mle} = \|\mathbf{d}_{obs} - \mathbf{Gm}\|_{\mathbf{C}_{obs}^{-1}}^2. \quad (2.21)$$

The maximum likelihood solution is the model that minimized the misfit function. The solution is given as

$$\mathbf{m}_{mle} = (\mathbf{G}^T \mathbf{C}_{obs}^{-1} \mathbf{G})^{-1} \mathbf{G}^T \mathbf{C}_{obs}^{-1} \mathbf{d}_{obs}. \quad (2.22)$$

2.4.3 Nonlinear problems

The general expression of Eq. (2.15) is given by

$$\mathbf{d}_{obs} = \mathbf{g}(\mathbf{m}) + \mathbf{e}_{obs}. \quad (2.23)$$

When $\mathbf{g}(\mathbf{m})$ is not a linear mapping, the problem is referred to as a nonlinear problem. In this case, $\mathbf{g}(\mathbf{m})$ is a vector of nonlinear functions, which may include non-differentiable features (e.g. jumps or kinks). In the nonlinear case, the linear transformation matrix, \mathbf{G} , does not exist. If, however, the functions are differentiable with slowly varying partial derivatives, they are referred to as mildly nonlinear. A mildly nonlinear problem can be linearized to approximate the linear problem where the maximum likelihood estimate can be determined.

The forward response of the time-domain DCIP method is nonlinear but differentiable, why it may be referred to as a mildly nonlinear problem.

2.5 Linearized inversion in AarhusInv

In this section, the inversion scheme and the forward code used in AarhusInv (Auken *et al.*, 2014) will be presented.

2.5.1 Forward mapping

AarhusInv applies the forward code described by Fiandaca *et al.* (2012). Given the spectral Cole-Cole parameters of a layered model, the code uses the Cole-Cole model to compute the corresponding IP decay (forward response). The code applies the full waveform of the signal to assess the spectral content of the IP decay. It takes the transmitter waveform into account including the number of stacks used during the measurement and the pulse duration for the charge-up effect.

The nonlinear forward problem is linearized to approximate a linear problem, where the methods described in Section 2.4.2 can be used to minimize the misfit function and find the best model estimate. More accurately, a linearization is carried out to approximate the Jacobian matrix, \mathbf{G} , holding the partial derivatives used for mapping between the model space and the data space. For the s 'th parameter in the data vector and the t 'th parameter in the model vector, the Jacobian is defined as

$$\mathbf{G}(\mathbf{m})_{st} = \frac{\partial \mathbf{g}(\mathbf{m})_s}{\partial \mathbf{m}_t} = \frac{\partial \mathbf{d}_s}{\partial \mathbf{m}_t}. \quad (2.24)$$

A Taylor expansion of the model response linearizes the problem. AarhusInv applies a first order Taylor without the truncation error, so a linearized expansion in the point \mathbf{m}_i is given as (Egholm, 2014),

$$\mathbf{g}(\mathbf{m}_i + \delta \mathbf{m}) \cong \mathbf{g}(\mathbf{m}_i) + \mathbf{G} \delta \mathbf{m}, \quad (2.25)$$

which can be rearranged to

$$\mathbf{G} \cong \frac{\mathbf{g}(\mathbf{m}_i + \delta\mathbf{m}) - \mathbf{g}(\mathbf{m}_i)}{\delta\mathbf{m}}, \quad (2.26)$$

where $\delta\mathbf{m}$ is the vector of a model perturbation from the point of expansion \mathbf{m}_i and $\mathbf{g}(\mathbf{m}_i)$ is the forward response of \mathbf{m}_i . The change in the data space can be expressed as

$$\delta\mathbf{d}(\mathbf{m}_i) = \mathbf{d}_{\text{obs}} - \mathbf{g}(\mathbf{m}_i) \cong \mathbf{G} \delta\mathbf{m} + \mathbf{e}_{\text{obs}}. \quad (2.27)$$

2.5.2 Inversion

The inversion of DCIP data is an iterative procedure (Auken & Christiansen, 2004). A start model, \mathbf{m}_i is defined. The goal is now to determine a new model \mathbf{m}_{i+1} ,

$$\mathbf{m}_{i+1} = \mathbf{m}_i + \delta\mathbf{m}_{\text{est}} \quad (2.28)$$

which minimized the misfit criterion given as (Fiandaca *et al.*, 2012),

$$Q = \left(\frac{\delta\mathbf{d}^T \mathbf{C}_{\text{obs}}^{-1} \delta\mathbf{d}}{N + M} \right)^{1/2}, \quad (2.29)$$

where $\delta\mathbf{d}$ is given in Eq. (2.27) and N and M are the number of data and model parameters respectively. To find \mathbf{m}_{i+1} , the perturbation, $\delta\mathbf{m}_{\text{est}}$, must be computed. The misfit function is minimized in a maximum likelihood approach, where the solution to the inverse problem is given as

$$\delta\mathbf{m}_{\text{est}} = [\mathbf{G}(\mathbf{m}_i)^T \mathbf{C}_{\text{obs}}^{-1} \mathbf{G}(\mathbf{m}_i)]^{-1} \mathbf{G}(\mathbf{m}_i)^T \mathbf{C}_{\text{obs}}^{-1} \delta\mathbf{d}(\mathbf{m}_i). \quad (2.30)$$

The resulting estimate for the next model in the iteration therefore becomes

$$\mathbf{m}_{i+1} = \mathbf{m}_i + [\mathbf{G}(\mathbf{m}_i)^T \mathbf{C}_{\text{obs}}^{-1} \mathbf{G}(\mathbf{m}_i)]^{-1} \mathbf{G}(\mathbf{m}_i)^T \mathbf{C}_{\text{obs}}^{-1} \delta\mathbf{d}(\mathbf{m}_i). \quad (2.31)$$

When \mathbf{m}_{i+1} is computed the first iteration is complete. The iterations are then continued until a certain stopping criteria is reached. In AarhusInv the iteration stops when the change of the data residual gets below a certain value (Auken & Christiansen, 2004).

It is common to work with prior information and constrains of variables when inverting geoelectric data. This information is simply added as an extension to the already existing vectors. However, in this thesis, constrains have not been applied.

Analysis of model estimated uncertainties

The parameter sensitivity analysis of the final model in the inversion is the linearized approximated covariance of the estimation error (Auken & Christiansen, 2004):

$$\mathbf{C}_{\text{est}} = (\mathbf{G}^T \mathbf{C}_{\text{obs}}^{-1} \mathbf{G})^{-1}. \quad (2.32)$$

Because the model parameters in AarhusInv are represented as logarithms, the uncertainties are given as standard deviation factors (STDF). So, the STDF of the parameters m_i is defined by:

$$\text{STDF}(m_i) = \exp\left(\sqrt{\mathbf{C}_{\text{est}(i,i)}}\right). \quad (2.33)$$

In this case, it is 68% likely that the model parameter, m_i , falls in the interval:

$$\frac{m_i}{STDF(m_i)} < m_i < m_i \cdot STDF(m_i). \quad (2.34)$$

A perfect resolution will give a $STDF = 1$. Using the terminology from Auken *et al.* (2005), $STDF < 1.2$ is a well-resolved parameter, $1.2 < STDF < 1.5$ is a moderately resolved parameter, $1.5 < STDF < 2$ is a poorly resolved parameter and $STDF > 2$ is an unresolved parameter.

2.5.3 Limits of the linearized approach

A Taylor expansion used for linearization is only valid in the neighborhood of the point of expansion, \mathbf{m}_i , and for small changes in the model space. As a consequence, the region where the approximation is valid depends on the smoothness of the differential functions of the forward problem. When the partial derivatives of the forward mapping are almost constant in the model space, then the Taylor approximation is very good. But as nonlinearity increases, the approximation deteriorates in several ways.

In the nonlinear case, the estimation error does not necessarily obey a Gaussian distribution, not even if the observational errors are Gaussian (Jacobsen, 2010). The estimation errors may have infinite variances and even if the covariance matrix is finite it is still different from the covariance matrix found from the linearized approach, so

$$\mathbf{C}_{est} \neq (\mathbf{G}^T \mathbf{C}_{obs}^{-1} \mathbf{G})^{-1}. \quad (3.35)$$

In general, linearized techniques are likely to underestimate the uncertainties when nonlinearity is severe (Sambridge & Mosegaard, 2002). Furthermore, the result of an iterative solution to a nonlinear problem is not guaranteed to converge to the global minimum of the misfit function, because the problem may have more than one solution, meaning that the misfit function may have more than one minimum.

It is not possible to know if a linearized estimate of the covariance matrix is accurate unless a fully nonlinear calculation has been performed. The same holds for the iterative minimization process. A way to perform a full analysis of a nonlinear problem is by applying Monte Carlo methods.

2.6 Introduction to Monte Carlo methods

As mentioned, a misfit function of a nonlinear problem may have more than one minimum. This means that minimization methods have a risk of getting trapped in a local minimum and thereby not solving the inverse problem entirely. This is one of the risks associated with using a linearized inversion for solving the DCIP problem.

A simple method to avoid this, is to do an exhaustive search of the model space. In practice, all models within a chosen subspace are analyzed, and for every model a data misfit is computed. The model with the smallest misfit is chosen as the best estimate.

An exhaustive search for the five Cole-Cole parameters will demand great computational power because the dimensionality of the problem increases a lot when more layers are added to the model. Instead, a Monte Carlo search can be used to bring down the number of forward calculations. The Monte Carlo (MC) methods sample the model space randomly with the use of a random-walk, and do not have to analyze every model in the model space.

Monte Carlo methods are, compared to linearized inversion approaches, more numerically stable in the minimizing (parameter search) stage, because they do not rely on a convergence of a sequence of model perturbations like the linearized approach and at the same time avoid the need for matrix inversion. They are also more reliable in estimating the uncertainties by means of the covariance matrix because they avoid derivatives and thereby the numerical approximations on which linearized estimations are based. Of course, there are also drawbacks associated with the MC methods. These are discussed later.

In the following, the general application of MC methods and the Metropolis-Hastings algorithm will be introduced. First, a short introduction to the probabilistic formulation of inverse problems will be given. The MC algorithm used in this thesis is described in the method section.

2.6.1 Probabilistic formulation

In a probabilistic formulation, $P(\mathbf{m}|\mathbf{d}_{obs}, I)$ describes the probability of the model, \mathbf{m} , given the data, \mathbf{d}_{obs} , and the prior information, I . It is referred to as the posterior probability distribution and combines prior information and data information using the Bayesian formulation (Malinverno, 2002),

$$P(\mathbf{m}|\mathbf{d}_{obs}, I) = \frac{P(\mathbf{m}|I)P(\mathbf{d}_{obs}|\mathbf{m}, I)}{P(\mathbf{d}_{obs}|I)}, \quad (2.36)$$

where $P(\mathbf{m}|I)$ is the prior distribution describing the prior information on the model parameters, and $P(\mathbf{d}_{obs}|\mathbf{m}, I)$ is the likelihood function, which describes the degree of fit between observed data and data predicted from the model \mathbf{m} . The denominator, $P(\mathbf{d}|I)$, is a normalizing constant, also called the evidence or Bayes' denominator, where

$$P(\mathbf{d}_{obs}|I) = \int P(\mathbf{m}|I)P(\mathbf{d}_{obs}|\mathbf{m}, I)d\mathbf{m}. \quad (2.37)$$

If the posterior probability distribution is mapped over the model space, then it will be possible to find the model with the highest probability giving the observed data and prior. One way of mapping the probability density is, as mentioned, an exhaustive search or letting a MC algorithm sample the distribution by visiting random models in the model space. Using a sampling method is a way to avoid evaluating the integral in Eq. (2.37)

2.6.2 Markov chain Monte Carlo

In the group of Monte Carlo methods, the Markov chain Monte Carlo (MCMC) method is often used. Instead of sampling unrelated models in the model space, as a plain MC method will do, the MCMC uses a random sampling procedure to build a chain of models in the model space - a Markov chain (Sambridge & Mosegaard, 2002). In the Markov chain the next model only depends on the current model and not any of the previous visited models. The chain will, if everything goes right, converge toward the desired posterior probability distribution.

2.6.3 Metropolis-Hastings

A widely used MCMC sampler is the Metropolis-Hastings algorithm (Metropolis *et al.*, 1953). The algorithm samples models in a Markov chain directly from a posterior

probability distribution. The algorithm takes the following steps after a start model is defined:

A proposal distribution, $q(\mathbf{m}|\mathbf{m}_c)$, is chosen to describe the possibility of going from the current model, \mathbf{m}_c , to any other model. A new model, \mathbf{m}_{new} , is then drawn from the proposal distribution. The distribution is often a Gaussian distribution centered around the current model, but it may take any shape.

Hereafter, an acceptance probability, α , is computed. The acceptance probability determines the probability of accepting the new model in the Markov chain. It is given by (Malinverno, 2002):

$$\alpha(\mathbf{m}_c, \mathbf{m}_{new}) = \min \left[1, \frac{P(\mathbf{m}_{new}|\mathbf{d}, I)}{P(\mathbf{m}_c|\mathbf{d}, I)} \cdot \frac{q(\mathbf{m}_c|\mathbf{m}_{new})}{q(\mathbf{m}_{new}|\mathbf{m}_c)} \right]. \quad (2.38)$$

Using Eq. (2.36) to describe the posterior probability distributions in the equation above, we see that the normalization constant, Bayes' denominator, cancels itself out. So, the equation becomes

$$\alpha(\mathbf{m}_c, \mathbf{m}_{new}) = \min \left[1, \frac{P(\mathbf{m}_{new}|I)}{P(\mathbf{m}_c|I)} \cdot \frac{P(\mathbf{d}|\mathbf{m}_{new}, I)}{P(\mathbf{d}|\mathbf{m}_c, I)} \cdot \frac{q(\mathbf{m}_c|\mathbf{m}_{new})}{q(\mathbf{m}_{new}|\mathbf{m}_c)} \right], \quad (2.39)$$

Which in words can be describes as

$$\alpha(\mathbf{m}_c, \mathbf{m}_{new}) = \min[1, (\text{prior ratio}) \cdot (\text{likelihood ratio}) \cdot (\text{proposal ratio})]. \quad (2.40)$$

It is notable that the proposal ratio cancels out if the distribution is symmetrical as for a Gaussian distribution. In this case, Eq. (2.39) reduces to

$$\alpha(\mathbf{m}_c, \mathbf{m}_{new}) = \min \left[1, \frac{P(\mathbf{m}_{new}|I)}{P(\mathbf{m}_c|I)} \cdot \frac{P(\mathbf{d}|\mathbf{m}_{new}, I)}{P(\mathbf{d}|\mathbf{m}_c, I)} \right]. \quad (2.41)$$

If the prior information is assumed to be a uniform distribution, e.g. if boundaries are put on the model space geometry, then the prior ratio also cancels out and only the likelihood ratio is left, so the acceptance probability of the new model becomes

$$\alpha(\mathbf{m}_c, \mathbf{m}_{new}) = \min \left[1, \frac{P(\mathbf{d}|\mathbf{m}_{new}, I)}{P(\mathbf{d}|\mathbf{m}_c, I)} \right]. \quad (2.42)$$

So, the new model is accepted in the Markov chain with probability α and rejected with probability $(1 - \alpha)$:

- If $P(\mathbf{d}|\mathbf{m}_{new}, I) > P(\mathbf{d}|\mathbf{m}_c, I)$, then the new model is always accepted.
- If $P(\mathbf{d}|\mathbf{m}_{new}, I) < P(\mathbf{d}|\mathbf{m}_c, I)$, then the new model is accepted with probability $\frac{P(\mathbf{d}|\mathbf{m}_{new}, I)}{P(\mathbf{d}|\mathbf{m}_c, I)}$.

To phrase it more generally, every time a new model is proposed, the model is compared to the current model. If the probability of the new model is higher than the probability of the current model, then the acceptance probability, α , is one, and the model is accepted. If the probability of the new model is lower than the probability of the current model, then the model will be accepted with probability α . This theory is the foundation of the MCMC code used in this thesis. The MCMC code is described in the following method section.

3 Method - MCMC algorithm

The method section in this thesis is divided into two chapters. The first method chapter, Chapter 3, is a description of the Markov chain Monte Carlo (MCMC) algorithm and a description of the generation of synthetic data. The second method chapter, Chapter 4, presents the studies that are carried out in order to answer the research questions given in the introduction.

3.1 MCMC algorithm

In this section, the MCMC inversion algorithm will be presented. The algorithm is written in Fortran by C. Kirkegaard, Aarhus University, and is implemented in the inversion software AarhusInv (Auken *et al.*, 2014). The algorithm applies the forward code from Fiandaca *et al.* (2012) (see Section 2.5.1).

Before the algorithm could be applied to DCIP data, a range of tests and bug fixes have been completed as a part of this project. The bugs were fixed in cooperation with academic advisor Gianluca Fiandaca.

3.1.1 Parameterization in AarhusInv

In AarhusInv, a log-transform is applied to all data and model parameters (Auken & Christiansen, 2004), so

$$\mathbf{d}_{obs} = \{\log(\rho_{a,i}), \log(M_{i,j})\}; \quad (3.1)$$

$$i = 1 \dots N_{quads}; j = 1 \dots N_{gates},$$

where the apparent resistivity, ρ_a , is given for each quadrupole measurement, i , and the chargeability, M , is computed in each gate, j , of the IP decay. The model vector is

$$\mathbf{m} = \{\log(\rho_i), \log(m_{0,i}), \log(\tau_i), \log(C_i), \log(thk_j)\}; \quad (3.2)$$

$$i = 1, N_{layers}; j = 1, N_{layers} - 1,$$

where ρ_i is the resistivity and $m_{0,i}$, τ_i , and C_i are the Cole-Cole IP parameters of the layer i with thickness thk . The log-transform is applied to minimize nonlinearity and impose positivity.

3.1.2 MCMC inversion algorithm

The MCMC inversion algorithm is based on the Metropolis-Hasting sampling algorithm described in section 2.4.4. An overview of the algorithm is given in the flow chart in Figure 3.1. The steps of the chart are described in the following subsections.

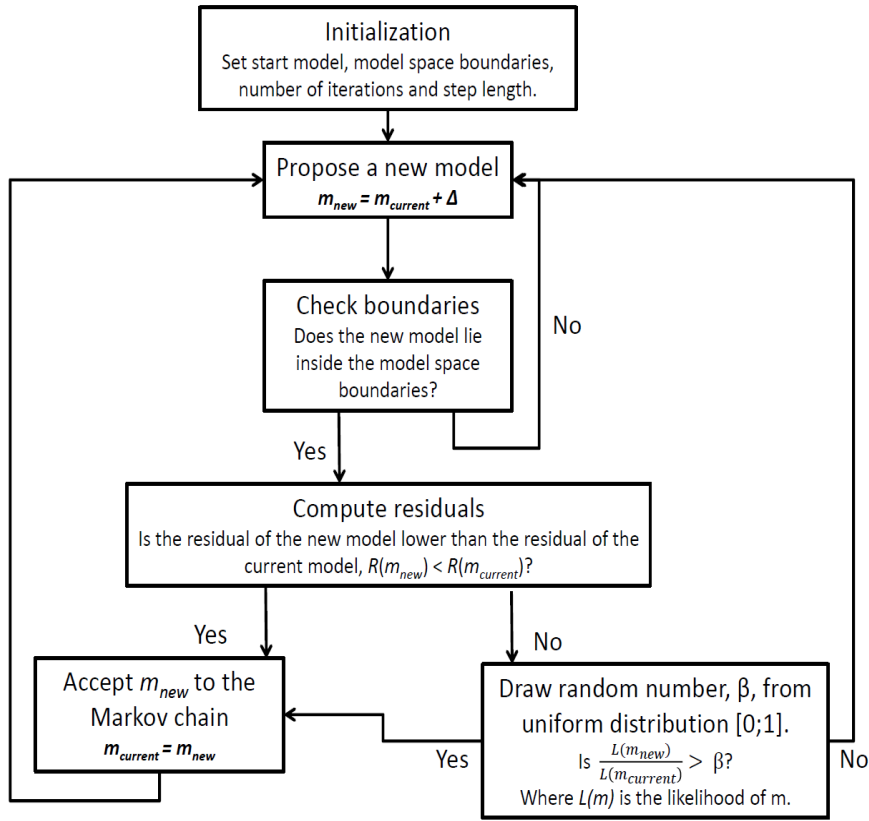


Figure 3.1: Flow chart of the MCMC algorithm used in this thesis to analyze the sensitivity of DCIP data. The chart goes through the steps of a Metropolis-Hastings algorithm, which samples a target distribution of the model space. A new model, m_{new} , is proposed from a perturbation, Δ , added to the current model, $m_{current}$. The procedure ends after a predefined number of iterations.

3.1.3 Initialization

Before the Metropolis-Hasting sampling of the model space can begin, a start model for the Markov chain must be defined and reasonable limits must be placed on the model space geometry. A step length constant, a maximum model perturbation, and the number of iterations must also be defined.

Start model

The sampling start model is found by performing a linearized inversion in AarhusInv (described in Section 2.5). From the linearized result, ten random steps are taken in the model space to advance randomness. By performing the linearized inversion, the burn-in phase is minimized, because the start model is close to a minimum of the misfit function and therefore already in the area of a maximum of the posterior probability distribution (Figure 3.2). In this thesis, the linearized inversion is started in the true model when inverting synthetic data. This is done to simplify the process and to make sure that the linearized inversion finds the global minimum of the misfit function and not a local one. The validation of this approach is tested and evaluated later.

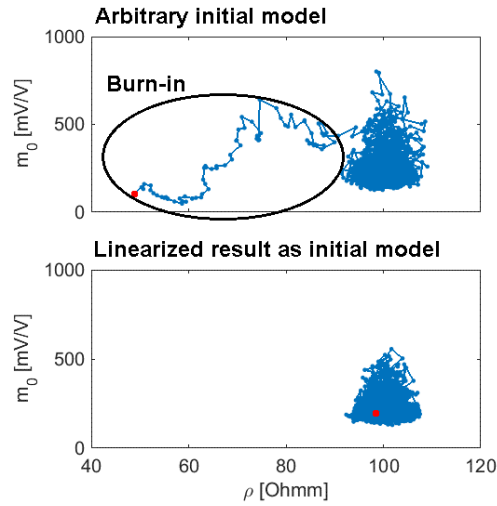


Figure 3.2: Top: Example of burn-in phase, where the start (initial) model, which is indicated by the red dot, is chosen arbitrary. Bottom: The start model is the resulting model of a linearized inversion and ten random steps. This method minimizes the burn-in phase.

Model space boundaries

To limit the sampling space, reasonable boundaries must be placed on the model space geometry. The boundaries are defined for each model parameter individually. The boundaries are shown in Table 3.1. The minimum and maximum values are not necessarily physical, but are based on experience from the MCMC results.

	ρ [Ωm]	m_0 [mV/V]	τ [s]	C [dim.less]	Thk [m]
Min value	1	0.1	10^{-5}	10^{-4}	0.1
Max value	$2 \cdot 10^4$	10^3	10^5	1	100

Table 3.1: Model space boundaries of the Cole-Cole parameters applied in the MCMC inversion.

Step length

A step length constant, k , is used to define the length of the perturbation between models in the Markov chain. k is determined by a trial and error process. It is important to choose a suitable step length constant for each individual inversion problem, because the step length have a direct influence on the model acceptance rate, which is the percentage of the visited models that are accepted to the Markov chain. A high acceptance rate indicates that the proposed models are very close to the current model, so the step length is relative small. The algorithm can become trapped in a local minimum of the misfit function, if the steps are too small. However, if the steps are too long, the convergence to an equilibrium distribution will take longer time and the acceptance rate will be small. The optimal step length constant is often found when the acceptance rate is 20-30% for high dimension problems and 30-40% for low dimension problems (Jacobsen, 2010).

3.1.4 Proposer algorithm

The algorithm that proposes the next model in the Markov chain is referred to as the model proposer. A new model, \mathbf{m}_{new} , is defined as

$$\mathbf{m}_{new} = \mathbf{m}_c + \Delta, \quad (3.3)$$

where Δ is the perturbation from the current model, \mathbf{m}_c . The perturbation is defined as

$$\Delta = \mathbf{L}\mathbf{n} \cdot k, \quad (3.4)$$

where \mathbf{n} is a vector of random numbers drawn from a Gaussian proposal distribution, k is the step length constant, and the lower triangular matrix, \mathbf{L} , is the Cholesky decomposition of the estimated covariance matrix of the MCMC start model (see section below). The proposer algorithm is shown in Appendix A.1.

The Cholesky decomposition

The Cholesky decomposition scales the perturbation for each Cole-Cole parameter according to their uncertainty and value range. The decomposition is given as (Golub & Van Loan, 1996):

$$\mathbf{C}_{est} = \mathbf{L}\mathbf{L}^T \quad (3.5)$$

By definition, this decomposition takes the square root of \mathbf{C}_{est} . When this is applied to the perturbation, it lets the algorithm take longer steps for the model parameters, which have a large uncertainty. If the decomposition is not applied, the algorithm will take relative small steps for e.g. the chargeability ($m_0 = 0.1-1000$ mV/V) and relative large steps for the frequency exponent ($C = 0-1$), because of the relative difference in interval width.

The scaling of the perturbation is not adaptive, meaning that the scaling is unchanged through the Markov chain. This keeps the transition probability distribution Gaussian and symmetric, so that the probability of going from \mathbf{m}_i to \mathbf{m}_{i+1} is the same as going from \mathbf{m}_{i+1} to \mathbf{m}_i :

$$P(\mathbf{m}_i|\mathbf{m}_{i+1}) = P(\mathbf{m}_{i+1}|\mathbf{m}_i) \quad (3.6)$$

Keeping the transition probability symmetric is not necessary, but it allows the use of the simple acceptance probability, found in Eq. (2.42).

3.1.5 Acceptance criterion

As the next step, the MCMC algorithm must determine whether the new model should be accepted to the Markov chain and the posterior probability distribution or not. Eq. (2.42) shows that the acceptance probability of the new model is a function of the likelihood $P(\mathbf{d}|\mathbf{m}, I)$. Because the observational errors are assumed Gaussian, the likelihood is defined as

$$P(\mathbf{d}|\mathbf{m}, I) = K \cdot \exp(-0.5 \cdot R), \quad (3.7)$$

where K is a normalization constant and R is the data residual (Jacobsen, 2010). By inserting Eq. (3.7) into Eq. (2.42), the acceptance probability becomes

$$\alpha(\mathbf{m}_c, \mathbf{m}_{new}) = \min[1, \exp[0.5 (R(\mathbf{m}_{new}) - R(\mathbf{m}_c))]], \quad (3.8)$$

where the residual,

$$R = \left[(\mathbf{d}_{obs} - \mathbf{g}(\mathbf{m}))^T \mathbf{C}_{obs}^{-1} (\mathbf{d}_{obs} - \mathbf{g}(\mathbf{m})) \right]^{1/2}, \quad (3.9)$$

is given as for the maximum likelihood method.

In practice, the MCMC algorithm computes the likelihood ratio,

$$\exp[0.5 (R(\mathbf{m}_{new}) - R(\mathbf{m}_c))], \quad (3.10)$$

and draws a random number, β , from a uniform distribution [0;1]. The probability of the random number to be below the likelihood ratio is equal to the acceptance probability (α). So, if

$$\beta < \exp[0.5 (R(\mathbf{m}_{new}) - R(\mathbf{m}_c))], \quad (3.11)$$

then the new model is accepted and \mathbf{m}_{new} becomes the new \mathbf{m}_c . The process described above is then repeated until the number of iterations reaches the defined value.

The MCMC algorithm saves the model vectors of the accepted models into an output file together with the data residuals. All the accepted models make up the posterior probability distribution.

3.2 Synthetic data

In the following section, the generation of synthetic data is described. This includes the electrode configuration, gating of the IP decay, and the construction of a noise model.

Synthetic datasets are computed by defining a geoelectric model parameterized by the Cole-Cole parameters and mapping the model into the data space. The model parameters, an electrode configuration, a gating, and a noise model are used as inputs for AarhusInv². AarhusInv then performs the forward computation and writes an output file containing the DC resistivity, the data space chargeabilities, and the standard deviation (STD) on each data point. This file is then used as input for the MCMC inversion.

3.2.1 Electrode configuration

All synthetic data are generated as Schlumberger soundings where the current electrodes and the potential electrodes are centered around the same point. For homogenous half-spaces, one quadrupole measurement is used for each sounding. The electrodes are placed so the spacing between the current electrodes, $|AB|$, is 55 m and the spacing between the potential electrodes, $|MN|$, is 5 m. This gives a geometric factor of approximately 470 m.

For models with three or more layers, the setup has 20 quadrupoles where the spacing between the electrodes increases approximately logarithmic. So, $|AB|$ is ranging from 7.5 m to 500 m and $|MN|$ is ranging from 2.5 m to 65 m. The electrode configurations are chosen to limit the geometric factor to 3000 m and thereby increasing the IP potential as seen in Eq. 2.10. The main penetration depth of each quadrupole setup is proportional to the spacing between the current electrodes (Christensen, 2012):

² A manual for AarhusInv describing the different types of input and output files are available on the HydroGeophysics Group webpage: www.hgg.geo.au.dk/HGGsoftware/em1dinv/em1dinv_manual.pdf

$$\text{main penetration depth} = 0.25 \frac{|AB|}{2} \quad (3.12)$$

So, with the listed setup, the maximum penetration is approximately 62,5 m.

3.2.2 Gateing

The gating of the IP decay is computed according to a standard used at the HydroGeophysics Group, Aarhus University. 22 gates with widths increasing approximately logarithmic between 1.06 and 1300 ms are computed. The widths of the gates are presented in Table 3.2.

A 100% duty cycle with three stacks is applied for each quadrupole measurement. Each pulse is 4000 ms. The time delay, i.e. the time from the sign of the current pulse is reversed to the first measurement is made, is 2.59 ms. The DC potential is measured 3350 ms after the start of the pulse.

Gate number	Gate width [ms]	Gate number	Gate width [ms]
1	1.06	12	40
2	1.33	13	60
3	2.13	14	80
4	2.93	15	100
5	4	16	140
6	5.33	17	200
7	7.46	18	280
8	10.4	19	380
9	14.4	20	540
10	20	21	760
11	20	22	1300

Table 3.2: Standard gating of IP signal. As a standard, 22 gates are used to compute the chargeability for synthetic data. The width of the gates are log-distributed from 1.06 ms to 1300 ms. The acquisition delay is 2.59 ms and the time of one pulse is 4 s.

3.2.3 Noise model

A Gaussian noise model can be added to the forward computation to simulate the noise level and the error bars gained from measurements in the field. The noise model defines the standard deviation (STD) on the apparent resistivity data on the chargeability data. Additional, a voltage threshold can be added.

The total STD on the i 'th data parameter is computed as

$$STD_{total,i}^2 = STD_{uniform,i}^2 + STD_{vth,i}^2, \quad (3.13)$$

where $STD_{uniform}$ is the STD on the apparent resistivity and the chargeability and the voltage threshold, STD_{vth} , is computed as

$$STD_{vth,i} = \frac{V_{TH}}{V_{IP,i}} \cdot \frac{\sqrt{Nominal\ width}}{\sqrt{Gate\ width\ (i)}} \cdot \frac{1}{\sqrt{N_{stacks}}}, \quad (3.14)$$

where V_{TH} is the voltage threshold for a nominal gate width, which is 10 ms. The equation defines that the STD is proportional to one over the square root of the number of stacks. So, as the number of stacks is increased the STDs on the data decrease. The vector STD_{total}^2 defines the diagonal of the covariance matrix C_{obs} . The errors are assumed uncorrelated, why the off-diagonal of the matrix is zero.

In this thesis, different noise models have been used for homogenous half-spaces and multi-layer models. For multi-layer models, a 2% STD is added to the apparent resistivity and a 10% STD is added to the chargeability. Additionally, a voltage threshold of 0.1 mV is added to the data. This is comparable with the noise level in the field (Gazoty *et al.*, 2013). For homogenous half-spaces, the noise on the chargeability is decreased to 5%, because it is expected that a forward response can be fitted to the observed data within smaller error bars for this simplified model.

In AarhusInv, it is also possible to add a random perturbation to the IP decays according to the defined STD. This can be done to imitate the decays recorded in the field. Because the perturbation is random, it cannot be duplicated, why it has not been added in the synthetic data in this thesis.

4 Method - DCIP studies

The aim of this thesis is to analyze Cole-Cole parameters extracted from time-domain DCIP data. This is done through a series of different studies using the Markov chain Monte Carlo (MCMC) algorithm described in the previous chapter. The purposes of the individual studies are described below together with the methods for exploring the individual problems.

4.1 Study of proposer algorithm

To illustrate the effect of the novel MCMC algorithm with the covariance scaled model proposer, the algorithm is tested against a standard Gaussian proposer. The resulting posterior probability distributions and the convergence rates of the two algorithms are compared.

4.1.1 Gaussian model proposer

A new standard Gaussian proposer algorithm has been implemented in the MCMC algorithm in AarhusInv as part of this study. The covariance scaled proposer and the Gaussian proposer use the same MCMC algorithm, and only minor changes have been made in the code to implement the second proposer. For the Gaussian proposer, the equation of the model perturbation, Δ , in the Markov chain is simplified to

$$\Delta = \mathbf{n} \cdot k, \quad (4.1)$$

where \mathbf{n} is a vector of random numbers drawn from a Gaussian distribution and k is the step length constant. A new model, \mathbf{m}_{new} , is computed from the current model, \mathbf{m}_c , as

$$\mathbf{m}_{new} = \mathbf{m}_c + \Delta = \mathbf{m}_c + \mathbf{n} \cdot k. \quad (4.2)$$

The code written for the Gaussian proposer is presented in Appendix A.1.

4.1.2 Comparative analysis

A simple geoelectric model of a homogenous half-space has been chosen to compare the two model proposers to ensure a good resolution. The model parameters are defined as: $\rho = 100 \Omega\text{m}$, $m_0 = 200 \text{ mV/V}$, $\tau = 0.01 \text{ s}$ and $C = 0.6$.

Synthetic data are generated from the model with the settings described in Section 3.2. The generated dataset is then inverted with both the Gaussian and the covariance scaled proposer algorithm. Many inversions are performed with each proposer, and for each inversion a different number of iterations is used. The step length constant is determined by trial and error. The aim is to find the step length that gives a model acceptance rate of approximately 30%.

For each inversion result, the marginal posterior probability distributions of the Cole-Cole parameters are plotted as histograms. A curve is fitted to each histogram and then normalized by the area below the curve. In this way, distributions containing a different number of models become comparative. When the resulting curves are plotted together it will give a picture of the convergence rate of the two proposer algorithms. The modeling

procedure is presented in Appendix A.2 and the results of the comparison are presented in Section 5.1.

4.2 Study of a homogenous half-space

Can the spectral Cole-Cole parameters be resolved from time-domain DCIP data and how well can they be resolved? This is investigated with a full sensitivity analysis based on MCMC inversion results.

In the following, methods for testing the stability of the MCMC algorithm are described. The purpose of the tests is to ensure consistency of the MCMC inversion results. Hereafter, the methods behind the actual sensitivity analysis are presented.

4.2.1 Convergence study for a homogenous half-space

Before the sensitivity analysis is carried out, the consistency of the MCMC inversion results, which the sensitivity analysis relies on, must be tested. This is done by repeating the same inversion multiple times and comparing the results. If consistency is not obtained, the number of iterations or the step length constant should be adjusted in the MCMC inversion settings.

The following Cole-Cole model has been chosen for the tests: $\rho = 100 \text{ } \Omega\text{m}$, $m_0 = 200 \text{ mV/V}$, $\tau = 1 \text{ s}$ and $C = 0.6$. These model parameters produce an IP decay with a relative high chargeability and signal-to-noise ratio, which ensures resolution of the parameters. τ is chosen so it is within the acquisition range (2.59-4000 ms). Synthetic data are generated from the model with the settings described in Section 3.2.

Additionally, the inversion results are compared to the result of an inversion, where the start model is a random model instead of being the result of a linearized inversion. This is done to ensure that the MCMC algorithm finds the same equilibrium despite the different start positions.

The inversion results are plotted with a script presented in Appendix A.2.

4.2.2 Sensitivity analysis of a homogenous half-space

The sensitivity analysis of the Cole-Cole parameters are based on computations of the standard deviation factors (STDFs) of the individual parameters.

For the MCMC inversion results, it is possible to compute the STDFs from the standard deviations (STDs) of the marginal posterior probability distributions. The STD is computed as

$$STD = \sqrt{\frac{1}{N-1} \sum_{i=1}^N |x_i - \mu|^2}, \quad (4.3)$$

where \mathbf{x} is a vector containing all the N accepted values of one of the Cole-Cole parameters. μ is the mean of \mathbf{x} given as

$$\mu = \frac{1}{N} \sum_{i=1}^N x_i. \quad (4.4)$$

Because the Cole-Cole parameters are presented with the base-10 logarithm in this thesis, the STDF is computed as

$$STDF = 10^{STD(\log_{10} x)}. \quad (4.5)$$

The computations of the STDFs are carried out with a script presented in Appendix A.2. The STDFs are computed for a sweep of models, which all are variations of the model described previously. The parameter combinations are shown together with the results of the study in Section 5.3.

To assess the quality of a linearized inversion approach, the STDFs of the MCMC inversion results are compared to the sensitivity analysis given by the linearized inversion in AarhusInv. Here, the STDFs are computed by evaluation of the estimated covariance matrix, C_{est} , as described in Section 2.33.

4.3 Study of Ghorbani *et al.* (2007)

In this study, Cole-Cole models previously analyzed by Ghorbani *et al.* (2007) in time-domain and frequency-domain are examined.

Ghorbani used a Bayesian approach to invert synthetic IP data. The aim of their study was to compare inversion results of time-domain and frequency-domain IP data. The study showed that the uncertainties associated with the Cole-Cole parameters are much higher for measurements performed in time-domain compared to those of the frequency-domain. Based on an observed nonlinearity and non-uniqueness of the solutions, the study concluded, that it is very difficult, if not impossible, to resolve Cole-Cole parameters from time-domain data using standard least-squares methods.

In this thesis, the same Cole-Cole models as used by Ghorbani will be studied. This is done to compare their results from time-domain to the results of the MCMC inversion and to assess their conclusions.

The Cole-Cole parameters of the models are presented in Table 4.1. The same gating, acquisition range, and model space boundaries as used by Ghorbani (Table 4.2) are applied for the MCMC inversion. The IP data acquisition is performed over two decades (20-2000 ms) with a total of 20 gates and a 50% duty cycle waveform. No noise model is added to the forward responses.

STDFs are computed for all the MCMC results to analyze the uncertainty and the resolution of the models. The inversion results are visualized using the script described in Appendix A.2. The results of this study are presented in Section 5.3.

	ρ [Ωm]	m_0 [mV/V]	τ [s]	C [dim less]
Model 1	100	800	0.01	0.25
Model 2	100	200	0.01	0.75
Model 3	100	200	0.01	0.25
Model 4	100	800	10	0.75
Limits	0 - $2 \cdot 10^3$	0 - 10^3	10^{-4} - 10^4	0 - 1

Table 4.1: Cole-Cole parameters of four homogenous half-space models and the limits of the model space geometry applied by Ghorbani et al. (2007). The same settings are used in this thesis to reproduce the inversion results of synthetic data generated from the models.

Gate number	Gate width [ms]	Gate number	Gate width [ms]
1	20	13	110
2-4	30	14	120
5-6	40	15	130
7	50	16	140
8	60	17	150
9	70	18	160
10	80	19	180
11	90	10	200
12	100		

Table 4.2: Gating of a IP signal used by Ghorbani *et al.* (2007). The acquisition delay, dly , is minimum 20 ms and the injected current waveform has a 50% duty cycle. The same settings are applied to reproduce their results using a MCMC inversion.

4.4 Study of acquisition ranges

This study focuses on the acquisition time required to resolve Cole-Cole parameters from time-domain DCIP data. The acquisition time, or acquisition range, refers here to the time from the first to the last measurement on the IP decay. In this study, five different acquisition ranges are compared. Apart from the previously introduced standard gating (Table 3.2) and the gating used by Ghorbani *et al.* (2007) (Table 4.2), three new gate settings are used. These are presented in Table 4.3.

The comparative analysis is carried out on the model also used in Section 4.1: $\rho = 100 \Omega\text{m}$, $m_0 = 200 \text{ mV/V}$, $\tau = 0.01 \text{ s}$ and $C = 0.6$. Synthetic data are generated from the model with

the noise model presented in Section 3.2. The STDFs are computed for the MCMC inversion results with the method described previously. The forward responses, the MCMC inversion results, and the computed STDFs are presented in Section 5.4.

	dly [ms]	Time of pulse [ms]	Number of Gates	Min. and max. gate width [ms]
One decade	100	1000	10	20-200
Two decades	10	1000	20	2.66-200
Four decades	1	10,000	40	0.26-2060

Table 4.3: Description of acquisition range and gating for one, two and four decade data acquisition. *dly* is the acquisition delay before measurements are started (see Section 3.2.2).

4.5 Study of layered models

In order to test the MCMC algorithm on non-homogenous half-spaces, a three-layer model and a five-layer model have been produced. The models are specified in Table 4.4 and Table 4.5 respectively. The aim of this study is to test the resolution of the Cole-Cole parameters on layered models with different acquisition ranges and to investigate the correlations between the parameters.

The three-layer model has previously been used by Fiandaca *et al.* (2012) to test different forward modeling approaches. The value of C is changed from $C = 0.8$ in the paper to $C = 0.6$ for this MCMC analysis. This is done because a C value above 0.6 is non-physical (Pelton *et al.*, 1978a). This model is referred to as Model A.

To test the limits of the time-domain DCIP method, a version of Model A is computed with a smaller C value. This model is referred to as Model B. Furthermore, a third version is generated with the use of a smaller acquisition range. This model is referred to as Model C and the acquisition range used is the two decade gating described in Table 4.3.

A five-layer model, Model D, is constructed with 5 m thick layers with alternating resistivities and chargeabilities. Layer one, three and five have a low resistivity and a high chargeability, which could be the responses of clay layers (Dinesen, 1962). Layer two and four have a higher resistivity and a lower chargeability which are comparable to the responses of a sandy till. Model D thereby represents a geological model with alternation clay and till layers.

Synthetic dataset are generated from the models as described in Section 3.2. STDFs are computed for the MCMC results. Additionally, an analysis of the correlations between the Cole-Cole parameters is carried out. The method is described in the following section.

Model A, B and C	Layer 1	Layer 2	Layer 3
ρ [Ωm]	20	20	20
m_0 [mV/V]	5	300	5
τ [s]	0.08	8	1
C [dim less]	0.6 (0.3)	0.6 (0.3)	0.6 (0.3)
Thickness [m]	7	7	

Table 4.4: Cole-Cole parameters describing a three-layer model. Three different versions of the model are used for MCMC inversion analyses. Model A: The model described in the table, where a standard gating and acquisition range (2.59-4000 ms) are applied. Model B: The model takes the same values as Model A, but $C = 0.3$ as indicated in the brackets in the table. Model C: The model takes the same parameter values as Model A, but the acquisition range is smaller (10-1000 ms).

Model D	Layer 1	Layer 2	Layer 3	Layer 4	Layer 5
ρ [Ωm]	20	200	20	200	20
m_0 [mV/V]	300	50	300	5	300
τ [s]	0.1	1	0.01	10	0.1
C [dim less]	0.6	0.6	0.6	0.6	0.6
Thickness [m]	5	5	5	5	

Table 4.5: Cole-Cole parameters describing a five-layer model referred to as Model D. Model D resembles the response of a geological model with alternating clay and till layers.

4.5.1 Parameter correlation

One of the benefits of performing a MCMC analysis is the ability to study the cross-correlations between the model parameters.

In this thesis, the Person's correlation coefficient (PCC) is computed to measure the degree of correlation between the Cole-Cole parameters. PCC is a measure of the linear correlation between two variables and is simply a normalization of the covariance of the model parameters. It is defined as the covariance of the two variables, x and y , divided by the product of their STD (Barlow 1989):

$$PCC_{x,y} = \frac{cov(x,y)}{STD_x STD_y}. \quad (4.6)$$

PPC is a number between -1 and 1, where 1 is a total positive correlation, 0 is no correlation, and -1 is a total negative correlation (anti-correlation). The relationship between the Cole-Cole parameters is expected to show some degree of nonlinearity, why the PCC is computed for the base-10 logarithm of the parameter values to increase linearity. A correlations matrix is computed and plotted with a script described in Appendix A.2.

4.6 Study of resistivity equivalence

This study investigates resistivity equivalences in DC and DCIP data. The aim is to understand the role of the IP signal, especially the chargeability, when it comes to resolving ρ - thk equivalences. This can be assessed by studying the uncertainties and the correlations of the model parameters.

Equivalent models produce model responses (IP signals), which are identical within the uncertainties given by the noise model (Christensen, 2012). In some cases, the equivalent models will be similar, meaning that the model uncertainty is small. In other cases, very different models can produce similar responses, meaning that one or more model parameters are very uncertain. An example of this is high resistivity equivalence.

For models with high resistivity equivalence the relationship between the resistivity of the layers is as follows: $\rho_1 < \rho_2 > \rho_3$. This is representative for a sand or gravel layer imbedded in a formation with finer grained material (Dinesen, 1962). It is often difficult to resolve the thickness and the resistivity of the high resistivity layer in such a model, however, the resistance can sometimes be determined. The resistance is

$$T_i = \rho_i \cdot tkh_i, \quad (4.7)$$

where T_i is the resistance of the i 'th layer.

The opposite of high resistivity equivalence is low resistivity equivalence, where $\rho_1 > \rho_2 < \rho_3$. As an example, this would be representative for a clay layer imbedded in a sand formation. Here, the conductance is sometimes resolved even though the thickness and the resistivity of the middle layer are not. The conductance of the i 'th layer is

$$S_i = \frac{tkh_i}{\rho_i}. \quad (4.8)$$

The resistivity equivalences are studied from Model E and Model F, which are described in Table 4.6 and Table 4.7, respectively. To investigate the equivalences, variations of the two default models are examined. The thickness of the middle layer is varied to see how it affects the parameter uncertainties. Furthermore, the chargeability of the middle layer is varied to understand the role of the contrast in the chargeability.

The MCMC inversion is carried out on DCIP data, but also on DC data alone. This is done to see what information is added by the IP part of the signal. The synthetic data are generated as described in Section 3.2. STDFs and correlation coefficients are computed with the method described previously. The results are presented in Section 5.6.

Model E	Layer 1	Layer 2	Layer 3
ρ [Ωm]	20	200	20
m_0 [mV/V]	5	300	5
τ [s]	0.08	1	0.8
C [dim less]	0.6	0.6	0.6
Thickness [m]	10	5	

Table 4.6: Cole-Cole parameters describing a three-layer model, Model E, which has a high resistivity equivalence.

Model F	Layer 1	Layer 2	Layer 3
ρ [Ωm]	200	20	200
m_0 [mV/V]	5	300	5
τ [s]	0.08	1	0.8
C [dim less]	0.6	0.6	0.6
Thickness [m]	10	5	

Table 4.7: Cole-Cole parameters describing a three-layer model, Model F, which has a low resistivity equivalence.

4.7 Study of IP

This study investigates to what extent an imbedded layer in a three-layer model can be resolved from a layer contrast in just one of the IP parameters. This is done to understand what information the IP signal brings to the DCIP method and to test the capability of the different Cole-Cole parameters to resolve layer boundaries.

Firstly, a model is computed with a factor ten contrast in the resistivity: $\rho = [200, 2000, 200]$ Ωm . The remaining parameters are as defined for Model G (Table 4.8). For this model, a DC and a DCIP inversion are carried out with the MCMC approach to see if the IP part of the signal helps to resolve layer thicknesses even though no contrasts or layering are present in the IP parameters.

Secondly, all the Cole-Cole parameters in Model G are kept constant down through the profile, so that the model is homogenous. One of the IP parameters is then changed in the middle layer, to see if this causes an equivalence or if the contrast is enough to resolve the thickness of the layer. The STDFs are computed for a sweep of model to determine the limits of resolution.

Synthetic data are generated from the models as described in Section 3.2. STDFs and correlation coefficients are computed with the method described previously. The resulting correlation matrixes are presented in Appendix A.7 and will be applied for a

more general discussion of parameter correlations in the discussion chapter. The main results are shown in Section 5.7.

Model G	Layer 1	Layer 2	Layer 3
ρ [Ωm]	20	20	20
m_0 [mV/V]	50	50	50
τ [s]	1	1	1
C [dim less]	0.6	0.6	0.6
Thickness [m]	10	5	

Table 4.8: Cole-Cole parameters describing a three-layered model, Model G, with no contrast between the layers, so the model is actually homogenous.

4.8 Field example

In this study, real field data are used to compare inversion results from the linearized inversion approach and the MCMC method. The aim is not to make a geophysical interpretation of the data, but to see if the tendencies observed from synthetic data regarding uncertainties and parameter correlations can be applied to real field data as well.

The inversions are carried out on a 1D model, which is part of a larger 2D dataset acquired at Samsø, Denmark. The measurements are carried out as part of the project GEOCON³, where the subsurface around an old landfill is mapped with different geophysical methods. The geology in the area is characterized by shifting layers of glacial clay, silt and sand tills, and meltwater deposits.

29 quadrupoles were used for the 1D Schlumberger sounding setup. The electrode spacing was in the range: $|AB| = 45 - 260$ m and $|MN| = 5 - 30$ m. The measurements were performed with a 100% duty cycle and a gating comparable to the standard gating described in Table 3.2. The data have been processed by the GEOCON project, where outliers have been removed. The resulting IP decays are shown in Figure 4.1. The STDs on the chargeability data are 10-22% with an average of 11%.

The number of layers applied to the data in the inversions is determined by a trade-off between the data misfit and the complexity of the model in terms of the number of layers. Here, a linearized inversion is used to estimate the best trade-off by inverting the data with one to ten layers and comparing the resulting data misfits.

For the resulting model, the STDFs are calculated for the linearized approach and the MCMC and a correlation matrix is computed for the MCMC posterior probability distributions with the methods described previously. The results of the inversions are presented in Section 5.8.

³ GEOCON: Advancing GEOlogical, geophysical and CONtaminant monitoring technologies for contaminated sites: <http://www.env.dtu.dk/english/Research/WRE/GEOCON>

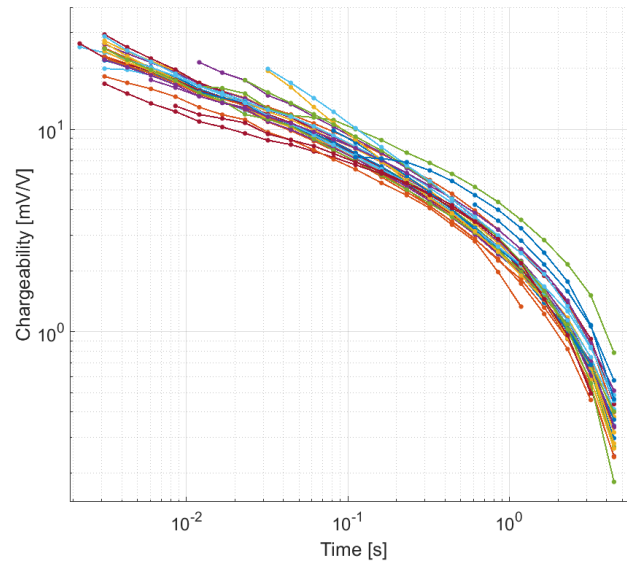


Figure 4.1: Resulting IP decays from an environmental survey at Samsø, Denmark. The decays were measured with a 29 quadrupole setup and a 100% duty cycle. The standard deviations on the data are 10-22% with an 11% average.

5 Results

In this chapter the results of the Markov chain Monte Carlo (MCMC) studies of the DCIP data are presented. The results are given in the same order as the methods of the studies were presented in the previous chapter.

5.1 Proposer algorithms

Synthetic DCIP data were generated from the model: $\rho = 100 \Omega\text{m}$, $m_0 = 200 \text{ mV/V}$, $\tau = 0.01 \text{ s}$ and $C = 0.6$. The data were inverted with two different proposer algorithms and a different number of iterations.

Figure 5.1 shows the resulting marginal posterior probability distributions of the time constant, τ , which is commonly the Cole-Cole parameter with the largest uncertainty. The results are shown for the two different model proposer algorithms: The covariance scaled proposer and the Gaussian proposer. In each plot, the different line styles show the different number of iterations, which has been used to obtain the different distributions. The figures for the remaining Cole-Cole parameters are shown in Appendix A.3.

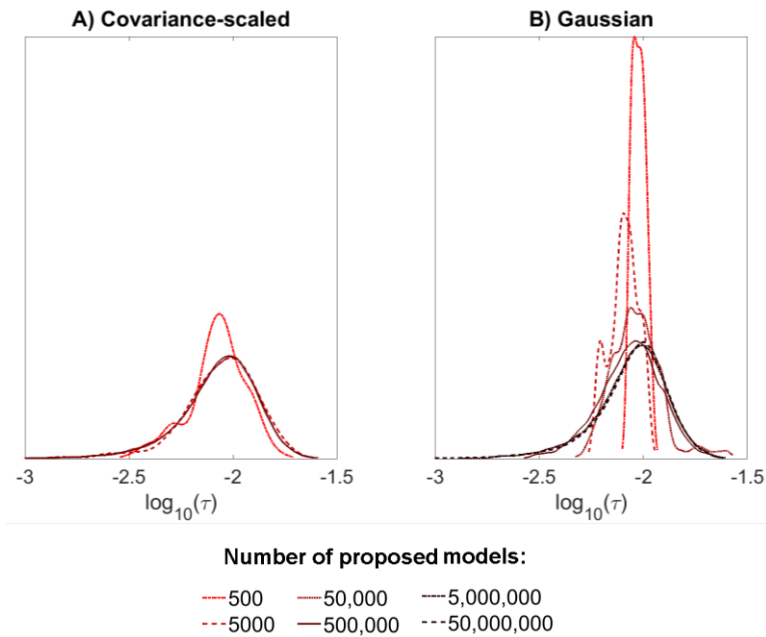


Figure 5.1: Normalized marginal posterior probability distributions of the time constant, τ , resulting from two different proposer algorithms: A) covariance scaled proposer (A) and a Gaussian proposer (B). The figure illustrates that the covariance scaled proposer converges faster (after 5000 iterations) compared to the Gaussian proposer, which needs more than 500,000 iterations to converge.

The two proposer algorithms find approximately the same distributions. As seen in the figure, the Markov chain produced with the covariance scaled proposer converges after 5000 iterations, which means that after 5000 iterations the distribution does not change

shape anymore. The chain from the Gaussian proposer converges after approximately 1,000,000 iterations. Consequently, the covariance scaled proposer reduces the computation time from approximately one day to 10 min for one MCMC inversion of a homogenous half-space running on 10 CPUs. The figure also shows that the two proposer algorithms search the model space equivalently, why it can be justified to use the faster novel proposer algorithm, which is used throughout this thesis.

5.2 Homogenous half-space

Synthetic data were computed from the model: $\rho = 100 \Omega\text{m}$, $m_0 = 200 \text{ mV/V}$, $\tau = 1 \text{ s}$, $C = 0.6$. The data were then inverted using the MCMC algorithm. 50,000 iterations and a step length constant of $k = 0.9$ were used. The resulting acceptance rate of models was 33%.

The resulting marginal posterior probability distributions are shown in Figure 5.2. The histograms along the diagonal show the distributions of the Cole-Cole parameters in \log_{10} with the true model values marked with red. The off-diagonals are cross-plots of all combinations of the four parameters.

The distributions are bell-shaped and unimodal with a single maximum for all the Cole-Cole parameters. The maxima correspond very well with the true model. The cross-plots indicate strong correlations between chargeability, m_0 , and the frequency exponent, C .

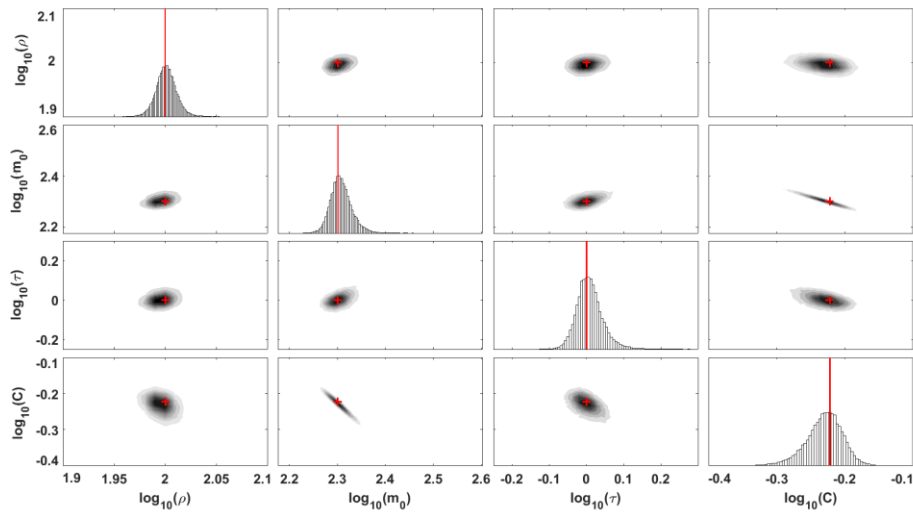


Figure 5.2: The posterior probability distribution of the homogenous half space: $\rho = 100 \Omega\text{m}$, $m_0 = 200 \text{ mV/V}$, $\tau = 1 \text{ s}$, $C = 0.6$. The diagonal shows histograms of the marginal distributions of the Cole-Cole parameters. The off-diagonal shows the density of the cross-correlations between the parameters. The true model parameters are indicated in red. Note that the figure is symmetric about the diagonal.

5.2.1 Convergence of a homogenous half-spaces

Six inversions were computed for the homogenous half-space problem. They all show approximately the same posterior probability distributions. In Figure 5.3, the distribution of τ is shown. The six distributions are approximately identical.

Figure 5.4 shows the cross-plots between τ and m_0 . Each blue dot is an accepted model. The six densities are almost identical in shape and location of maximum. At the edges, however, the densities are slightly different. It is expected from random-walks that the low density regions have different patterns.

The MCMC inversion results presented until now, have had a start model very close to the true model. If the data were not synthetic, but real field data, the true model would not be known and the inversion had to start from an arbitrary point in the model space. Figure 5.5 shows that the MCMC inversion reaches the same equilibrium distributions whether it is started from the true model or a model outside the maximum of the posterior probability distribution. The only difference between the results is the burn-in period.

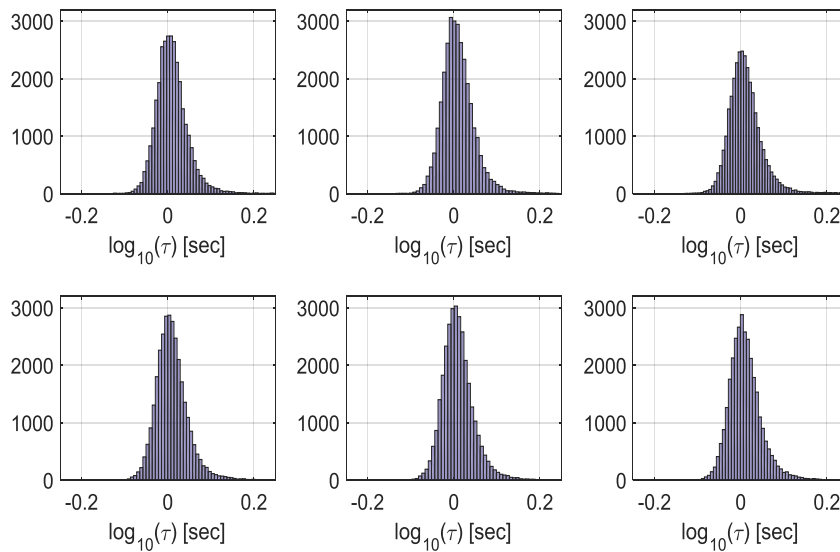


Figure 5.3: Marginal posterior probability distribution of τ from six different MCMC inversions of the same data. The distributions are approximately identical after 50,000 iterations, which is a good indication of convergence and consistency in the MCMC algorithm. The true model value is $\tau = 1$ s.

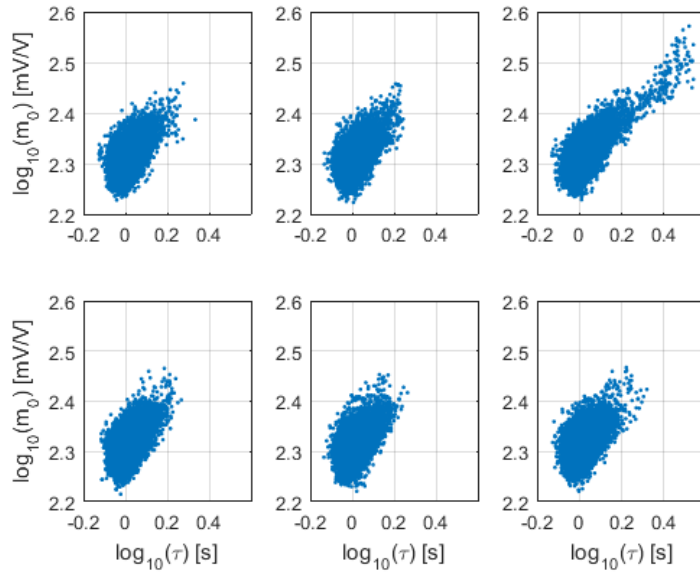


Figure 5.4: Cross-plots of τ and m_0 from six different MCMC inversions of the same dataset. The plots are approximately identical after 50,000 iterations, which is a good indicator of convergence and consistency in the MCMC algorithm. The true model values are $\tau = 1$ s and $m_0 = 200$ mV/V.

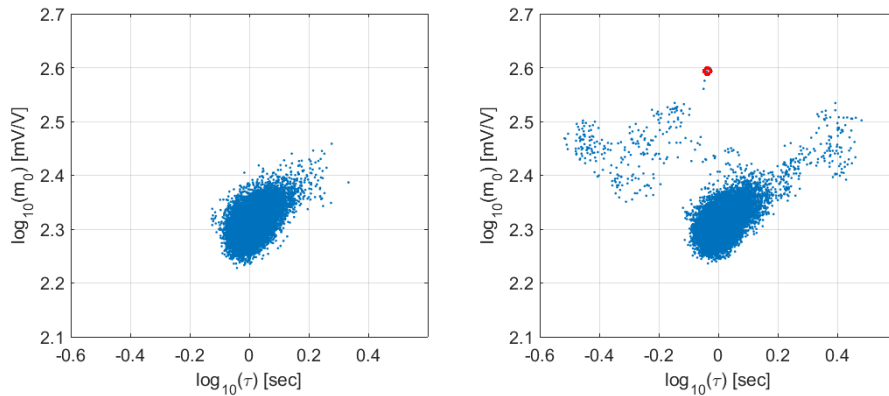


Figure 5.5: Effect of different start models used for a MCMC inversion. Left: The start model is ten steps from a result of a linearized inversion started at the true model. This means that the MCMC start model is located in a maximum of the posterior probability distribution. Right: The start model (red circle) is chosen randomly and is located outside the maximum of the posterior probability distribution. The plots show that the start model does not influence the result of the MCMC inversion. The only difference is the burn-in phase.

5.2.2 Sensitivity analysis of a homogenous half-space

STDFs of the inversion results presented in Figure 5.2 are plotted in Figure 5.6 - Figure 5.10. The plots show the standard deviation factors (STDFs) for both the MCMC inversion

(dashed lines) and the linearized approach (solid lines). In each plot, one of the model parameters is varied, so the results are shown for a sweep of models.

In Figure 5.6, the resistivity, ρ , is varied from $\rho = 10 \text{ } \Omega\text{m}$ to $\rho = 1000 \text{ } \Omega\text{m}$. The remaining model parameters are kept constant. The plot shows the STDFs of ρ in red, m_0 in green, τ in blue, and C in yellow. For the tested models, all the Cole-Cole parameters are well-resolved with STDFs < 1.2 . This is the case for both the MCMC and the linearized approach, why the two uncertainty analyses match well.

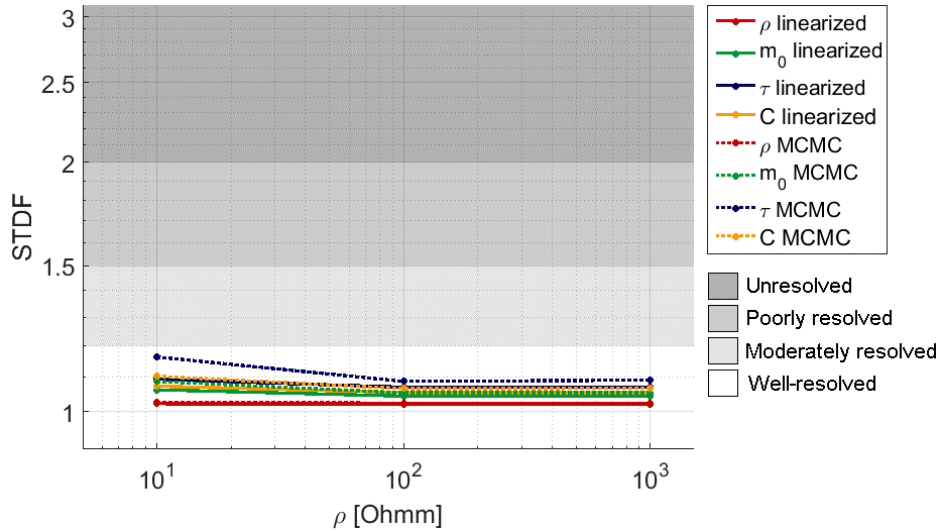


Figure 5.6: Standard deviation factor (STDF) as a function of the resistivity, ρ . ρ is varied from 10-1000 Ωm while the remaining Cole-Cole parameters are kept constant: $m_0 = 200 \text{ mV/V}$, $\tau = 1 \text{ s}$ and $C = 0.6$. The STDFs are computed from the results of a linearized inversion (solid line) and a MCMC inversion (dashed line).

Figure 5.7 shows the STDFs as a function of different m_0 values. m_0 is varied from 5 - 800 mV/V. The Cole-Cole parameters are all well-defined for $m_0 > 50 \text{ mV/V}$. As m_0 gets below 50 mV/V, the resolution decreases. For $m_0 = 5 \text{ mV/V}$, the MCMC results have STDFs > 2 , which means that the IP parameters are unresolved. However, the linearized approach finds that all parameters are well-resolved.

The black line in Figure 5.8 shows the average standard deviation (STD) on the IP data for the models also presented in Figure 5.7. The STD increases as m_0 decreases, which means that the signal-to-noise ratio decreases because the voltage threshold begins to influence the data. High STDs on the data are seen for the models, which also have high STDFs on the Cole-Cole parameters.

Figure 5.9 shows how the STDFs change as τ is changed. The model parameters are best resolved when τ is in the range of approximately 0.01-1 s. Higher or lower values will increase the STDFs of m_0 and τ itself. ρ and C only show a decrease in resolution with increasing τ values, but are well-resolved in all the models. The linearized approach and the MCMC finds approximately the same results for $\tau < 100 \text{ s}$.

The last figure, Figure 5.10, shows STDFs as a function of C . The resolution of the IP parameters decrease for decreasing values of C . For $C = 0.5-0.6$, all Cole-Cole parameters

are well-resolved with $STDF < 1.2$. For $C < 0.5$, the STDFs computed from the MCMC and the linearized approach do not agree. For $0.4 \geq C \geq 0.2$, the linearized approach underestimates the uncertainties of C , m_0 , and τ compared to the MCMC, where the parameters are moderately to poorly resolved. For $C < 0.2$, the linearized approach overestimates the uncertainty of C and m_0 .

The contradictions between the uncertainty analyses from the MCMC inversion and from the linearized approach are discussed in Section 6.3.

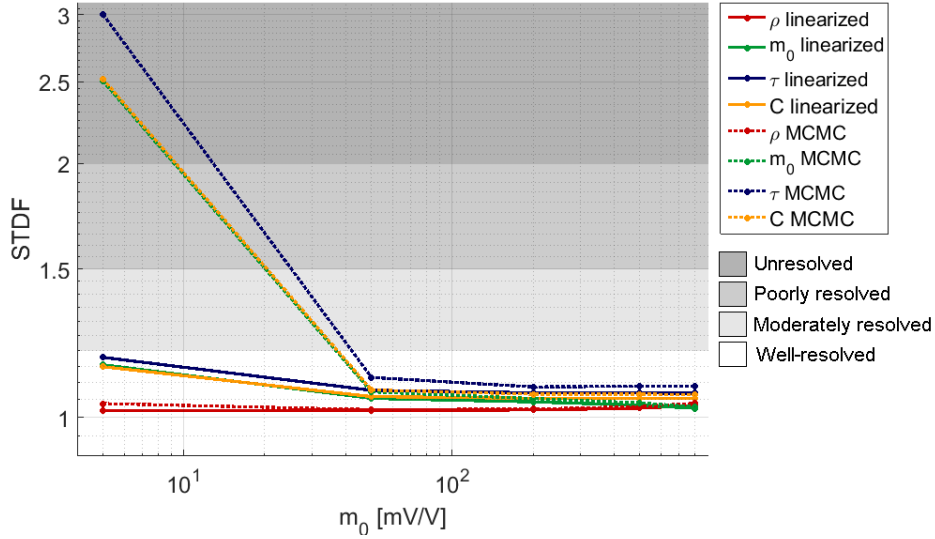


Figure 5.7: Standard deviation factor (STDF) as a function of the chargeability, m_0 . m_0 is varied from 5-800 mV/V, while the remaining Cole-Cole parameters are kept constant: $\rho = 100 \Omega m$, $\tau = 1$ s and $C = 0.6$. The STDFs are computed from the results of a linearized inversion (solid line) and a MCMC inversion (dashed line). NB: If the STDF is above 3, it is put to 3.

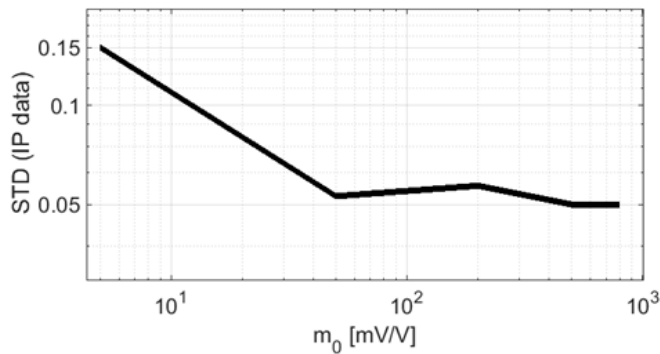


Figure 5.8: Standard deviations (STDs) on IP data for five different Cole-Cole models with different chargeability, m_0 , values. The STDs are computed as the average STD of all data points along the respective IP decay.

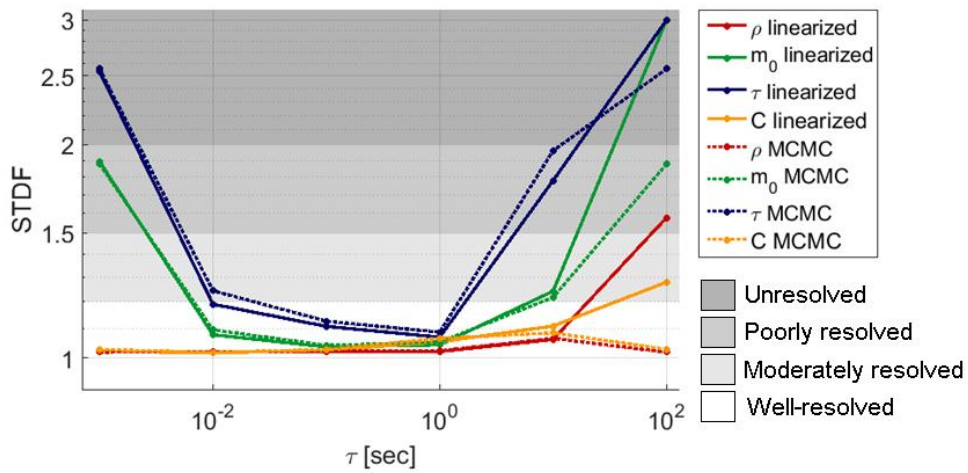


Figure 5.9: Standard deviation factor (STDF) as a function of the time constant, τ . τ is varied between 0.001-100 s, while the remaining Cole-Cole parameters are kept constant: $\rho = 100 \Omega\text{m}$, $m_0 = 200 \text{ mV/V}$ and $C = 0.6$. The STDFs are computed from the results of a linearized inversion (solid line) and the MCMC inversion (dashed line). NB: If the STDF is above 3, it is put to 3.

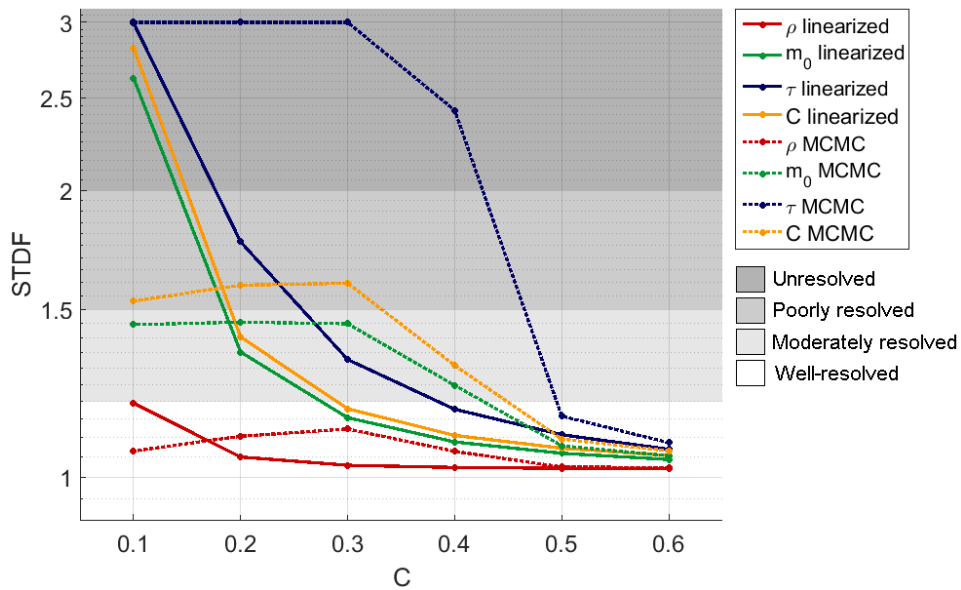


Figure 5.10: Standard deviation factor (STDF) as a function of the frequency exponent, C . C is varied between 0.1-0.6, while the remaining Cole-Cole parameters are kept constant: $\rho = 100 \Omega\text{m}$, $m_0 = 200 \text{ mV/V}$ and $\tau = 1 \text{ s}$. The STDFs are computed from the results of a linearized inversion (solid line) and the MCMC inversion (dashed line). NB: If the STDF value is above 3, it is put to 3.

5.3 Models from Ghorbani *et al.* (2007)

The four Cole-Cole models, previously used by Ghorbani *et al.* (2007), were inverted with 500,000 iterations to ensure convergence of the less resolved models. 29-31% of the proposed models were accepted, when the steps length constants were in the range 0.5-0.9.

All the inversion results are presented in Appendix A.4 together with the synthetic forward responses. The appendix also includes the results from Ghorbani. Here, the results from Model 1 are shown as an example.

STDFs are computed on the MCMC inversion results from this study. The results are shown in Table 5.1. All parameters, except τ in Model 1 and Model 3, are resolved with $STDF < 2$.

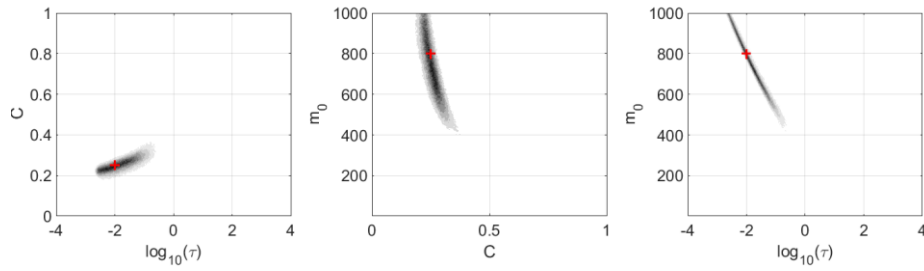
Figure 5.11a shows the posterior probability distributions from the MCMC inversion of Model 1. The distributions are presented with a logarithmic transform of τ to make them comparable with the results from Ghorbani. Clear and simple correlations are seen between the IP parameters. The correlations are slightly nonlinear, however, if the logarithm was used on all parameters, it would impose linearity. Each plot has only one maximum, which is close to the true model indicated by the red cross. The distributions of τ and C are limited by the upper boundary of m_0 . This can also be seen in Figure 5.12, where the marginal distributions of the IP parameters are plotted as histograms. The distribution of τ is steep to the left due to the correlation with m_0 .

The results from Ghorbani (Figure 5.11b) have more complex posterior distributions with two maxima seen on the m_0 - τ cross-plot. This is also the case for Model 2, 3 and 4 (Appendix A.4).

	$STDF(\rho)$	$STDF(m_0)$	$STDF(\tau)$	$STDF(C)$
Model 1	1.02	1.29	3.77	1.18
Model 2	1.22	1.9	1.86	1.03
Model 3	1.01	1.40	7.32	1.25
Model 4	1.02	1.22	1.49	1.11

Table 5.1: Standard deviation factors (STDF) of the MCMC estimated Cole-Cole parameters for Model 1 to Model 4 (Table 4.1). All parameters with $STDF < 2$ are said to be resolved.

a) Results from MCMC inversion:



b) Results from Ghorbani *et al.* (2007):

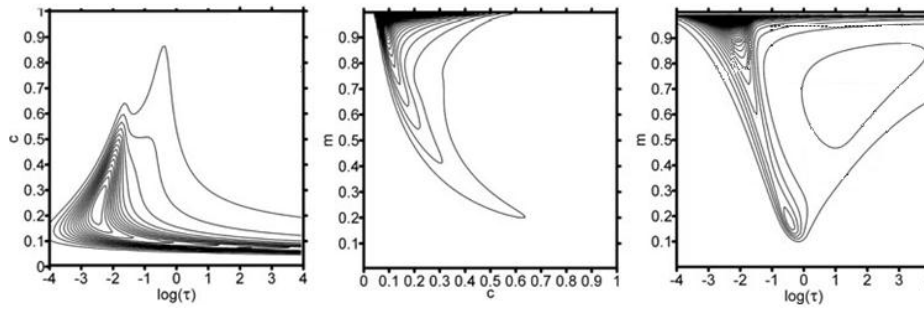


Figure 5.11: a) MCMC inversion results of Model 1: $\rho = 100 \Omega\text{m}$, $m_0 = 800 \text{ mV/V}$, $\tau = 0.01 \text{ s}$, and $C = 0.25$. b) Results of the same model and same settings produced by Ghorbani *et al.* (2007). Both results are shown with $\log_{10}(\tau)$.

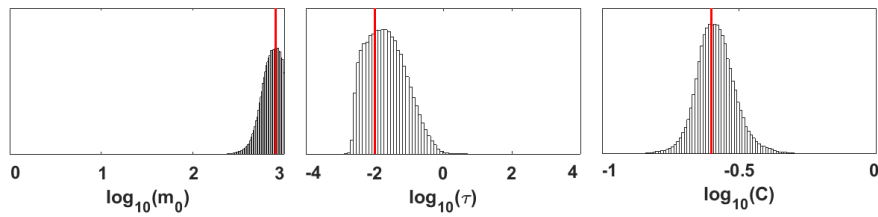


Figure 5.12: Marginal posterior probability distributions of Model 1. The distributions are bell-shaped and have one maximum close to the true model value (red line).

5.4 Acquisition range

Synthetic datasets were generated from the same model but with five different acquisition ranges. The IP decays are shown in Figure 5.13. 500,000 iterations were used for the MCMC inversion of the model and 24-27% of the proposed models were accepted and added to the posterior probability distributions when the step length constant was 0.2-1.05.

The MCMC inversion results are shown in Figure 5.14 - Figure 5.18. The plots have the same scaling for all acquisition ranges, so the span of the distributions can be compared. Zooms of the plots are shown in Appendix A.5.

The results show that the longer the acquisition range is, the better defined are the Cole-Cole parameters. For the acquisition ranges below three decades (Figure 5.14-Figure 5.16), the distributions of m_0 and τ do not have a clear maximum and the true model is located on the flank of the distributions.

The results from the two decade acquisition range (Figure 5.16) have a skewness in the distribution of m_0 and τ . Furthermore, the cross-plots between m_0 and C and between τ and C are curved. This means that the correlation between the parameters is nonlinear.

For acquisition ranges above three decades (Figure 5.17 - Figure 5.18), the distributions are all bell-shaped with a single clear maximum. The nonlinearity of the parameter correlations are gone (see zoom of cross-plots in Appendix A.5).

The STDFs of the five results are plotted in Figure 5.19. The figure sums up the results. When a small acquisition range of two decades or less is used, m_0 and τ cannot be resolved. The longer acquisition range, the better resolved are the parameters.

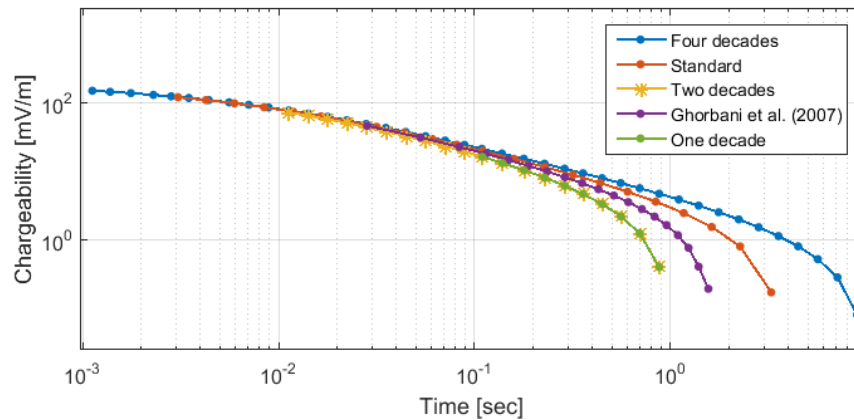


Figure 5.13: IP decays for a homogenous half-space with the Cole-Cole parameters: $\rho = 100 \Omega\text{m}$, $m_0 = 200 \text{ mV/V}$, $\tau = 0.01 \text{ s}$, and $C = 0.6$. The synthetic decays are generated using five different acquisition ranges indicated by the colors. A noise model is added to all the datasets (Section 3.2.3).

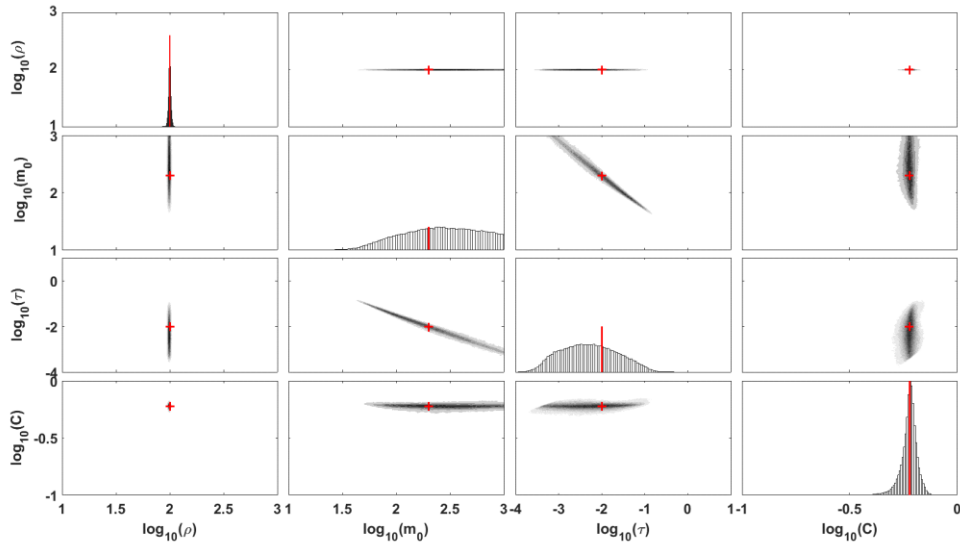


Figure 5.14: MCMC inversion results for a one decade (100-1000 ms) acquisition range (Table 4.3). The true model has the parameters: $\rho = 100 \Omega\text{m}$, $m_0 = 200 \text{ mV/V}$, $\tau = 0.01 \text{ s}$, and $C = 0.6$. The diagonal shows marginal distributions of the Cole-Cole parameters and the off-diagonal shows the cross-correlations. The true model parameters are indicated in red.

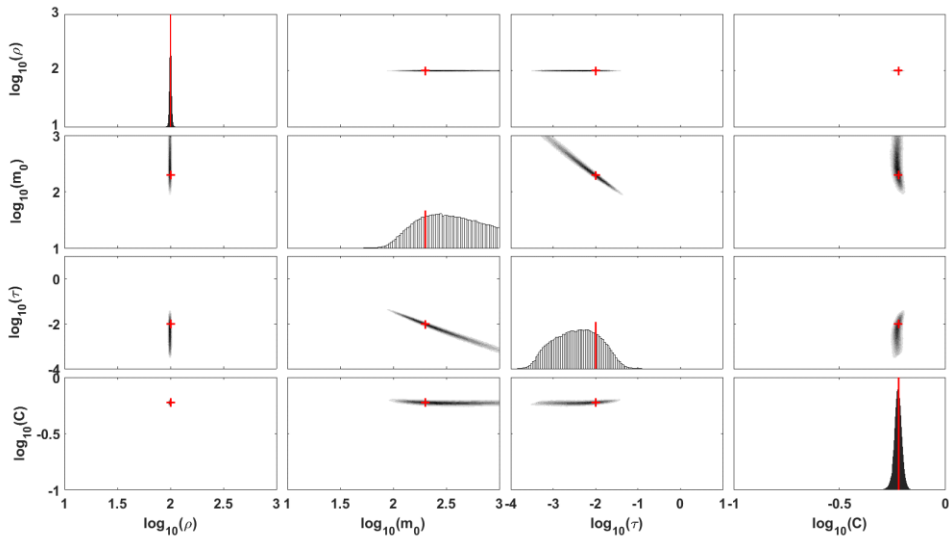


Figure 5.15: MCMC inversion results for acquisition range (20-2000 ms) as used by Ghorbani *et al.* (2007). The true model has the parameters: $\rho = 100 \Omega\text{m}$, $m_0 = 200 \text{ mV/V}$, $\tau = 0.01 \text{ s}$, and $C = 0.6$. The diagonal shows distributions of the Cole-Cole parameters and the off-diagonal shows the correlation. The true model parameters are indicated in red.

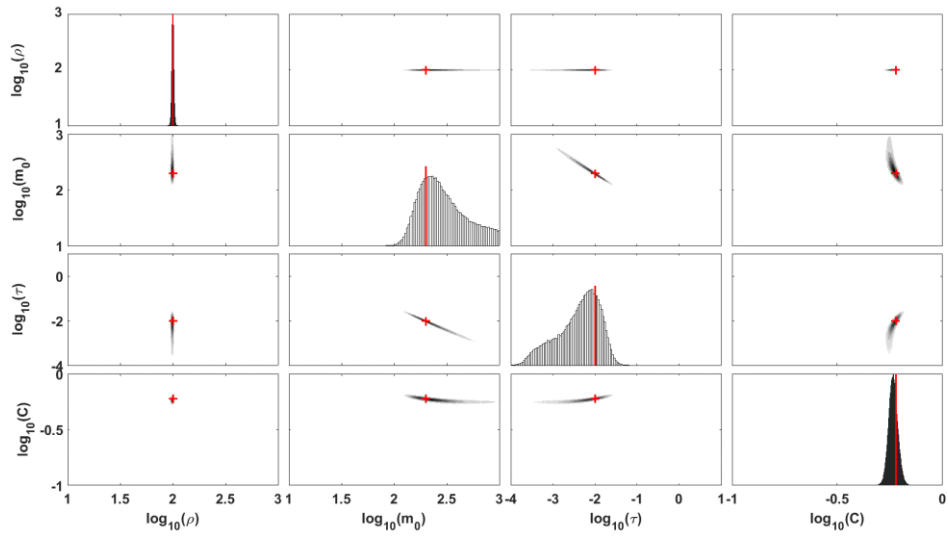


Figure 5.16: MCMC inversion results for a two decade (10-1000 ms) acquisition range. The true model has the parameters: $\rho = 100 \Omega\text{m}$, $m_0 = 200 \text{ mV/V}$, $\tau = 0.01 \text{ s}$, and $C = 0.6$. The diagonal shows distributions of the Cole-Cole parameters and the off-diagonal shows the correlation. The true model parameters are indicated in red.

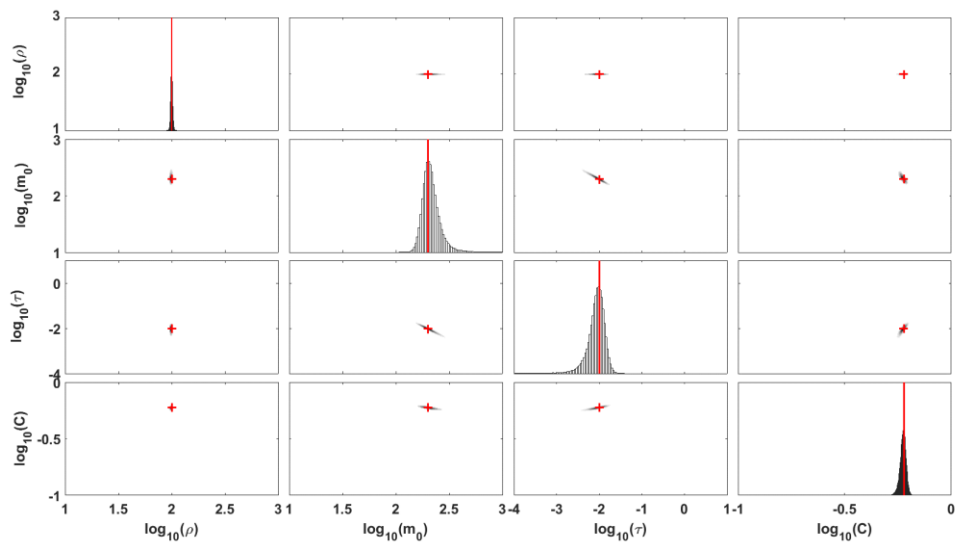


Figure 5.17: MCMC inversion results for the standard acquisition range (2.59-4000 ms). The true model has the parameters: $\rho = 100 \Omega\text{m}$, $m_0 = 200 \text{ mV/V}$, $\tau = 0.01 \text{ s}$, and $C = 0.6$. The diagonal shows distributions of the Cole-Cole parameters and the off-diagonal shows the correlation. The true model parameters are indicated in red. Zoomed views of the subplots can be found in Appendix A.5.

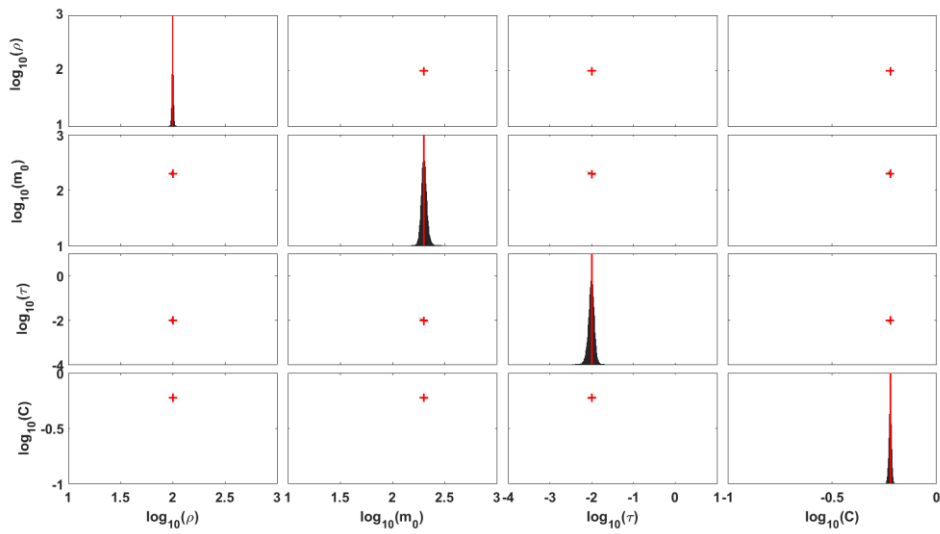


Figure 5.18: MCMC inversion results for a four decade (1-10.000 ms) acquisition range. The true model has the parameters: $\rho = 100 \Omega$, $m_0 = 200 \text{ mV/V}$, $\tau = 0.01 \text{ s}$, and $C = 0.6$. The diagonal shows distributions of the Cole-Cole parameters and the off-diagonal shows the correlation. The true model parameters are indicated in red. Zoomed views of the subplots can be found in Appendix A.5.

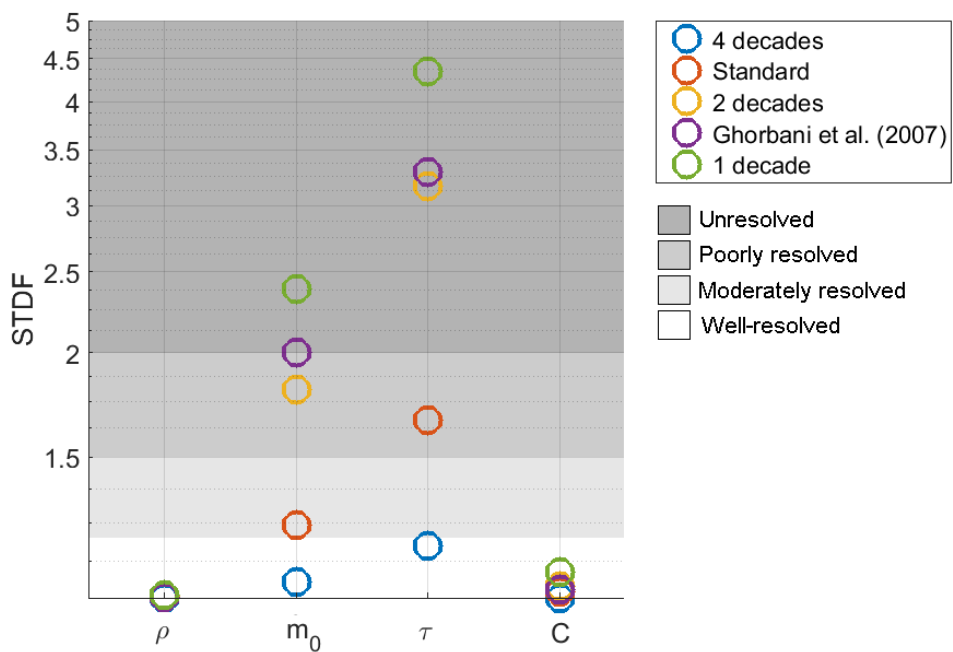


Figure 5.19: Standard deviation factors (STDFs) of the four Cole-Cole parameters computed from MCMC inversion of a model with five different acquisition ranges (indicated by the colors). The figure shows that the acquisition range must be more than two decades to resolve the IP parameters.

5.5 Layered models

5.5.1 Three-layer model

Synthetic data sets were generated on Model A, B and C (described in Table 4.4). The synthetic forward response of Model A is shown in Figure 5.20. The three datasets were inverted with 500,000 iterations and step length constants of 0.75, 0.6, and 0.63, respectively. This gave acceptance rates of 21%-23%.

Model A

The MCMC inversion result of Model A with a standard gate setting is presented in Figure 5.21 as the posterior probability density for all three layers. The densities show every 10th accepted model as a transparent line. The more detailed marginal distributions and cross-plots of the model parameters can be found in Appendix A.6.

Figure 5.21 shows a decreasing resolution of the Cole-Cole parameters with increasing depth. In the first two layers, where the corresponding IP decays have tight error bars (Figure 5.20), all the Cole-Cole parameters are resolved according to the STDFs listed in Table 5.2. The thickness, ρ , and m_o are well-resolved and τ is moderately resolved. The value of C is best resolved in the second layer, which can be an effect of the m_o that give raise to a high signal-to-noise ratio.

In the third layer only ρ is resolved. The distribution of τ_3 has a large spread, but the maximum of the distribution is still located at the true model. This is not the case for $m_{o,3}$ and C_3 . Here, the distribution maxima lie far from the true model values. These maxima may illustrate a fit to IP decays with large error bars with penetration depth below 14 m.

Model B

The study of Model A was repeated with Model B, where the C value of all layers were lowered from $C = 0.6$ to $C = 0.3$. The results (shown in Appendix A.6) are similar to the results of Model A. The resolution of ρ is unchanged and the IP parameters of the third layer are still unresolved. The STDFs of the IP parameters have increased with 23-35% in layer one, where $m_o = 50$ mV/V, and with 1-22% in layer two, where $m_o = 300$ mV/V.

Model C

The inversion of Model A was also repeated with Model C, where the acquisition range was decreased to two decades. The results (shown in Appendix A.6) show the same tendencies as for Model A: The IP parameters are resolved in layer one and two and unresolved in layer three. The STDFs of the resolved parameters are increased with 1-32% compared to the results of Model A.

Parameter correlation

Pearson's correlation coefficients were computed for all combinations of the Cole-Cole parameters based on their posterior probability distributions. The coefficients are shown in the lower triangular matrix in Figure 5.22. Here, a positive correlation is indicated with a red color and a negative correlation with a blue color. In the bottom row, the correlation to the data residual, R_{data} , is shown.

The matrix shows a strong C - m_0 anti-correlation in all three layers. In layer one, $m_{o,1}$ is negatively correlated to τ_1 and τ_1 is positively correlated to C_1 . In layer two, ρ_2 is strongly correlation to τ_2 and $m_{o,2}$. $m_{o,2}$ is also strongly negatively correlated to the thickness of layer one and has a strong positive correlation to the thickness of layer two.

The data residual is mildly correlated to the unresolved Cole-Cole parameters of the third layer. The matrix shows that the residual increases as ρ_3 or $m_{o,3}$ increases and as C_3 decreases.

The correlation matrixes of Model B and Model C (Appendix A.6) show the same tendencies as for Model A.

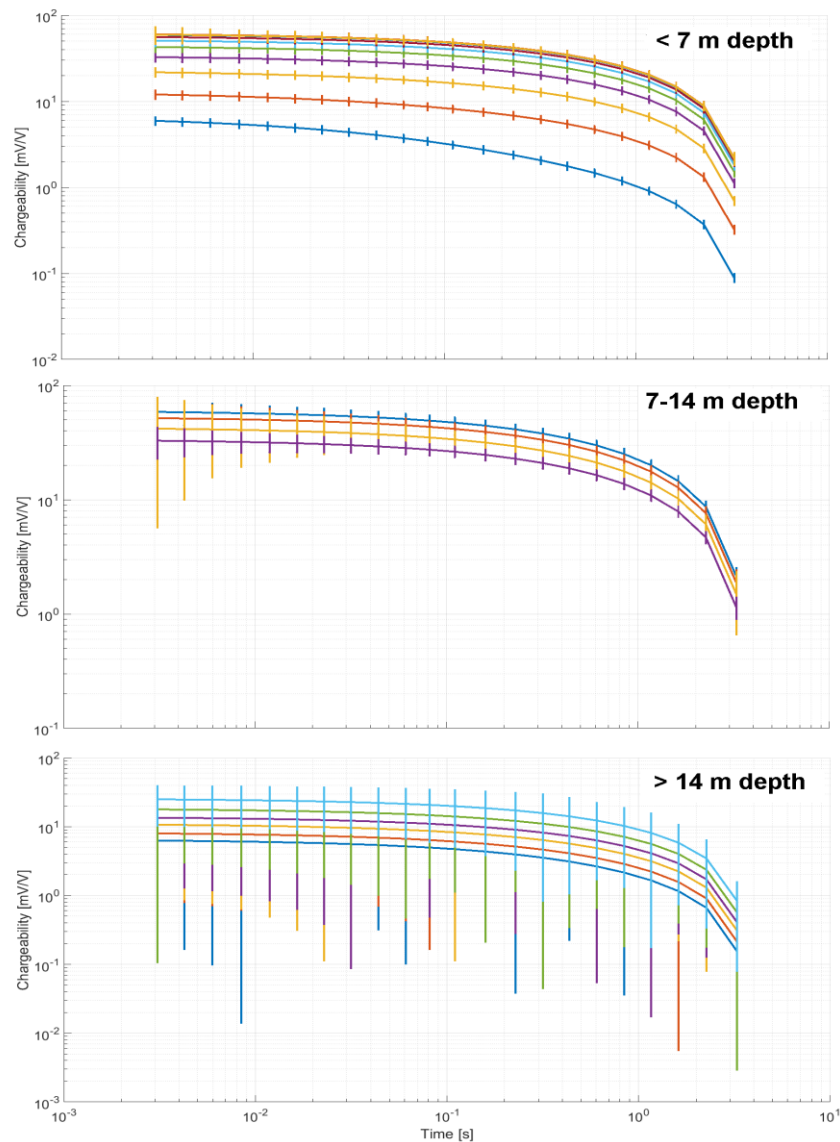


Figure 5.20: Synthetic IP decays with error bars generated from Model A (Table 4.4). The decays are plotted in three subplots according to the depth of their main focus point in the subsurface. The decays are generated with 10% standard deviation on the chargeability and a 0.1 mV voltage threshold.

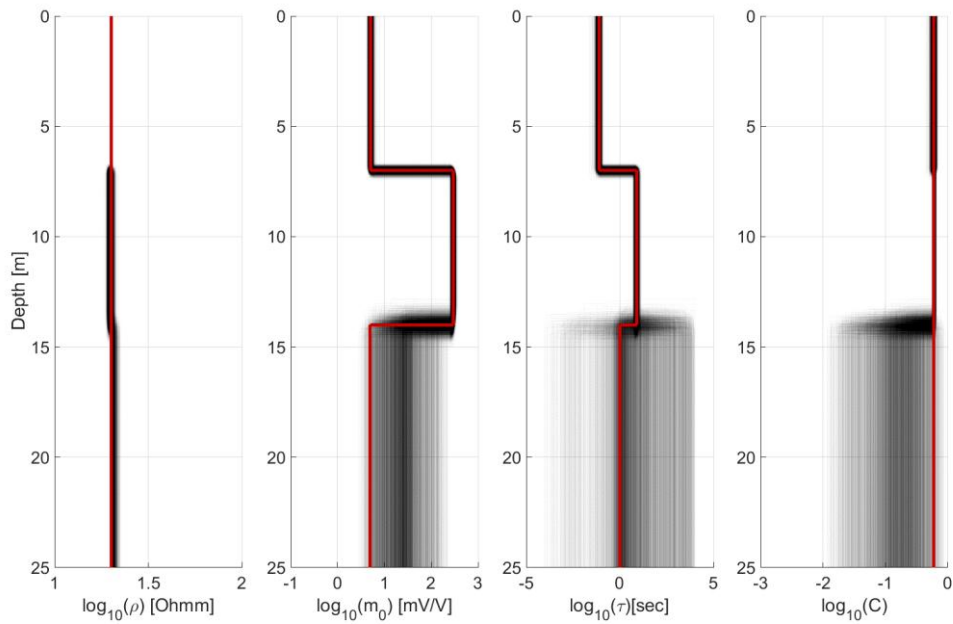


Figure 5.21: MCMC inversion result of Model A (Table 4.4) using a standard acquisition range (2.59 - 4000 ms). The red lines are the true model values and the black lines are models accepted to the posterior probability distribution of the Cole-Cole parameters. The tone represents the model density.

	$STDF(\rho)$	$STDF(m_0)$	$STDF(\tau)$	$STDF(C)$	$STDF(thk)$
Layer 1	1.01	1.07	1.20	1.06	1.02
Layer 2	1.02	1.06	1.17	1.03	1.06
Layer 3	1.02	2.28	23.15	2.34	

Table 5.2: Standard deviation factors (STDFs) computed for Model A (Table 4.4) for a standard acquisition range (2.59-4000 ms).

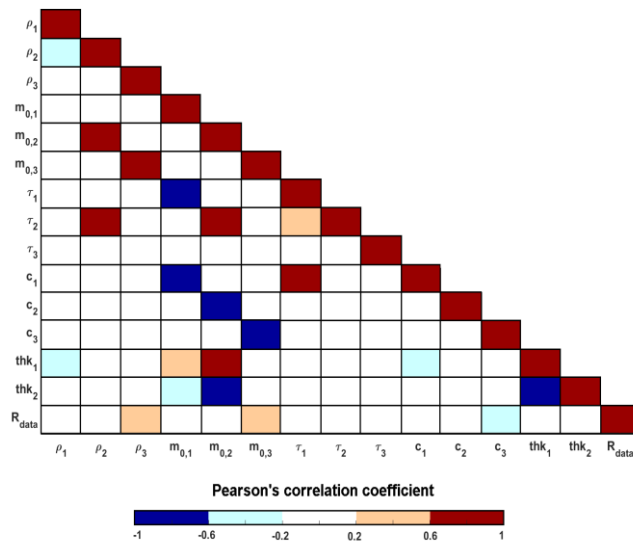


Figure 5.22: Correlation matrix for Model A (Table 4.4). The matrix holds Pearson's correlation coefficients for all correlations between the Cole-Cole parameters. Blue colors indicate an anti-correlation and red colors a positive correlation.

5.5.2 Five-layer model

A synthetic dataset was generated on Model D (described in Table 4.5). The dataset was inverted with 500,000 iterations and step length constant of 0.001. This gave an acceptance rate of 20%. Figure 5.23 shows the posterior possibility distributions of the Cole-Cole parameters, Figure 5.24 shows the IP decays from the forward modeling, Table 5.3 shows the STDFs computed for each Cole-Cole parameter, and Figure 5.25 shows the correlation matrix for the MCMC inversion results.

The resolution of the layer thicknesses decreases with depth and becomes unresolved for layer four (Table 5.3). Thk_2 has STDF = 1.21, which is a moderate resolution, but the density maximum of the layer boundary is shifted upwards compared to the true value (Figure 5.23). This means that the MCMC inversion fails to find the true model.

Layer four is completely unresolved. However, the MCMC finds that the resistivity is high relative to the surrounding layers and that the chargeability is low, which corresponds to the true model. The bottom layer is well-resolved for all parameters.

The correlation matrix in Figure 5.25 shows a C - m_0 anti-correlation in all layers. In layer one, three and five, m_0 is anti-correlated to τ and τ is positive correlated to C . The thicknesses are strongly correlated to ρ in all layers. In layers with low resistivity, this correlation is positive and in layers with high resistivity the correlation is negative. The matrix also shows more complex correlations between the layers. This is both correlations within the same parameters, e.g. $m_{0,1}$ - $m_{0,3}$, and between parameters, e.g. $m_{0,1}$ - τ_3 .

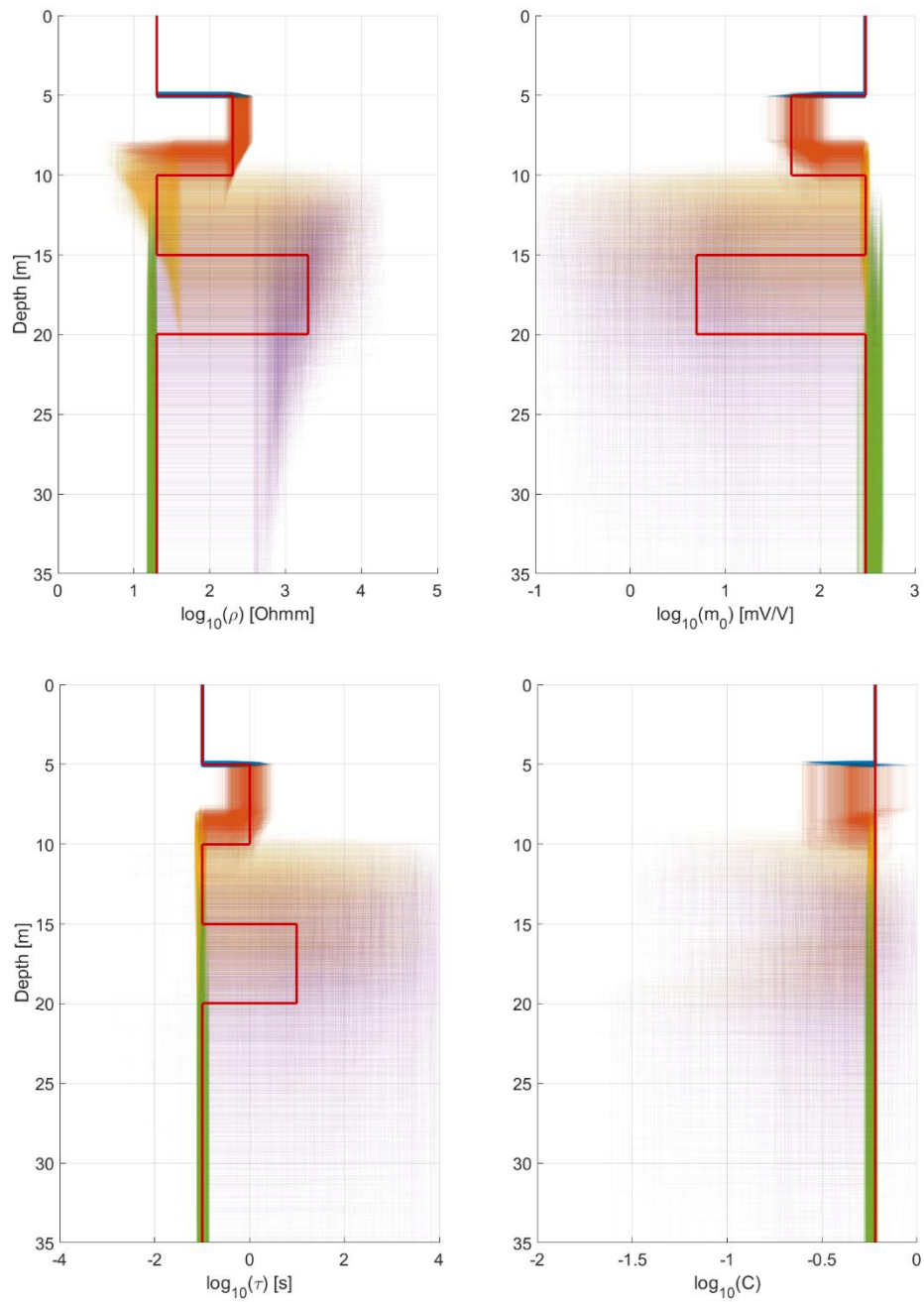


Figure 5.23: MCMC inversion result of the five-layer model, Model D (Table 4.5), using a standard acquisition range (2.59-4000 ms). The red lines are the true model values and the colored areas show the posterior probability density of the Cole-Cole parameters. Each layer is shown in a different color.

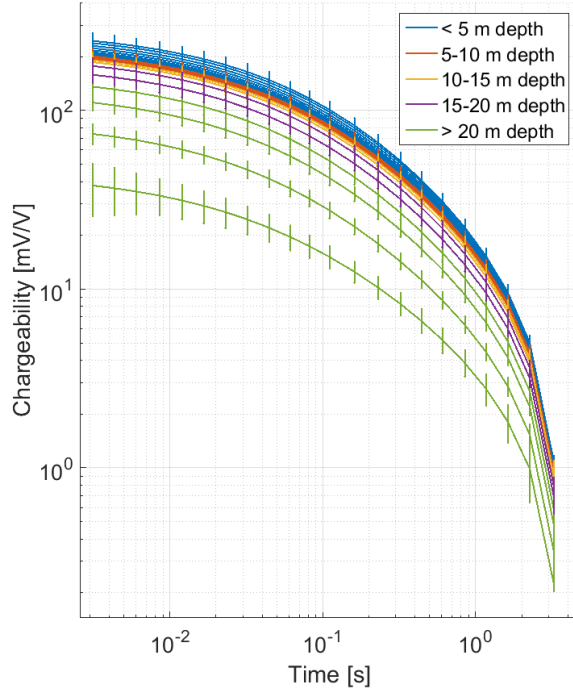


Figure 5.24: Synthetic IP decays for Model D (Table 4.5). The colors show the main focus depths for the IP measurements. The decays are generated with 10% standard deviation on the chargeability and a 0.1 mV voltage threshold.

	$STDF(\rho)$	$STDF(m_0)$	$STDF(\tau)$	$STDF(C)$	$STDF(thk)$
Layer 1	1.01	1.02	1.04	1.01	1.03
Layer 2	1.19	1.33	1.69	1.27	1.21
Layer 3	1.70	1.06	1.17	1.03	1.71
Layer 4	2.55	4.37	15.96	2.22	2.54
Layer 5	1.08	1.15	1.16	1.04	

Table 5.3: Standard deviation factors (STDFs) for MCMC inversion results of the five-layer model, Model D, described in Table 4.5.

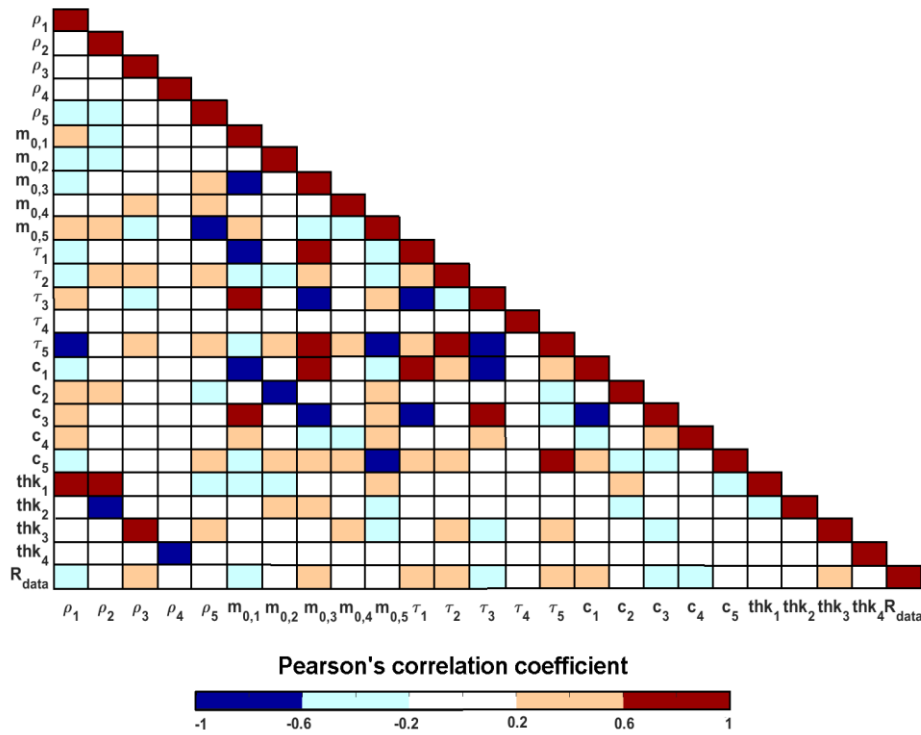


Figure 5.25: Correlation matrix for Model D (Table 4.5). The matrix holds the correlation coefficients between all the Cole-Cole parameters. Blue colors indicate an anti-correlation and red colors a positive correlation.

5.6 Resistivity equivalence

The synthetic DC and DCIP data generated from Model E (Table 4.6) and Model F (Table 4.7) were inverted with 500,000 iterations. 18-32% of the proposed models were accepted and added to the posterior probability distributions when the step length constants were 0.4-0.5.

The MCMC inversion of the DC data alone were approximately 150 times faster than the inversion of the combined DCIP data.

5.6.1 High resistivity equivalence

The MCMC inversion result of the DC and DCIP data from Model E are shown in Figure 5.26 and Figure 5.27, respectively. The model shown has $\rho = [20, 200, 20] \Omega\text{m}$ and the thickness of the middle layer is one half of the layer above.

The DC method finds the resistivity of the top and bottom layer, but ρ_2 and thk_2 are completely unresolved (Figure 5.26). The resistance ($thk \cdot \rho$), however, is well-resolved with a STDF = 1.03. This indicates a classic high resistivity equivalence. The correlation matrix (Figure 5.28) also shows a negative correlation between the parameters meaning that if the resistivity is increased the thickness will decrease to keep the resistance response constant.

Opposite to the DC method, the DCIP method resolves ρ_2 and thk_2 well, even though the parameters are strongly correlated (Figure 5.27 and Figure 5.29). This means that the information from the IP signal resolves the high resistivity equivalence.

Different thicknesses

The thickness of the middle layer in Model E was varied to study the equivalence. Figure 5.30 shows the STDFs of the resistivities and the thicknesses for the sweep of models. The STDFs are shown for both the DC and the DCIP inversions. The DCIP method resolves the middle layer down to a thickness of 5 meters. When the thickness gets below 5 meters, ρ_2 and thk_2 become unresolved. The DC method, on the other hand, only resolves the middle layer when thk_2 is above 30 m. This means that the middle layer must be three times the thickness of the overlying material to be resolved by the DC method.

Different chargeabilities

In Model E, the chargeability contrast between the middle layer and the layer below and above is high. This is expected to help resolve the equivalence in Figure 5.26, because the thicknesses are more easily determined. To test this, different values of $m_{0,2}$ were used and the STDFs of ρ_2 and thk_2 were computed. The results, shown in Figure 5.31, show that as the contrast in m_0 between the layers is decreased, the resolution of ρ_2 and thk_2 decreases as well. When the contrast in m_0 is removed entirely, ρ_2 and thk_2 become completely unresolved.

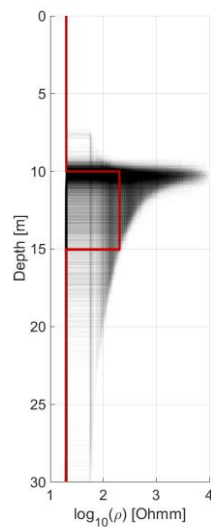


Figure 5.26: MCMC inversion results of DC data generated from a three-layer model, Model E, described in Table 4.6. Here, $\rho = [20, 200, 20] \Omega\text{m}$. The red line is the true model value and the black is the posterior probability density from the MCMC inversion result. The figure shows a high resistivity equivalence, where the high resistivity of the middle layer is unresolved together with the thickness.

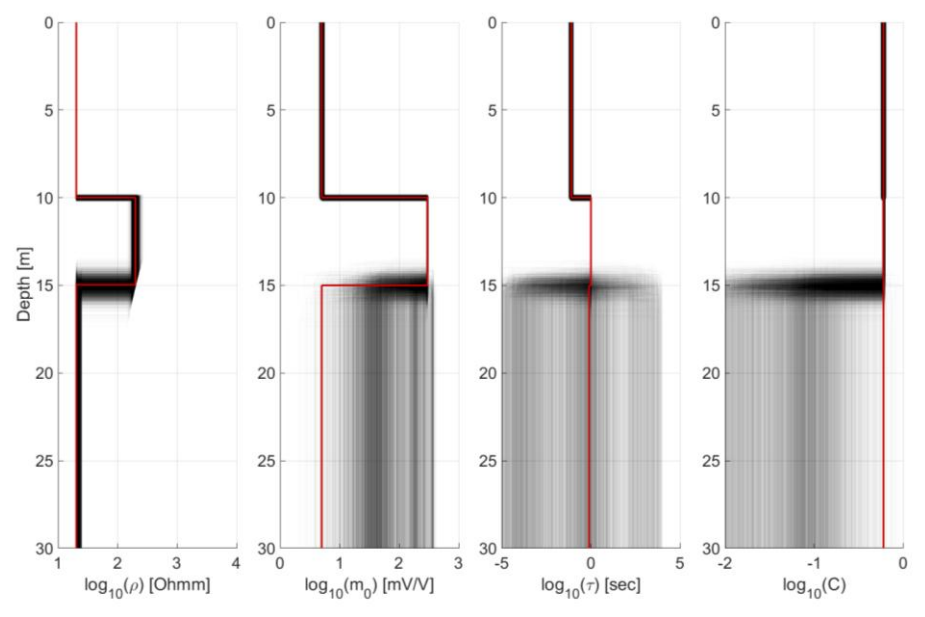


Figure 5.27: MCMC inversion results of DCIP data generated from the three-layer model, Model E, described in Table 4.6. The red line is the true model values and the black is the posterior probability density from the MCMC inversion.

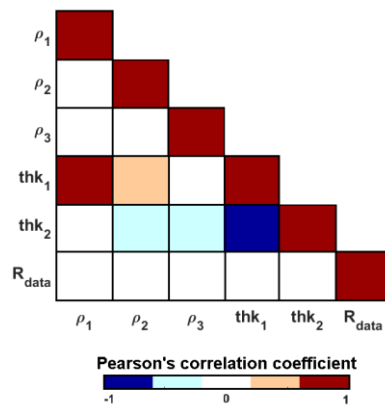


Figure 5.28: Correlation matrix for DC inversion of a high resistivity equivalence model, Model E, described in Table 4.6. The matrix holds the correlation coefficients between all the Cole-Cole parameters. Blue colors indicate an anti-correlation and red colors a positive correlation.

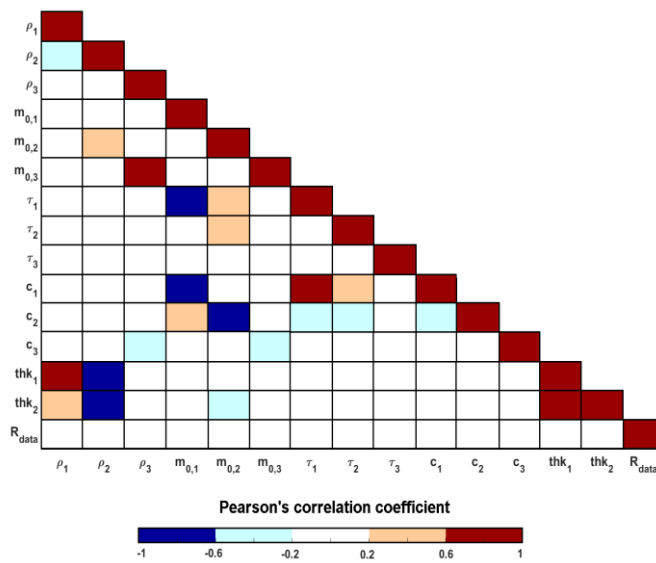


Figure 5.29: Correlation matrix for DCIP inversion of a high resistivity equivalence model, Model E, described in Table 4.6. The matrix holds the correlation coefficients between all the Cole-Cole parameters. Blue colors indicate an anti-correlation and red colors a positive correlation.

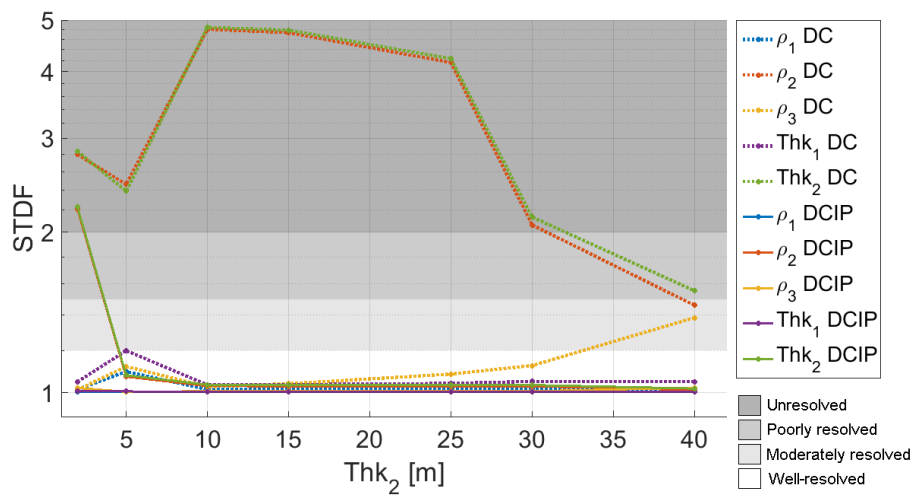


Figure 5.30: Uncertainty analysis of a three-layer model, Model E (Table 4.6), with high resistivity equivalences for a DC inversion (dashed lines) and a DCIP inversion (solid lines). The uncertainties are given as standard deviation factors (STDFs). The plot shows that the DCIP method resolves ρ_2 and thk_2 when the thickness of the middle is half the thickness of the layer above or thicker, but that the DC method needs the thickness to be three times the thickness of the layer above to resolve the equivalence.

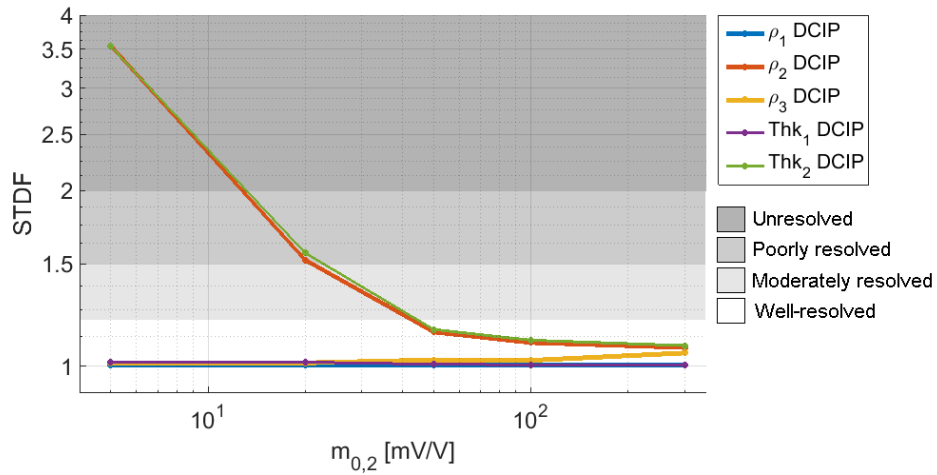


Figure 5.31: Uncertainty analysis of a three-layer model, Model E (Table 4.6), with high resistivity equivalences. The uncertainties are given as standard deviation factors (STDFs). The plot shows that the DCIP method resolves ρ_2 and thk_2 down to approximately a factor three in contrast, i.e. $m_0 = [5, 15, 5]$ mV/V.

5.6.2 Low resistivity equivalence

The study of equivalent models was also carried out for a low resistivity example with Model F (Table 4.7). The results of the DC and the DCIP inversion are shown in Figure 5.32 and Figure 5.33.

The inversion of the DC data does not resolve ρ_2 and thk_2 , which have STDFs > 2 (Figure 5.32). However, the conductance (thk_2/ρ_2) is well-resolved with STDF = 1.04. Figure 5.34 shows that the two parameters have a strong positive correlation, which is opposite the previous model with a high resistivity equivalence. When the IP data are added to the inversion, the parameters become well-resolved with STDFs < 1.2 .

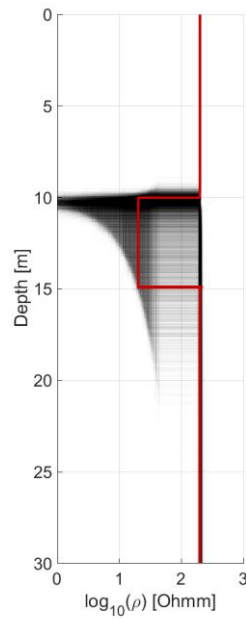


Figure 5.32: MCMC inversion results of DC data generated from a three-layer model (Model F described in Table 4.7). The red line is the true model and the black is the model density from the MCMC inversion. The figure shows a low resistivity equivalence, where the low resistivity middle layer is unresolved.

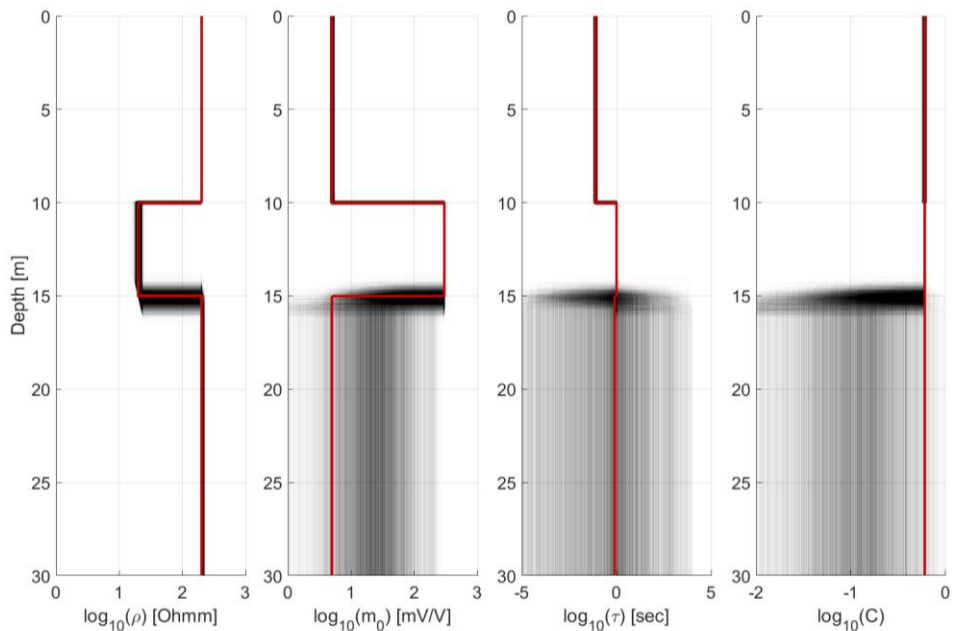


Figure 5.33: MCMC inversion results of DCIP data generated from a three-layer model (Model F described in Table 4.7). The red line is the true model and the black is the posterior probability density from the MCMC inversion.

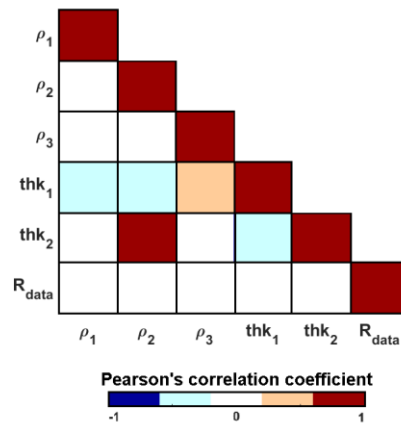


Figure 5.34: Correlation matrix for DC inversion of a low resistivity equivalence model (Model F described in Table 4.7). The matrix holds the correlation coefficients between all the Cole-Cole parameters. Blue colors indicate an anti-correlation and red colors a positive correlation.

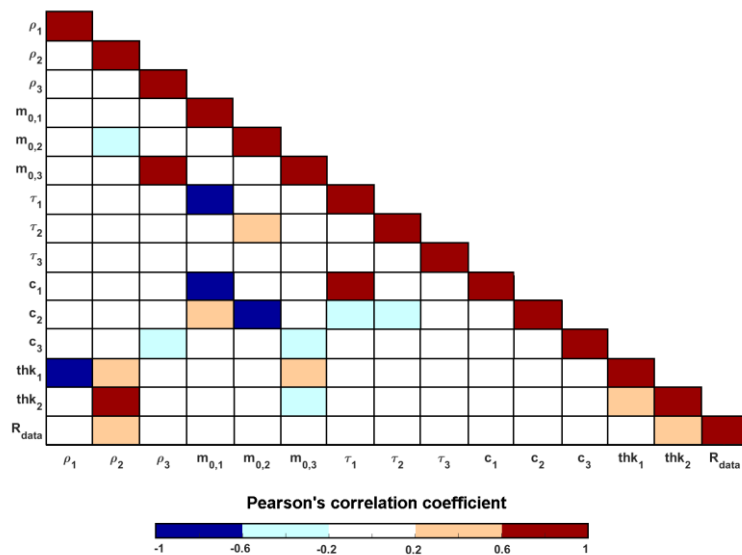


Figure 5.35: Correlation matrix for DCIP inversion of a low resistivity equivalence model (Model F described in Table 4.7). The matrix holds the correlation coefficients between all the Cole-Cole parameters. Blue colors indicate an anti-correlation and red colors a positive correlation.

5.7 Information from IP

A three-layer model with constant IP parameter ($m_0 = 50$ mV/V, $\tau = 1$ s, and $C = 0.6$), but a factor ten contrast in resistivity ($200 \Omega\text{m}$, $2000 \Omega\text{m}$, $200 \Omega\text{m}$) was inverted with DCIP data and with DC data alone. 500,000 iterations were used and 22% of the proposed models were accepted in both cases. The results are shown in Figure 5.36 and Figure 5.37.

The inversion results from the DC data show a high resistivity equivalence, similar to what was presented in Figure 5.26. Also here, the resistivity and the thickness of layer two are unresolved with $\text{STDF}(\rho_2) = 2.25$ and $\text{STDF}(\text{thk}_2) = 2.28$. In Figure 5.37, the IP data are added to the inversion, and ρ_2 and thk_2 are now resolved with $\text{STDF}(\rho_2) = 1.72$ and $\text{STDF}(\text{thk}_2) = 1.70$. This is, however, classified as poorly resolved parameters.

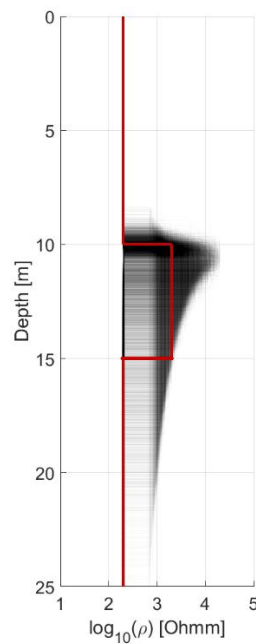


Figure 5.36: MCMC inversion results of DC data generated from the three-layer model: $\rho = [200, 2000, 200] \Omega\text{m}$. The red line is the true model and the black is the model density from the MCMC inversion. The thickness and the resistivity in the middle layer are unresolved with standard deviation factors above two due to high resistivity equivalence.

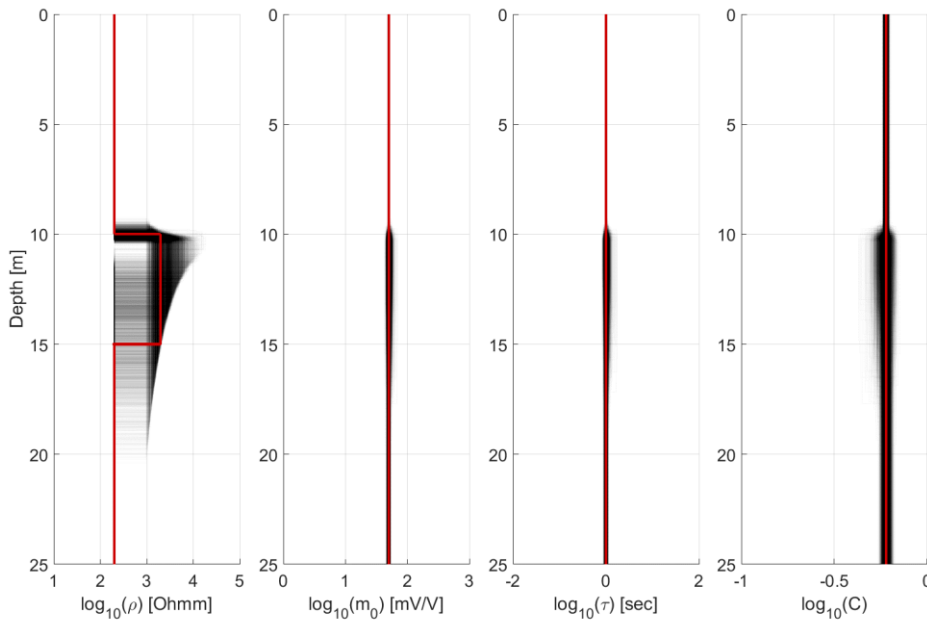


Figure 5.37: MCMC inversion results of DCIP data generated from the three-layer model: $\rho = [200, 2000, 200] \Omega\text{m}$, $m_0 = 50 \text{ mV/V}$, $\tau = 1 \text{ s}$, and $C = 0.6$. The red line is the true model and the black is the posterior probability density from the MCMC inversion.

5.7.1 Chargeability

The chargeability, $m_{0,2}$, of the middle layer in Model G (Table 4.8), was varied between $m_{0,2} = 5\text{-}800 \text{ mV/V}$. MCMC inversions were carried out on all the models with 500,000 iterations. 24-27% of the models were accepted to the posterior probability distribution.

An example of the MCMC inversion results is shown in Figure 5.38, where the contrast in m_0 between layer two and the layers above and below is a factor ten ($m_0 = [50, 500, 50] \text{ mV/V}$). The uncertainty analysis is shown in Figure 5.39.

Figure 5.38 shows that a factor ten contrast in chargeability resolves the thickness of the imbedded layer. Figure 5.39 shows that the resolution of the layer thicknesses decreases as the chargeability contrast is decreased. thk_1 and thk_2 are only unresolved when there is no contrast at all, which means that a factor two contrast in the chargeability is enough to resolve the middle layer. The resolution of $m_{0,2}$ is decreasing as the chargeability itself is decreasing, as has been observed previously.

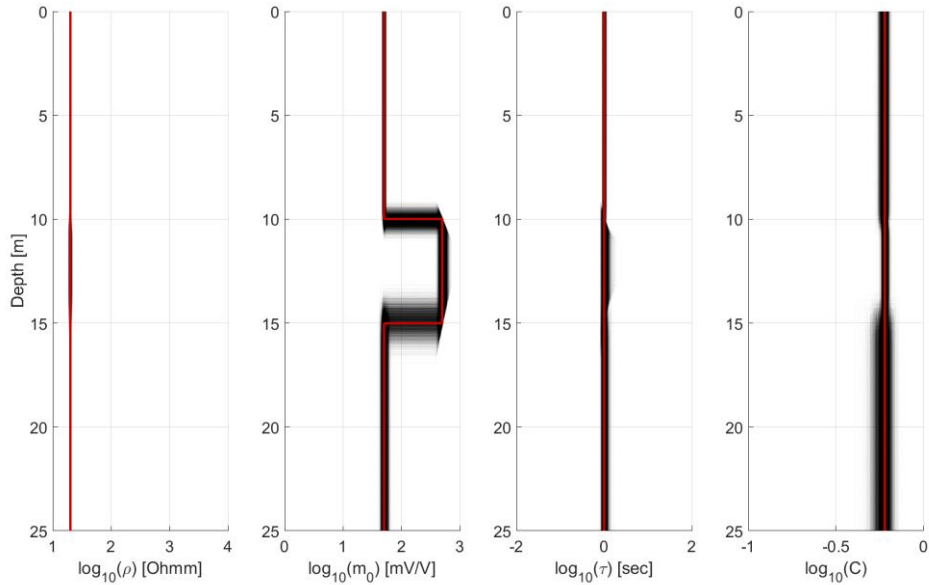


Figure 5.38: MCMC inversion results of a three-layer model with the Cole-Cole parameters: $\rho = 20 \Omega\text{m}$, $m_0 = [50, 500, 50] \text{ mV/V}$, $\tau = 1 \text{ s}$, and $C = 0.6$. The layer thicknesses are well-resolved from the factor ten contrast in the chargeability and have the standard deviation factors: $\text{STDF}(\text{thk}_1) = 1.03$ and $\text{STDF}(\text{thk}_2) = 1.19$. The red lines indicate the true model values and the black lines are the posterior probability density.

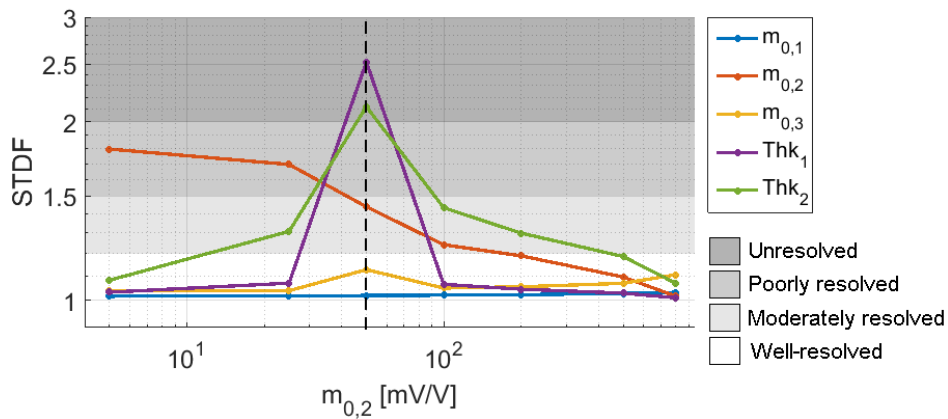


Figure 5.39: Resolution of thicknesses (thk) and chargeabilities (m_0) in a three-layer model ($\rho = 20 \Omega\text{m}$, $m_0 = [50, m_{0,2}, 50] \text{ mV/V}$, $\tau = 1 \text{ s}$, and $C = 0.6$), where $m_{0,2}$ has been varied between 5 and 800 mV/V. The dashed line marks the homogenous model with no contrasts between the layers. The figure shows the standard deviation factors (STDFs) for different contrasts in the chargeability. A factor two contrast in the chargeability is enough to resolve the thicknesses in the model.

5.7.2 Time constant

The time constant, τ_2 , of the middle layer of Model G (Table 4.8) was varied between $\tau_2 = 0.01$ -10 s. MCMC inversions were carried out on all the models with 500,000 iterations. 25-29% of the models were accepted to the posterior probability distribution.

The inversion result of a model with a factor ten contrast in τ is shown in Figure 5.40 and the uncertainty analysis is shown in Figure 5.41.

The results in Figure 5.40 show that a factor ten contrast in τ can resolve thk_2 moderately. However, the value of τ_2 is only poorly resolved, even though the distribution has its maximum at the true model.

The uncertainty analysis in Figure 5.41 shows that the resolution of thk_1 and thk_2 increases and the contrast in τ increases. The resolution of τ_2 itself, however, does not become more than poorly resolved.

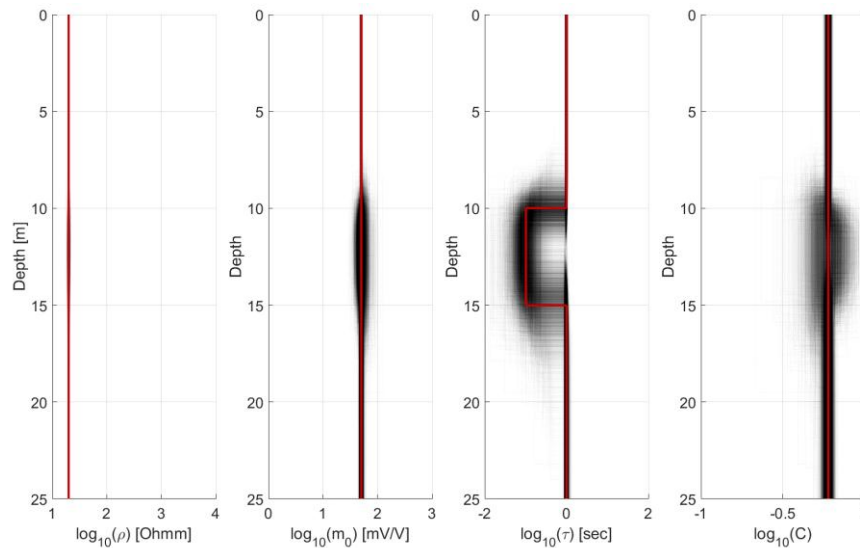


Figure 5.40: MCMC inversion results of a three-layer model with the Cole-Cole parameters: $\rho = 20 \Omega\text{m}$, $m_0 = 50 \text{ mV/V}$, $\tau = [1, 0.1, 1] \text{ s}$, and $C = 0.6$. The layer thicknesses are well to moderately resolved from the factor ten contrast in τ and have the standard deviation factors: $\text{STDF}(thk_1) = 1.09$ and $\text{STDF}(thk_2) = 1.33$. The red lines indicate the true model values and the black lines are posterior probability density.

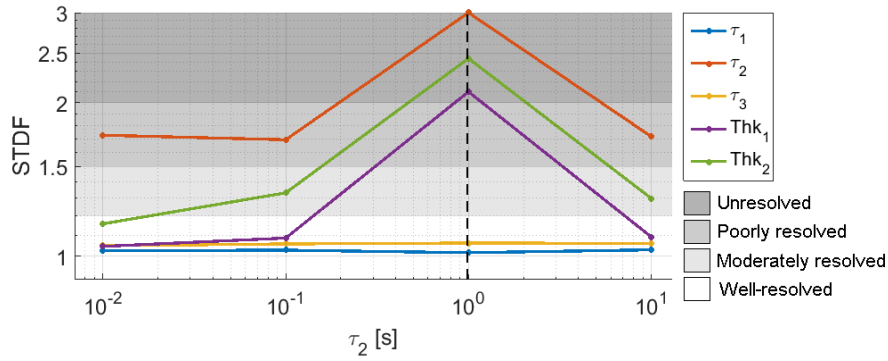


Figure 5.41: Resolution of thicknesses (*thk*) and τ in a three-layer mode: $\rho = 20 \Omega\text{m}$, $m_0 = 50 \text{ mV/V}$, $\tau = [1, \tau_2, 1] \text{ s}$, and $C = 0.6$, where τ_2 has been varied between 0.01 and 10 s. The dashed line marks the homogenous model with no contrasts between the layers. The figure shows the standard deviation factors (STDF) for different contrasts in τ .

5.7.3 Frequency exponent

The frequency exponent of the middle layer, C_2 , in Model G (Table 4.8) was varied between $C_2 = 0.1-0.6$. MCMC inversions were carried out on all the models with 500,000 iterations. 23-24% of the proposed models were accepted to the posterior probability distribution.

It is not possible to investigate a factor ten contrast in C as it was done for the other Cole-Cole parameters, so instead the following contrast was used: $C_1 = 0.6$, $C_2 = 0.1$ and $C_3 = 0.6$. The resulting distributives are shown in Figure 5.42 and an uncertainty analysis is plotted in Figure 5.43 for all values of C .

The results show that the factor six contrast in C resolves the thicknesses very well with $\text{STDF} < 1.2$ (Figure 5.42). The values of the IP parameters are, however, not resolved in the middle layer due to the low value of C .

The uncertainty analysis in Figure 5.43 shows that the resolution of thk_1 and thk_2 increases as the contrast in C increases. The thicknesses can be resolved even when the contrast in C is only a factor 1.2, e.g. $C = [0.6, 0.5, 0.6]$. For $C = 0.5$, C_3 is found to be moderately resolved according to the uncertainty analysis, however, the inversion does not find the true model, why the STDF is misleading. This dilemma is discussed in Chapter 6.

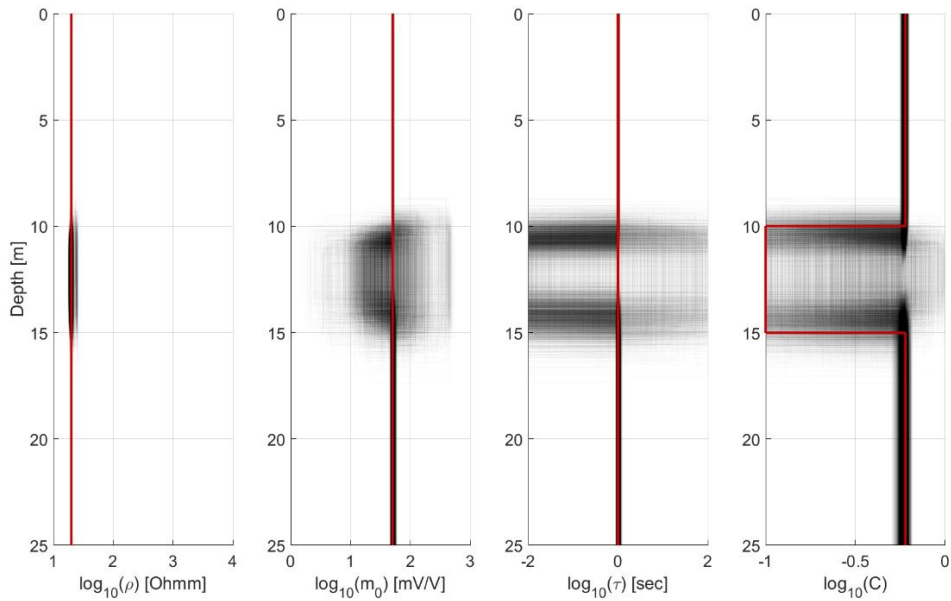


Figure 5.42: MCMC inversion results of a three-layer model with the Cole-Cole parameters: $\rho = 20 \text{ } \Omega\text{m}$, $m_0 = 50 \text{ mV/V}$, $\tau = 0.1 \text{ s}$, and $C = [0.6, 0.1, 0.6]$. The layer thicknesses are well-resolved from the factor six contrast in C and have the standard deviation factors: $\text{STDF}(thk_1) = 1.05$ and $\text{STDF}(thk_2) = 1.19$. The red lines indicate the true model values and the black lines are the posterior probability density.

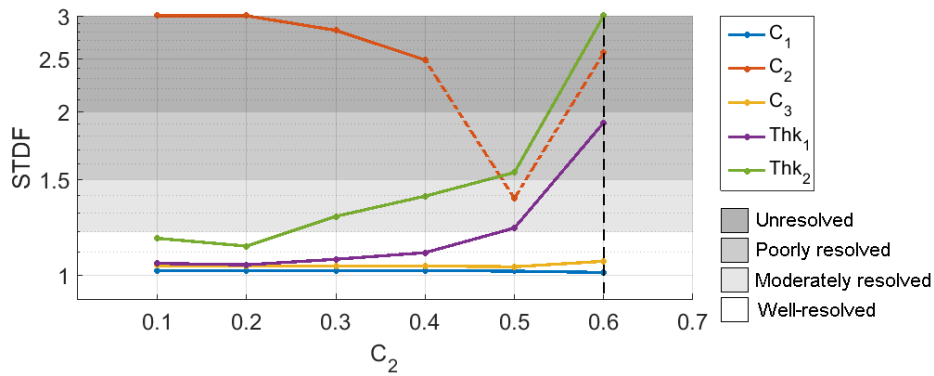


Figure 5.43: Resolution of thicknesses, thk , and C in a three-layer mode: $\rho = 20 \text{ } \Omega\text{m}$, $m_0 = 50 \text{ mV/V}$, $\tau = 1 \text{ s}$, and $C = [0.6 \ C_2 \ 0.6]$, where C_2 has been varied between 0.1 and 0.6. The dashed line marks the homogenous model with no contrasts between the layers. The figure shows the standard deviation factors (STDF) for different contrasts in C .

5.8 Field example

Ten linearized inversions were carried out on the field data with one to ten layers respectively. The smallest data residual was found using four layers, why this was applied for the analysis.

An arbitrary start model was chosen and a linearized inversion was carried out to determine a start model for the MCMC inversion. 1,000,000 iterations were used to ensure convergence of the Markov chain. Every 10th accepted model was plotted to show the posterior probability distribution in Figure 5.44. The plot shows the Cole-Cole parameters with a different color for each layer. The result of the linearized inversion is plotted with a red line. The marginal distributions and cross-plots of the Cole-Cole parameters are presented in more detail in Appendix A.8. The STDFs were computed for the MCMC inversion results and are listed together with the linearized uncertainty analysis in Table 5.4

Layer one

The MCMC inversion results show a very thin layer in the top of the profile (Figure 5.44). The layer has a low ρ . ρ is almost unresolved and has a strong positive correlation to the thickness of the layer (Figure 5.45 and Table 5.4). The distribution of ρ has a maximum at $\sim 10 \Omega\text{m}$ and the thickness at $\sim 0.4 \text{ m}$.

The well-resolved m_o of the layer is $\sim 16 \text{ mV/V}$. τ and C are also well determined to $\sim 1 \text{ s}$ and ~ 0.9 respectively. All the marginal distributions are approximately bell-shaped and the parameter correlations are linear (Appendix A.8).

Layer two

The well-resolved ρ of the second layer is $\sim 46 \Omega\text{m}$ and the layer thickness is $\sim 27 \text{ m}$. There is a strong positive correlation between these two parameters.

m_o and C are also well-resolved, while τ is poorly resolved. The marginal distributions are not as bell-shaped as for the top layer (Appendix A.8). The distributions have spikes on the flanks as if the MCMC has not fully converged. However, each distribution still has a clear maximum at $m_o \sim 40 \text{ mV/V}$, $\tau \sim 0.02 \text{ s}$, and $C \sim 0.5$ respectively. The IP parameters show strong correlations. Anti-correlations are seen between m_o and C and between m_o and τ , and a positive correlation is seen between C and τ .

Layer three

The third layer is very thin (mean value of 3 m) and all the Cole-Cole parameters including the thickness are unresolved. However, looking at the posterior probability distributions, ρ is relatively high and the m_o relatively low compared to the surrounding layers.

In Figure 5.44, the step lengths are visible in the plot of τ , because they are scaled by the large uncertainty of the layer. It can also be seen more clearly on the marginal distributions in Appendix A.8, where the step lengths of m_o and C also become visible.

Even though ρ and the thickness of the layer is unresolved, the marginal distributions are approximately bell-shaped with maxima at $\sim 1500 \Omega\text{m}$ and $\sim 1.3 \text{ m}$ respectively.

Layer four

m_o and ρ of layer four are unresolved, but τ is moderately resolved to a value of 0.9 s and C is well-resolved with a density maximum at ~ 0.8 , which is above what is normally considered as the physical boundary of the frequency exponent. The correlation matrix shows a strong anti-correlation between ρ and m_o in the layer and a positive correlation between C and τ .

Linearized inversion results

The linearized inversion results fit well with the results of the MCMC inversion (Figure 5.44). The linearized results have a final data residual of 1.25, which is a good fit. The linearized uncertainty analysis in Table 5.4 also agrees very well with the analysis computed on the MCMC results. In a few cases where the Cole-Cole parameters are close to being unresolved, the linearized inversion overestimates the uncertainty (e.g. for $\rho_1, \rho_4, m_{0,4}$ and thk_l). In layer two, the linearized analysis underestimates the uncertainty of m_o and τ . However, as mentioned previously, in layer two the MCMC results are not fully converged, why it might be the MCMC analysis which has overestimated the uncertainties.

Layer	STDF(ρ)		STDF(m_o)		STDF(τ)		STDF(C)		STDF(thk)	
	MCMC	Lin.	MCMC	Lin.	MCMC	Lin.	MCMC	Lin.	MCMC	Lin.
1	1.87	-	1.16	1.17	1.10	1.14	1.02	1.07	1.92	-
2	1.02	1.01	1.11	1.07	1.44	1.24	1.04	1.03	1.14	1.14
3	3.17	-	6.52	-	245,45	-	9.68	-	3.20	-
4	2.42	2.68	2.42	2.51	1.26	1.24	1.10	1.15		

Table 5.4: Standard deviation factors (STDFs) of the Col-Cole parameters obtained from inversion of field data with a MCMC approach and a linearized (lin.) approach. A STDF > 2 is an unresolved parameter and for the linearized approach ‘-’ marks a completely unresolved parameter.

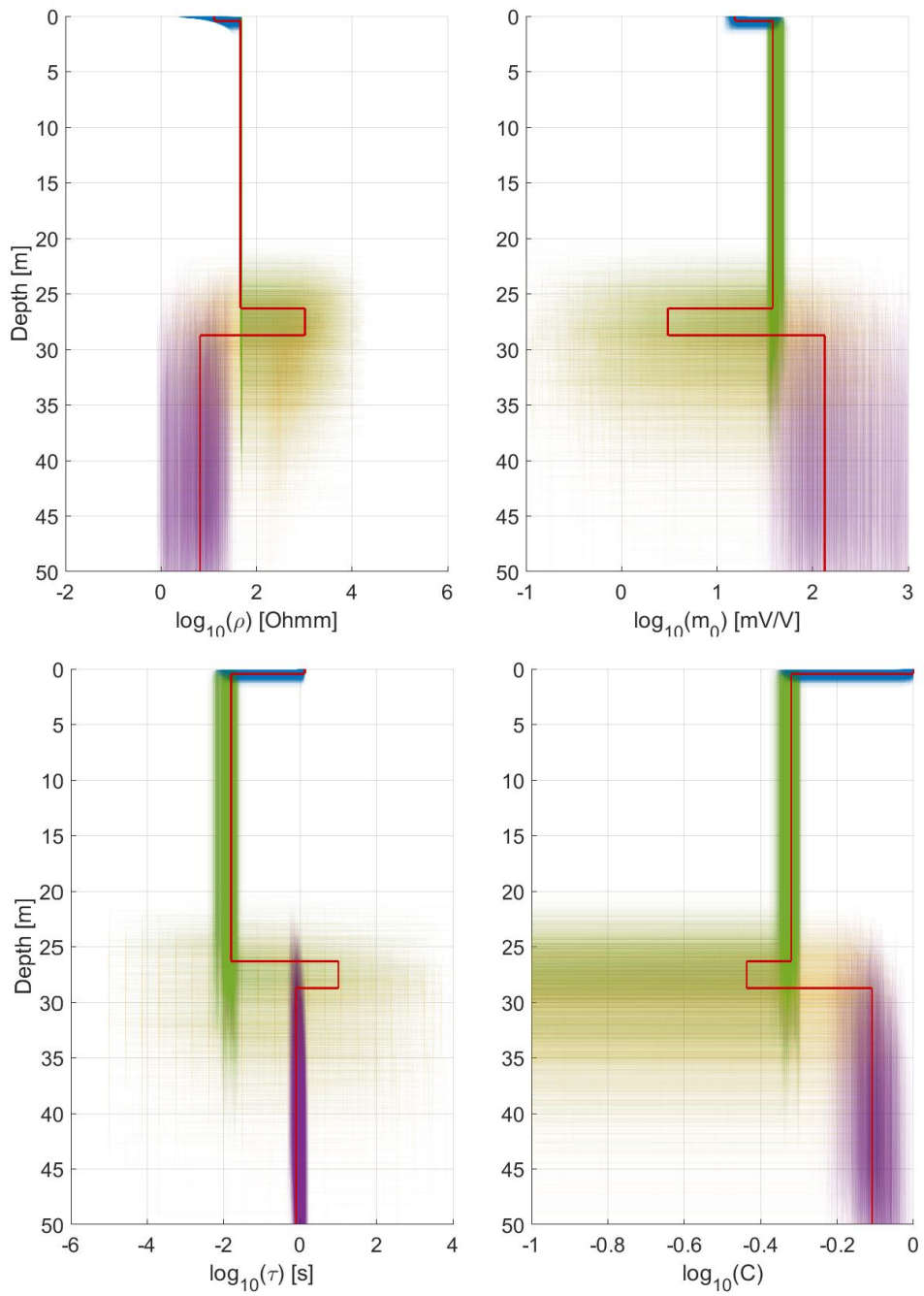


Figure 5.44: MCMC inversion results of field data from Samsø. The red line is the results of a linearized inversion with a final data misfit of 1.25. The result of the MCMC inversion is plotted as density clouds for layer one (blue), layer two (green), layer three (yellow), and layer four (purple).

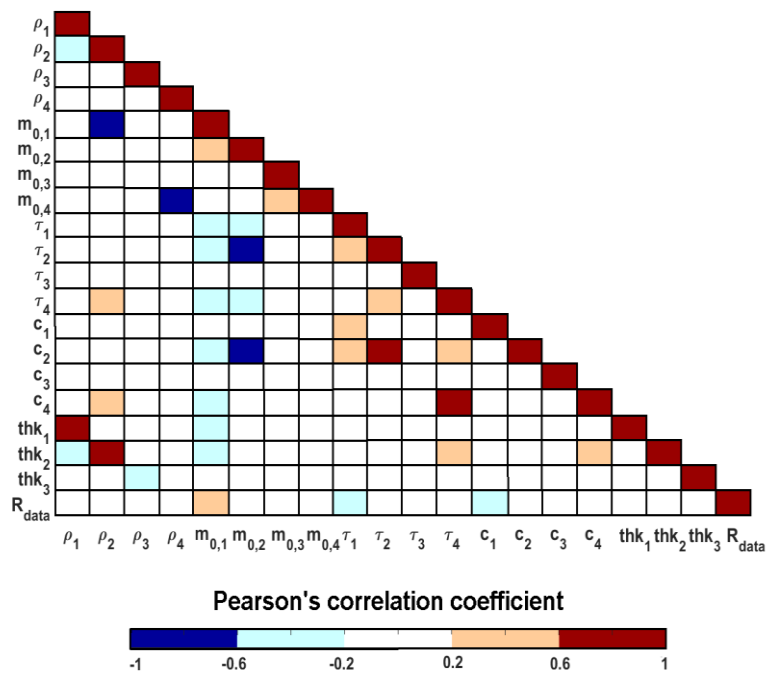


Figure 5.45: Correlation matrix for the Cole-Cole parameters determined from field data. The matrix holds the correlation coefficients between all the Cole-Cole parameters. Blue colors indicate an anti-correlation and red colors a positive correlation.

6 Discussion

In this chapter the results of the studies introduced in Chapter 4 will be discussed in connection with the research questions stated in the introduction. Before these questions are answered, a general discussion of the 1D Markov chain Monte Carlo (MCMC) algorithm used for all the studies is presented in the following section.

6.1 The MCMC algorithm

The MCMC method is capable of performing a full nonlinear analysis of the DCIP problem, which is not possible using a linearized approach. However, there are some general issues associated with the application of the MCMC method, which should always be considered before the method is applied in practice. These issues, and the solutions applied in this thesis, are discussed below. Furthermore, the advantages and disadvantages of a covariance scaled model proposer are discussed.

6.1.1 General implementation issues

One of the general problems associated with the MCMC method is to determine the length of the burn-in phase. The models, which make up this phase, must be removed from the Markov chain to reduce the risk of bias. This can be difficult because length of the phase varies for different probability distributions. Various techniques have been suggested to estimate the length (Brooks, 1998). In our MCMC algorithm the problem is solved by using a linearized inversion to find a maximum likelihood solution and using this as the start model for the Markov chain. The burn-in period is thereby skipped, because the chain is started inside the posterior probability distribution as illustrated by Figure 3.2.

Another issue is the choice of the start model. It may seem drastic to apply a linearized inversion started at the true model to determine the start model of a Markov chain as done here. It may be expected that this affects the extensiveness of the search of the model space. However, any interpretations based on MCMC samplings will be independent on the start values since the observations are made after the Markov chain has reached equilibrium and hence lost the dependence of those values. This is supported by the results of the convergence study presented in Figure 5.5. That study shows that the MCMC algorithms finds the same equilibrium independent of the start model. The choice of the start model may, however, still affect the pattern of the random-walk and especially the speed of convergence. This is evident for the MCMC algorithm applied in this thesis, because the step length directly depends on the start model. This aspect is discussed in the following section.

6.1.2 Scaling of model perturbation

Inversion of DCIP data with the MCMC method is highly time consuming compared to applying a linearized approach. However, by using a proposer algorithm in the MCMC code, where the step lengths are scaled according to the parameter uncertainty, the inversion time is reduced significantly. The study of convergence rates shows that a scaled proposer converges over 200 times faster than a Gaussian distributed one. The reduction of computation time is significant when multiple-layer models are inverted. The inversion

time for a three-layer model is approximately three hours on 10 CPU's when using a covariance scaled proposer, which should be compared to days of computation if a Gaussian proposer is applied. Even though the covariance scaled proposer reduces the computation time, it is still not close to being as effective as the linearized inversion in AarhusInv, where an inversion of a three-layer model takes only two seconds.

The scaling of the step length in our MCMC algorithm is given by the estimated covariance matrix from a linearized inversion. If the linearized result is far from the true model, or if the linearized uncertainty analysis is only valid very locally due to nonlinear functions, the scaling will not correspond to the uncertainty of the true model parameters. Often the scaling will be overestimated, because the estimation covariance matrix is computed for a model with a relative large uncertainties relative to the true model. The large steps can lead to a slowly converging Markov chain, which requires many iterations to converge to the desired posterior probability distribution. In this study, mainly synthetic data have been used where the start model of the linearized inversion was the true model. In this case, the scaling works ideally, because the estimated covariance matrix is computed for a model very close to the true model.

The general uncertainty analysis of the Cole-Cole parameters shows that the uncertainty of the time constant, τ , is relatively high and that the uncertainty of the resistivity, ρ , is relatively low. So, it can be argued that even though the scaling of the step length is computed from a model far from the true model, then the relative scaling of the model parameters is still useful and imposes a faster convergence compared to not using a scaling at all.

6.1.3 High dimensions

The final step length in the model space is a product of a predefined step length constant, k , and the scaling from the linearized estimated covariance matrix. For complex models with many layers, the predefined step length constant must be set to a relatively small value to obtain a satisfying acceptance rate of models to the Markov chain. When more layers are added to an inversion, the dimension of the model vector increases significantly. A step in the model space is taken for all model parameters at the same time, so the data misfit and thereby also the acceptance probability may change very fast when many dimensions are involved. By keeping the steps short, the model perturbation is kept to a minimum and the acceptance ratio is kept up. Smaller step lengths, however, lead to a slower convergence, why more iterations are required for high dimension problems to ensure that the entire probability region is covered.

It is possible to keep the acceptance rate around 20% for five-layer models, if the step length constant is 0.001-0.05 and the maximum perturbation is 1. This should be seen in contrast to the input of three-layer models, where the values are 0.1-1 and 5, respectively.

For models with more than five layers, it takes the MCMC algorithm more than 48 hours to converge. As the algorithm walks around the model space, the acceptance ratio keeps decreasing. If just one of the model parameters in one of the layers hits the model space boundaries, the model will not be accepted. The algorithm may get trapped for a while at the model space boundary, because it keeps suggesting models on the other side of the boundary causing the decrease in the acceptance rate, until it is led in another direction by the random-walk procedure. As the dimension of the problem grows, this will happen more frequently, meaning that it becomes more difficult to keep a satisfying acceptance

rate, and that the computation time increases exponentially as more layers are added to the inversion.

In the current state of the MCMC code, the models rejected by boundary constraints are part of the acceptance rate. Consequently, the acceptance rate gives the wrong picture of the change in data misfit in the respective part of the model space if many models hit the model space boundaries. This has, however, only affected the acceptance rate of the five-layer model (Section 5.5.2) and the field data (Section 5.8) where the boundaries were often hit. It was accounted for, when setting the step length constant, by studying the change of the data misfits in the Markov chain and the change in model parameters. In this way, it was possible to use a very small step length constant and at the same time make sure that a model perturbation was present.

In the case with the field data, the acceptance rate decreased from 60% to 2% from the beginning of the Markov chain and to iteration number 1,000,000. If a larger step length constant was applied, no models were accepted at all, and for smaller step lengths, the model perturbation was so small that only a very local area of the model space was searched. As a consequence, the MCMC algorithm was stopped before it reached a fully convergence for all model parameters, because with the low acceptance rate, it would take days for the algorithm to make any significant perturbation of the model vector. The posterior probability distributions, however, still give good approximations of the variance of the model parameters, because only the smoothness of the distributions are missing (see Appendix A.8). The results of the specific inversion are discussed later.

6.2 Resolution of Cole-Cole parameters

One of the main goals of this thesis is to investigate whether it is possible to resolve the spectral Cole-Cole parameters from time-domain DCIP data. An assessment of this is presented here with references to the individual studies carried out in the thesis.

First the uncertainty analysis of the Cole-Cole parameters will be discussed. Pitfalls in the analysis will be presented and a summation of the general tendencies will be given. Hereafter, results from time-domain data will be compared to the results from frequency-domain produced by Ghorbani *et al.* (2007). This is followed by a discussion of the impacts of acquisition range and parameter correlations.

6.2.1 Uncertainty analyses

The uncertainty analysis of the Cole-Cole parameters is based on the standard deviation factors (STDFs). The STDF of a Cole-Cole parameter expresses the variance of the marginal posterior probability distribution from its mean. If a distribution is strongly skewed, so the median is far from the mean, the STDF will not reflect the variation from the distribution maximum, why comparative consistency between analyses will be lost. It is, however, justified to use the STDFs for the mildly nonlinear problem of DCIP, because most of the probability distributions in this thesis are approximately Gaussian or bell-shaped with a maximum close to the mean. The influence of skewness on results obtained from a linearized inversion approach is discussed in Section 6.3.

The STDFs of the posterior probability distributions may vary slightly between repeated MCMC runs. This happens if the runs do not find exactly the same equilibrium each time. However, in this thesis the variation of the STDFs between repeated runs was below 5%

for homogenous half-spaces, which does not have a significant influence on the final results.

Homogenous half-spaces

The uncertainty analyses performed on homogenous half-space models in Section 5.2.2 show that the spectral Cole-Cole parameters are resolved from time-domain DCIP data.

The resistivity, ρ , is in all tested models well-resolved and does not show any strong correlations to the IP parameters, because ρ does not have a direct influence on the IP signal. If ρ is changed, but the IP parameters are kept constant, then the IP decay will be unchanged, because the data space chargeability describing the decay is normalized by the ρ as seen in Eq. (2.7). As a consequence, the magnitude of ρ does not show any significant influence on the resolution of the IP parameters when $\rho > 10 \text{ } \Omega\text{m}$ (Figure 5.6). It is, however, expected that the resolution of all the parameters would decrease significantly for smaller ρ , because ρ has a direct influence on the magnitude of the IP potential and thus the signal-to-noise ratio as seen in Eq. (2.8).

The values of the chargeability in the model space, m_0 , also have a direct influence on the magnitude of the IP signal in the time-domain (Figure 2.9). In frequency-domain, m_0 controls the magnitude of the imaginary response of the complex resistivity, which shows the phase shift between current and potential relative to frequencies (Figure 2.8). When m_0 decreases, the magnitude of the phase shift curve decreases and it becomes difficult to distinguish the features at the peak frequency, which determine the IP parameters including m_0 itself.

Figure 5.7 shows that for models with m_0 below 50mV/V, the IP parameters are all unresolved. When the magnitude of the IP signal comes below the defined voltage threshold noise, the error bars on the data become very wide. As a consequence, the posterior probability distributions will have a large variance, because the IP decays, which fall within the error bars, may come from very different models.

The Cole-Cole parameters are best resolved for values of the time constant, τ , between 0.01 s and 1 s (Figure 2.11). For higher and lower values, the resolutions of m_0 and τ itself are poor or completely unresolved. This can be explained by the following: As τ increase, the decay of the DCIP signal will set in at later times as shown in Figure 2.10. This also means that if τ is low the measured potential, $V(t')$, will rise more slowly after the current is turned on and might not converge fully before the pulse is reversed. As a consequence, the DC resistivity, V_{DC} , will be lower than the actual value. This makes it more difficult to resolve the resistivity. If V_{DC} drops significantly, the magnitude of the IP potential will also decrease as mentioned earlier, and the IP parameters will be more difficult to resolve due to the influence of the voltage threshold noise. For small values of τ , the IP signal will drop significantly fast and the signal-to-noise ratio will decrease, because the signal will approach the voltage threshold in this way as well.

In frequency-domain, τ determines at which frequencies the IP effect can be observed, i.e. the frequencies close to the peak frequency. As τ is changed, the peak frequency is shifted up and down the frequency spectrum (Figure 2.8). For large values of τ , the peak frequency is seen at relative small frequencies and for a small τ at relative high frequencies. So, if measurements are performed with a frequency interval, which does not include the peak frequency, then it cannot be expected that the IP parameters can be resolved. The same is valid in the time-domain. If τ falls outside the acquisition range it

cannot be expected that the IP parameters are resolved, because the part of the signal, where the spectral information is present, will be outside the acquisition range.

The standard acquisition range used in this thesis is 2.59 – 4000 ms. So, the bad resolution of the IP parameters at high and low values of τ (below 1 ms and above 10,000 ms) seen in Figure 5.9 could also be caused by τ being outside the acquisition range as described above. However, that does not correspond well with C being well-resolved, why the bad resolution is interpreted as a consequence of a low signal-to-noise ratio caused by early and late decays of the IP signal as described previously.

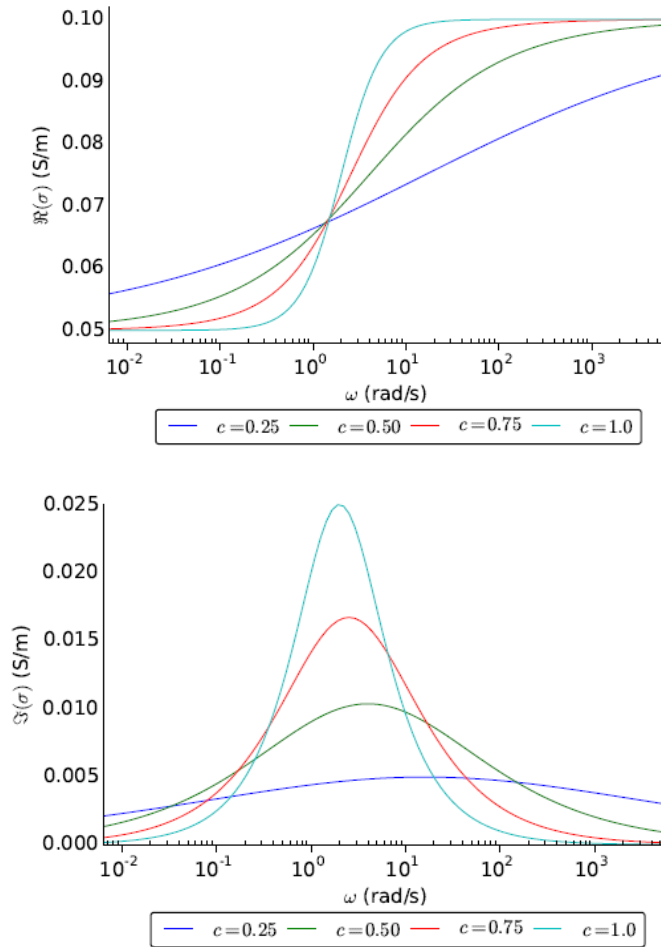


Figure 6.1: Magnitude (top) and phase (bottom) curves for the Cole-Cole model here presented as the real and imaginary part of the complex conductivity ($\sigma = 1/\rho$). The model has $\rho = 100 \Omega\text{m}$, $m_0 = 500 \text{ mV/V}$, $\tau = 1 \text{ s}$, and C varying between 0.25 and 0.75. The figure shows that as C decreases the change in magnitude happens continuously and the phase peak decreases, which makes it difficult to determine the peak frequency that is used to determine τ . The figure is modified from Marchant (2015).

In frequency domain, the frequency exponent C controls the dispersion of frequencies. If C is low, the peak of the phase shift will be wide and span many frequencies as seen in Figure 6.1. This makes identification of the key peak frequencies difficult, why m_0 , τ , and C

itself will be difficult to resolve. This is also the tendency seen in Figure 5.10: The uncertainty analysis shows that the IP parameters, especially τ , cannot be resolved well for $C < 0.4$. However, only τ becomes completely unresolved for very low values of C . In frequency-domain, this means that the height and the width of the phase peak, which are described by C and m_0 respectively, can be estimated, but the exact location of the maximum, which is a function of τ , is not as well determined (Figure 6.1).

Generalization of uncertainties on Cole-Cole parameters

The observations of the sensitivity of the Cole-Cole parameters discussed above rely on studies of a selection of models and are therefore not necessarily representative for all combinations of Cole-Cole parameters. The models analyzed have a noise model with a 2% STD on the resistivity, 5% on the chargeability, and a 0.1 mV voltage threshold. If the noise is increased, the uncertainties will increase as well.

The following tendencies have been observed on the homogeneous half-spaces as well as more complex models in this thesis. In general, it can be stated that the resolution of the Cole-Cole parameters decreases as the value of C decreases. The same is valid for a decrease in m_0 . It can also be concluded that a good resolution of τ is difficult to obtain and that the STDF of τ typically is above 1.2. The resolution of the IP parameters also decreases with depth, because the geometric factor increases, which according to Eq. (2.10) decreases the IP potential.

Errors associated with complex models

For very complex models with strong equivalences, one must be cautious before relying exclusively on MCMC uncertainty analyses. Figure 6.2 shows an example of a model where the MCMC analysis says that C_2 is moderately resolved (STDF = 1.4) even though the posterior probability distribution is not consistent with true model. This occurs because the inversion does not resolve the middle layer of the model. The STDF of C_2 is then computed from the mean value of the distribution, which is close to $C_{1,true}$ and $C_{2,true}$, but far from $C_{2,true}$. The STDF is low, because the variance of the posterior probability distribution is small even though it is not descriptive of C_2 . So, because the layer is not resolved, the STDF becomes misleading.

This means that for complex models, the MCMC uncertainty analysis should always be interpreted together with the posterior probability distributions. However, in this study, the misleading STDFs have only been observed for this one example, where the parameter contrast is very low, and for thk_2 in the five-layer model in Section 5.5.2, why it should not be seen as a general problem associated with the method.

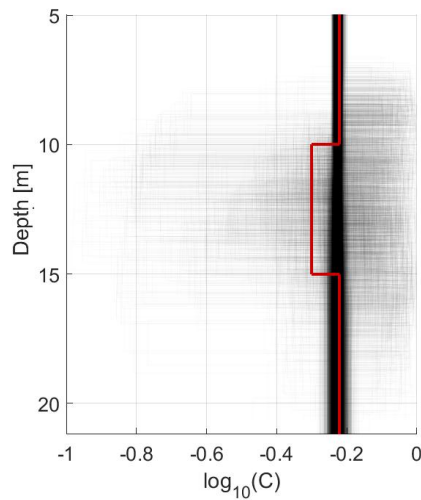


Figure 6.2: Example of a model where the MCMC inversion does not resolve a small imbedded layer, but the uncertainty analysis tell that it is resolved because the standard deviation factor is computed as the variation from the mean, which in this case is far from the true model (red line). The black lines shows the model density in the posterior probability distribution.

6.2.2 Model from Ghorbani *et al.* (2007)

Ghorbani *et al.* (2007) presented four homogenous half-space models, where the Cole-Cole parameters could not be determined from time-domain data by the applied inversion scheme. However, the results from Section 5.3 show that it is possible to resolve the Cole-Cole parameters from time-domain with the novel MCMC algorithm used in this thesis. The new results show posterior probability distributions of the Cole-Cole parameters, which are unimodal and approximately bell-shaped with strong approximately linear correlations between the parameters.

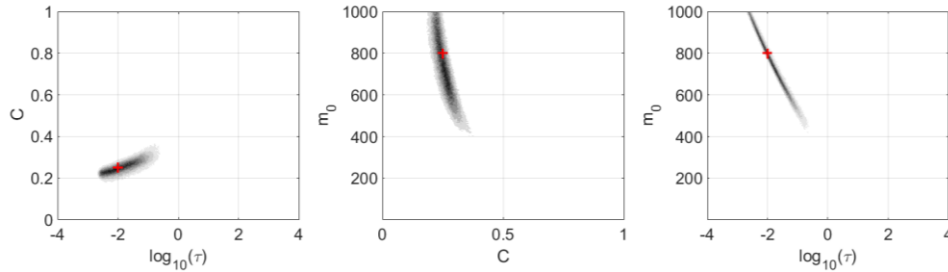
Fiandaca *et al.* (2012) discussed that the bad results produced by Ghorbani could be caused by the choice of τ ($\tau = 0.01$ s), which is earlier than the time of the first measurement ($dly = 0.02-0.04$ s). However, the value of τ is not directly equal to the reciprocal peak frequency, why the peak frequency for $\tau = 0.01$ is not necessarily outside the acquisition range (Kemna, 2000). In this study the same acquisition range is used but does not cause any undetermined parameters, except for τ , why the poor gating does not explain the unresolved models produced by Ghorbani.

Another difference between the two studies is the accuracy of the forward code. The approach used by Ghorbani does not have an accurate implementation of the waveforms, which have been proven crucial in resolving Cole-Cole parameters from time-domain data (Fiandaca *et al.*, 2012).

Figure 6.3 shows a comparison of MCMC inversion result of time-domain data from this study (a) and inversion result from frequency-domain produced by Ghorbani (b). The two results are very much alike. The two plots to the right produced by Ghorbani show two maxima: One maximum close to the true model and one maximum at the upper boundary of the chargeability. This may reflect errors concerning the boundary conditions and can also be observed on their results from time-domain (Appendix A.4). This comparison

supports that the resolution of the Cole-Cole parameters obtained from time-domain data is equivalent to the resolution gained from the frequency-domain.

a) MCMC inversion results from time-domain data



b) Results from frequency-domain data produced by Ghorbani *et al.* (2007)

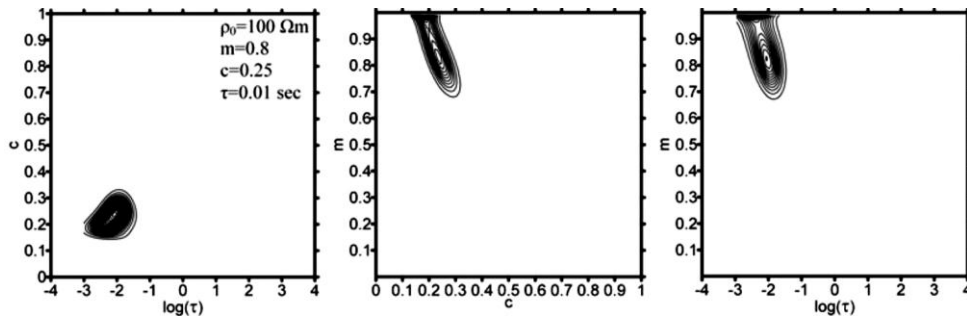


Figure 6.3: Comparison of inversion results of data from time-domain (a) and frequency-domain (b). The figures show that the resolutions gained from the two approaches are very similar.

6.2.3 Acquisition range

The acquisition range used for measuring time-domain DCIP data is proven very important for the resolution of the Cole-Cole parameters. Figure 5.14 to Figure 5.18 clearly show the trend on a homogenous half space: Acquisition ranges under three decades cannot resolve the spectral content of the IP signal properly. The same result is shown for a three-layer model in Appendix A.6.

The resolution of the two largest acquisition ranges applied in the study in Section 4.4 may be overestimated compared to what would be expected from field measurements. The gating starts after only 1 and 2.59 ms. At these early times, the signal is often weakened by coupling due to the change of sign of the injected current. For this reason, the early gates are often deleted in data processing as seen on the field data in Figure 4.1. This is not accounted for in the study of synthetic data. The information lost by deleting the first few gates is, however, not enough to change the conclusion that an acquisition range in the neighborhood of the standard used in this thesis (2.59-4000 ms) is required for a good resolution of the Cole-Cole parameters.

The studies of acquisition ranges also show, that the range has an influence on the linearity of the correlation between the Cole-Cole parameters. Figure 6.4 compares the cross-correlation of C and m_0 resolved with a 10-1000 ms acquisition range (left) and a 2.59-4000 ms acquisition range (right). The shape of the probability density to the left is nonlinear, while the right figure shows a linear correlation. So, the longer the acquisition range, the more linear and better resolved are the probability distributions. The magnitude of the correlation is, however, not changed, meaning that very well resolved parameters can show the same degree of correlation as bad resolved once.

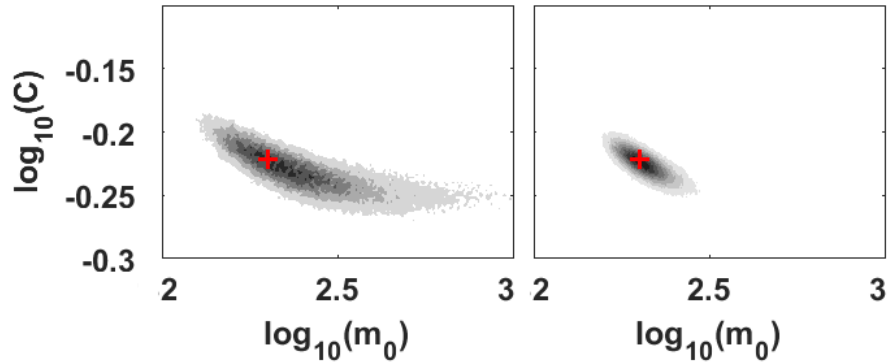


Figure 6.4: Posterior probability densities computed from two different acquisition ranges: 10-1000 ms (left) and 2.59-4000 ms (right). For the smaller acquisition range, the correlation between m_0 and C is nonlinear. The figures are outcrops of Figure 5.16 and Figure 5.17 in the result chapter.

6.2.4 Parameter correlation

An MCMC analysis makes it possible to study the correlations between the Cole-Cole parameters. If two parameters are correlated it will appear when the two marginal posterior probability distributions are plotted against each other as a linear or nonlinear trend.

Pearson's correlation coefficient (PPC) detects linear relationships between model parameters. The coefficient is therefore both a measure of correlation and linearity. This limits the method if the correlation between two parameters is nonlinear. For strong nonlinear relationships, the method will underestimate the correlation. In this study, the correlations are computed on the logarithmic transform of the model parameters, which imposes linearity. For the models where the correlations are studied, no strong nonlinearities have been observed in the logarithmic space, why PPC in this situation can be applied as an indicator of the degree of correlation between the Cole-Cole parameters.

An anti-correlation is observed between m_0 and C . For most models and layers, the correlation is strong with PCC between -0.6 and -1. Some models show a strong m_0 - C anti-correlation in well-resolved layers and only a mild correlation in poor resolved layers (e.g. Figure 5.25, where layer one, two, three, and five have a strong m_0 - C anti-correlation, but layer four, which is unresolved, has only a mild m_0 - C anti-correlation. In Figure 5.29, the

IP parameters of layer three are unresolved and the layer does not show a m_0 - C correlation opposite the other layers). A positive m_0 - C correlation is observed in a single case in Figure A.28. This correlation is mild and appears in a complex model, why it does not change the general trend of an anti-correlation between C and m_0 . The m_0 - C anti-correlation can be understood by studying the IP signal in time-domain. If m_0 is decreased in a default model, the magnitude of the IP signal also decreases. To obtain a model equivalent to the default model, the value of C can be increased, which increases the magnitude of the signal again. This gives two equivalent models, one with a high m_0 and low C and one with a high C and a low m_0 .

Strong correlations are also observed between the Cole-Cole parameters m_0 and τ and between τ and C . This is, however, not as frequently observed as the m_0 - C anti-correlation. The strong correlations to τ are always coexisting: If τ is negatively correlated to C , then τ is also positively correlated to m_0 , due to the m_0 - C anti-correlation. There is no straight forward pattern describing when the correlations of C and m_0 to τ are negative or positive.

As expected, models with resistivity equivalences show strong correlations between the resistivities and the layer thicknesses as described in the result chapter (see Section 5.6). For a three-layer model with high resistivity equivalences in the middle layer, the correlation between ρ_2 and thk_2 is negative. So, if one of the parameters is changed the resistance is kept constant, because a thinner layer needs a higher resistivity to give the same response. For a low resistivity equivalence, the ρ - thk correlation is positive. If the low resistivity layer gets thinner, then the resistivity must also decrease to give the same response relative to the other layers. The correlation between resistivity and thickness is also seen in models where the difference between equivalent models is so small that the parameters are well-resolved, why a strong correlation cannot be used as an indicator for high or low resistivity equivalence or equivalence of very different models in general.

In complex three-layer models parameter correlation across layer boundaries and parameters are observed for IP parameters when the layer contrast is very small or non-existing. An example is Figure A.27, where $m_{0,2}$ is strongly correlated to $m_{0,3}$, τ_2 to τ_3 , C_2 to C_3 , but also $m_{0,2}$ to C_3 , and C_2 to $m_{0,3}$. Despite the strong correlations, all the parameters are well-resolved, meaning that the involved equivalent models are very similar.

6.2.5 Field data

The inversion results of the field data from Samsø support the results from the analyses of synthetic datasets. The data were inverted with a four layer model (Figure 5.44). The results show a decreasing resolution with depth. Layer three in the model is very thin (below 3 m) and lies in a depth of 27 m. As expected, the Cole-Cole parameters of that layer are unresolved, however the resistance is moderately resolved and there is a ρ - thk anti-correlation. Combined, this indicates a high resistivity equivalence. Despite the equivalence, the marginal posterior probability distributions of the resistivity and the thickness are unimodal and approximately bell-shaped, why their maxima are a good approximation for the geoelectric model.

The typical m_0 - C anti-correlation appears in one of the layers from the field data. In the same layer, C is positive correlated with τ and τ is anti-correlated with m_0 , which was also observed in the synthetic data.

6.3 Linearity of the DCIP problem

The advantage of performing a MCMC inversion of the DCIP problem instead of using a linearized approach, is the possibility of studying a full nonlinear solution. This allows assessment of the accuracy of the linear approximation and the estimated covariance matrix, which are applied and produced by AarhusInv. The purpose of the following sections is to make such an assessment based on the MCMC results in this thesis.

6.3.1 Posterior probability distributions

The result of an iterative solution to a nonlinear problem is not guaranteed to converge to the global minimum of the misfit function, because it may converge to a local minimum as discussed previously. Figure 6.5 shows the connection between the degree of linearity of a forward equation and the corresponding posterior probability distributions. The plot to the left illustrates that, when a posterior probability distribution is Gaussian, then the forward function is linear. If the forward function is strongly nonlinear, then the distribution will be far from Gaussian, as seen on the plot to the right. The middle plot shows a forward function, which is mildly nonlinear. In this case the distributions will be approximately Gaussian as seen for most results in this thesis.

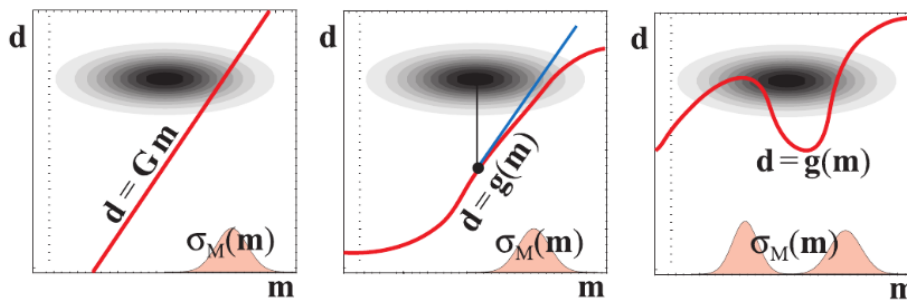


Figure 6.5: Connection between the forward equation, $d = Gm$, and posterior probability distributions, here referred to as σ_M . The density clouds represents the probability density including both the information on the observed data and the priors. In the first sketch, the forward equation is linear. The posterior probability distribution is then Gaussian. In the second sketch, the forward equation can be linearized around a model m given the Taylor expansion. Here, the posterior probability distribution is approximately Gaussian. In the third sketch, the forward equation cannot be linearized and the posterior probability distributions is far from Gaussian. The figure is modified from Tarantola (2005).

Figure 6.6 shows three different shapes of posterior probability distributions observed in this thesis. Figure 6.6a is a unimodal distribution. The distribution is approximately Gaussian, so the corresponding forward function can be linearized according to Figure 6.5. When a posterior probability distribution has only one maximum, the corresponding misfit function has only one minimum as well (Tarantola, 2005). Consequently, a linearized inversion does not risk converging to a local minimum, because no such exists. Most of the inversion results in this thesis resemble Figure 6.6.a.

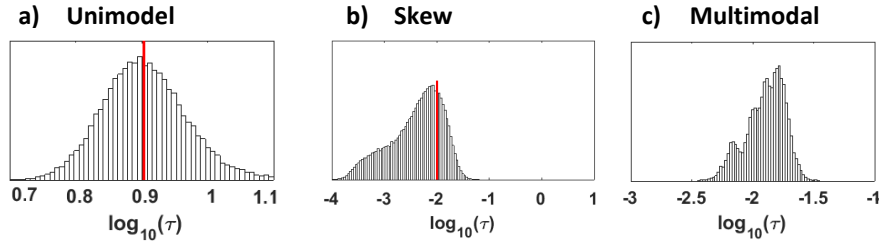


Figure 6.6: Examples of different types of posterior probability distributions obtained by the MCMC inversions in the thesis. Left: Unimodal distribution from Figure A.19. Center: Skewed unimodal distribution from Figure 5.17. Right: Multimodal distribution from Figure A.33.

Figure 6.6b shows a left-skewed distribution. In this thesis, skewness has particularly been observed for posterior probability distributions of τ and m_0 (e.g. Figure 5.16). The direction of the skewness varies and no trend has been observed. By applying different acquisition ranges to the DCIP data, it was found that the skewness of the distributions decreases as the acquisition range, and thereby the resolution of the Cole-Cole parameters increase.

As described previously, skewness of a distribution affects the STDFs. If a high degree of skewness is present, the STDFs of different models and parameters are no longer comparative, because the STDF is an expression of the variance from the mean. This holds for both the linearized inversion and the MCMC inversion, but in the MCMC analysis, the skewness can be identified on the posterior probability distribution and taken into account when interpreting the STDFs. This is not possible with the linearized approach, why the estimated errors on the Cole-Cole parameters loose comparative consistency if the distributions are skewed. However, the skewed distributions are mostly observed in badly resolved models, why well-resolved models are assumed not to be affected.

Figure 6.6c is an example of multimodality seen in the model of the field data. If this multimodal distribution reflects the true possibility distribution, then a linearized approach will probably fail to find the global maximum. However, such multimodal distributions are only observed on the field data and it is expected that the local maxima are only present because too few iterations have been used and that the Markov chain has not converged completely. This hypothesis is supported by the convergence analysis in Section 5.1, where the distributions also showed multimodality before converging to the final bell-shaped posterior probability distribution (see Figure 5.1).

So, aside from not fully converged results, the MCMC analysis shows that the posterior probability distributions of the Cole-Cole parameters have only one maximum and that the distributions are approximately bell-shaped for well-resolve parameters, which means that the linearized inversion approach applied by AarhusInv is justified for these models.

6.3.2 Linearized inversion results

In Section 5.2.2, the MCMC uncertainty analysis of the Cole-Cole parameters is compared to the linearized estimated uncertainty analysis computed by AarhusInv. For well-resolved Cole-Cole parameters the two analyses agree very well, but when the parameters become unresolved, the linearized approach tends to underestimate the uncertainty on

the IP parameters. Examples are shown in Figure 5.7 and Figure 5.10 where the MCMC analysis finds that the IP parameters are unresolved (STDFs > 2) for low values of m_o and C , while the linear approximation finds STDFs below 2. In this specific cases, the difference is caused by the nonlinearity induced by the low signal magnitude due to low values of m_o and C . As the correlation between parameters become more nonlinear and the marginal distributions are no longer bell-shaped, the linearized approach breaks down, because the observational data become a more nonlinear function of the model. For the nonlinear functions, the Taylor expansion used for linearization becomes valid in a very local area of the function, and the uncertainty analysis is therefore also valid locally in in the model space.

A comparative analysis of the MCMC and the linearized inversion approach was also carried out on field data (Table 5.4). For the resolved Cole-Cole parameters the two approaches found the same parameter values and the uncertainty analysis agreed very well for all parameters, resolved and unresolved, with differences in STDFs below 0.24. This again demonstrates that a linearization of the DCIP problem is justified because a linearized inversion approach gives the same results as a full nonlinear MCMC inversion.

6.4 Information from IP

Recording, processing and inversion of the IP part of the DCIP signal is very time consuming, why DCIP is also an expensive method to apply in surveys compared to applying the DC method alone. A MCMC inversion of a three-layer model with 500,000 iterations takes approximately 3 hours for DCIP data and only 30 s for DC data alone, when the computations are running on 10 CPUs.

It has been questioned, if IP is worth its expenses. The arguments are based on studies not capable of resolving the IP parameters from time-domain (e.g. Ghorbani *et al.*, 2007), but it is also based on the fact that the relations between the Cole-Cole parameters and well-known physical properties of the subsurface, e.g. grain size or types of contamination, are not fully understood yet, which makes the application of the method difficult to define.

In the following sections the contribution from the IP part of the DCIP signal will be discussed with references to the results of the MCMC inversions carried out in this thesis.

6.4.1 Resistivity equivalences

The presented studies of resistivity equivalences show that the IP signal does not only add information about the spectral IP parameters, but it also help resolving resistivities and may decrease the number of equivalent models in an inversion.

For a three-layer model with a high resistivity equivalence, the studies presented in Section 5.6.1 show that the ρ -*thk* equivalence is resolved when different IP parameters are added to the layers (see Figure 5.27 and Figure 5.31). The better resolution of the model is caused by the extra information added by the IP signal. The contrasts in the IP parameters between the layers make it possible to determine the layer thicknesses and thereby decrease the number of equivalent models significantly. In the model studied here, it is found that a layer contrast in the chargeability of a factor four is enough to solve the associated resistivity equivalence.

The studies of this thesis also show that even if no information on the layer thickness is given by the IP parameters, e.g. if there is no contrast in the m_0 , τ or C between the layers, the IP signal still adds information to the resistivity and helps solve layer boundaries (see example in Figure 5.36 and Figure 5.37).

The IP signal does not have a direct influence on the resistivity. If the resistivity of a default model is changed, but the three IP parameters are unchanged, then the IP decay of the new model will be the same as for the default model. So, it is difficult to understand the influence from the IP parameters in this case. In the MCMC algorithm, the data misfits of the models in the model space influence which models are accepted to the posterior probability distribution and which are not. The data misfit carries more information when the IP parameters are added, because the uncertainties on the additional parameters are added to the misfit computation. However, to understand the contribution from the IP signal in this case, more tests are needed.

The difference which is observed between the DC and the DCIP inversion results discussed above, can also be caused by some numerical differences, e.g. different step lengths or different model acceptance rates during the MCMC sampling. A way to exclude that the difference between the DC and the DCIP signal is caused by a numerical error, is by doing a MCMC inversion of the DCIP data again, where the IP parameters are locked, meaning that very tight constraints are put on the IP values, so they are unchanged through the entire Markov chain. It is then expected that the DCIP inversion will give the exact same result as the DC inversion, but if that is not the case, then the comparative results must be influenced by numerical errors.

6.4.2 Resolution of layer boundaries

To analyze the ability of the individual IP parameters to resolve a layer boundary, a three-layer model was constructed with the same Cole-Cole parameters in all three layers. By changing the values of one of the IP parameters in the middle layer, it was found that a layer contrast in the chargeability gives the best resolution of the layer thicknesses, but that all IP parameters can resolve an imbedded layer, if there is a factor ten contrast in just that parameter. For a contrast in τ , the value for τ itself could not be resolved and for a contrast in C none of the IP parameters were resolved, but the layer thickness was still found.

The studies show that no equivalences between the IP parameters and the layer thickness exists as observed between the resistivity and the thickness. This means that the IP parameters theoretically have an advantage over the DC resistivity when it comes to resolving layer boundaries.

6.5 Prospects and further work

The scope of this thesis has been to carry out a MCMC analysis of Cole-Cole parameters for time-domain DC and DCIP data. As the analysis has been completed and the research questions have been answered, no further tests on DCIP data are required using the MCMC algorithm in hand. However, it could be useful to make a corresponding MCMC analysis of data from frequency-domain. By applying the same algorithm and formulations to a study of frequency-domain data, it would be possible to make a more accurate comparative analysis between the time-domain and frequency-domain DCIP method.

In the grater picture, the results of this thesis have bought new knowledge to the field of geoelectric methods. The main new findings include that:

- The spectral Cole-Cole parameters can be resolved from time-domain DCIP data using an acquisition range comparable to the standard at the HydroGeophysics Group (2.59-4000 ms).
- The linear approximation of the time-domain DCIP problem applied in the inversion software, AarhusInv, is justified for resolved models.
- Information gained from the IP part of the DCIP signal helps resolving layer boundaries and minimizes model equivalences.

These research results will hopefully open up for even more research and continuous development of the time-domain DCIP method, which can be beneficial for the application of the method in the field and for environmental investigations.

As stated in the introduction of this thesis, the DCIP method is being applied for mapping of subsurface contamination in projects aiming to protect the groundwater and keep it as a clean drinking water resource. If more research is carried out in order to understand the IP response of different contaminants in the subsurface, this would improve the benefit of applying DCIP in such environmental investigations. Furthermore, improvements of measurement techniques and inversion software for faster and less expensive data acquisition and analysis would make the DCIP method more desirable also outside the scientific community.

7 Conclusion

The Markov chain Monte Carlo (MCMC) inversion method has been applied to time-domain direct current (DC) and induced polarization (IP) data. The MCMC method allows a full nonlinear analysis of the DCIP problem, which is not possible applying a linearized inversion approach as the one used in the inversion software AarhusInv (Auken *et al.*, 2014).

In this thesis, inversion of synthetic time-domain DCIP data was carried out to retrieve the spectral Cole-Cole parameters. All computations and analyses were performed with a logarithmic transform of the model parameters as used by AarhusInv to impose linearity. The following conclusions refers to the Cole-Cole parameters with this transform.

The MCMC inversion method requires great computational power and time compared to the linearized approach. A study shows that the convergence time of a MCMC inversion can be reduced with over 90% by scaling the model perturbation of the Metropolis-Hastings sampling algorithm according to the uncertainty of the Cole-Cole parameters. Using this novel proposer algorithm, the computation time for a MCMC inversion of a three-layer model was brought down to three hours using 10 CPUs, which should be compared to below 30 s for a linearized inversion.

The MCMC analyses in this thesis show that the spectral Cole-Cole parameters can be resolved from time-domain DCIP data. The obtained posterior probability distributions are approximately bell-shaped with the maxima close to the true model values. The results from this thesis are equivalent - in term of uncertainty and results - to results obtained from frequency-domain in other studies.

A limiting factor in the resolution of the Cole-Cole parameters is the magnitude of the chargeability, m_0 . An analysis of parameter sensitivity carried out on homogenous half-spaces showed that as m_0 decreases in a model, the resolution of all the IP parameters decreases as well, because a decrease in m_0 leads to a decrease in the magnitude of the IP potential and therefore weakens the signal-to-noise ratio. The same holds for a decrease in the frequency exponent, C . For the synthetic data examined, the Cole-Cole parameters could not be resolved for m_0 below 10 mV/V or a C below 0.2. It was also found that the resolution of the IP parameters decrease significantly if the time constant, τ , gets below 0.01 s or above 10 s. In general, τ is the most difficult Cole-Cole parameter to resolve. These results from homogenous models were supported by similar results from more complex models and a field example.

Another limiting factor in the resolution of the Cole-Cole parameters is the applied acquisition range. As the acquisition range is decreased, the resolution of the IP parameters decreases as well and the posterior probability distributions become unsymmetrical. So, to obtain usable information from inversion of IP data, it is important to use a minimum acquisition range similar to the standard used by HydroGeophysics Group, which is the IP signal from 2.59 ms to 4000 ms.

The results of this thesis show that the Cole-Cole parameters are dependent. Correlation factors computed from cross-plots between the marginal posterior probability distributions of the Cole-Cole parameters show a strong anti-correlation between m_0 and C . Strong correlation are also observed between the remaining IP parameters, but not with

the same frequency or consistency as the m_0 - C anti-correlation. The correlations between the parameters were found to be approximately linear for resolved models. However, the linearity breaks down as parameters become unresolved, e.g. if the acquisition range is decreased.

Strong correlations are present between layer thicknesses and resistivities in models with high and low resistivity equivalences. This thesis shows that the IP part of the DCIP signal plays an important role in resolving layer boundaries in such models, because no equivalences or correlations are present between the layer thickness and the IP parameters. So, the DCIP method resolved layers which could not be resolved with DC data alone. It is found that a contrast in m_0 of a factor two between two layers is enough to resolve a layer boundary in an else homogenous model when the imbedded layer is half the thickness of the overlying material. The same results were found for C , while it was more difficult to resolve the layer boundaries from a contrast in τ .

The results of the MCMC sensitivity analysis were compared to estimated uncertainties from the linearized approach. It was found that the two approaches agree well for resolved models, but as the Cole-Cole parameters become unresolved and nonlinearity is increased, the linearized approach tends to underestimate the uncertainty of the parameters.

This thesis shows that the time-domain DCIP forward problem behaves approximately linear for resolved models. Unimodal and bell-shaped posterior probability distributions supports that the misfit function has only one minimum, why a linearized approach does not risk solving a secondary local minimum. The results also support a justification of a linearized uncertainty analysis for resolved parameters. Furthermore, it is established in theory that the application of IP data helps resolving model geometries, which cannot be resolved from DC data alone.

8 References

- Auken, E. & Christiansen, A. V. (2004): Layered and laterally constrained 2D inversion of resistivity data. *Geophysics*: **69**, 752-761.
- Auken, E., Christiansen, A. V., Jacobsen, B. H., Foged, N. & Sørensen, K. I. (2005): Piecewise 1D Laterally Constrained Inversion of resistivity data. *Geophysical Prospecting*: **53**, 497-506.
- Auken, E., Christiansen, A. V., Kirkegaard, C., Fiandaca, G., Schamper, C., Behroozman, A. A., Binley, A., Nielsen, E., Effersø, F., Christensen, N. B., Sørensen, K. I., Foged, N., and Vignoli, G. (2014): An overview of a highly versatile forward and stable inversion algorithm for airborne, ground-based and borehole electromagnetic and electric data. *Exploration Geophysics*: **46**(3) 223-235.
- Barlow, R. J. (2008): *Statistics: A Guide to the Use of Statistical Methods in the Physical Sciences*. Manchester. John Wiley & Sons Ltd.
- Binley, A., Slater, L. D., Fukes, M. & Cassiani, G. (2005): Relationship between spectral induced polarization and hydraulic properties of saturated and unsaturated sandstone. *Water Resources Research*: **41**, 1-13.
- Brooks, S. P. (1998): Markov chain Monte Carlo method and its application. *The Statistician*: **47**, Part 1, 69-100.
- Christensen, N. B. (2012). Environmental applications of geoelectric methods.
- Cole, K. S. & Cole, R. H. (1941): Dispersion and absorption in dielectrics. *Journal of Chemical Physics*: **9**, 341-351.
- Dahlin, T., Bernstone, C. & Loke, M. H. (2002): A 3-D resistivity investigation of a contaminated site at Lernacken, Sweden. *Geophysics*: **67**, 1692-1700.
- Dahlin, T. & Leroux, V. (2010): Full wave from time-domain IP data acquisition, in: 16th European Meeting of Environmental and Engineering Geophysics.
- Dinesen, B. (1962): Geoelektrisk kortlægning af Limfjordsengene ved Vestre Hassing. DGU III. Rk. **Nr. 35**, 1962.
- Doetsch, J., Fiandaca, G., Auken, E., Christiansen, A. V., Cahill, A. G. & Jacobsen, J. D. (2015): Field scale time-domain spectral induced polarization monitoring of geochemical changes induced by injected CO₂ in a shallow aquifer. *Geophysics*: **80**, WA113-WA126.
- Egholm, D. L. (2014). *The Finite Difference Method - Introduction to computational geomodelling*. Lecture notes from Geomodelling, Aarhus University.
- Fiandaca, G., Auken, E., Gazoty, A. & Christiansen, A. V. (2012): Time-domain induced polarization: Full-decay forward modeling and 1D laterally constrained inversion of Cole-Cole parameters. *Geophysics*: **77**, E213-E225.
- Fiandaca, G., Ramm, J., Binley, A., Gazoty, A., Christiansen, A. V., Auken, E. (2013): Resolving spectral information from time domain induced polarization data through 2-D inversion. *Geophysical Journal International*: **192**, 631-646.
- Fraser, D. C., Keevil, N. B. J. & Ward, S. H. (1964): Conductivity spectra of rocks from the Craigmont ore environment. *Geophysics*: **XXIX**, 832-847.
- Gazoty, A., Fiandaca, G., Pedersen, J., Auken, E. & Christiansen, A. V. (2012): Mapping of landfills using time-domain spectral induced polarization data: The Eskelund case study. *Near Surface Geophysics*: **10**, 575-586.
- Gazoty, A., Fiandaca, G., Pedersen, J., Auken, E. & Christiansen, A. V. (2013): Data repeatability and acquisition techniques for Time-Domain spectral Induced Polarization. *Near Surface Geophysics*: **11**, 391-406.

- Ghorbani, A., Camerlynck, C., Florsch, N., Cosenza, P. & Revil, A. (2007): Bayesian inference of the Cole-Cole parameters from time- and frequency-domain induced polarization. *Geophysical Prospecting*: **55**, 589-605.
- Golub, G. H. & Van Loan, C. F. (1996): *Matrix Computations*. Maryland. The Johns Hopkins University Press. 3rd edition.
- Jacobsen, B. H. (2010). *Geophysical Inverse Modelling - Linear and Linearized approaches*. Lecture notes from Introduction to Inversion theory, Aarhus University.
- Kemna, A. (2000): *Tomographic Inversion of Complex Resistivity: Theory and Application*. Thesis, Institut für Geophysik der Ruhr-Universität Bochum.
- Kemna, A., Binley, A., Cassiani, G., Niederleithinger, E., Revil, A., Slater, L., Williams, K. H., Orozco, A. F., Hegel, F.-H., Hördt, A., Kruschwitz, S., Leroux, V., Titov, K. & Zimmermann, E. (2012): An overview of the spectral induced polarization method for near-surface applications. *Near Surface Geophysics*: **10**, 453-468.
- Kemna, A., Binley, A. & Slater, L. (2004): Crosshole IP imaging for engineering and environmental applications. *Geophysics*: **69**, 97-107.
- Malinverno, A. (2002): Parsimonious Bayesian Markov chain Monte Carlo inversion in a nonlinear geophysical problem. *Geophys. J. Int*: **151**, 675-688.
- Marchant, D. (2015): *Induced Polarization Effects in Inductive Source Electromagnetic Data*. Ph.d. thesis, The University of British Columbia.
- Marshak, S. (2007): *Earth – Portrait of a Planet*. Illinois. W. W. Norton & Company. 3rd edition.
- Marshall, D. J. & Madden, T. R. (1959): Induced polarization, a study of its causes. *Geophysics*: **24**, 790-816.
- Metropolis, N., Rosenbluth, M. N., Rosenbluth, A. W. & Teller, A. H. (1953): Equation of state calculations by fast computing machines. *J. Chem. Phys.*: **21**, 1987-1092.
- Olsson, P. I., Dahlin, T., Fiandaca, G. & Auken, E. (2015): Measuring time-domain spectral induced polarization in the on-time: decreasing acquisition time and increasing signal-to-noise ratio. *Journal of Applied Geophysics*: **2015**, 6.
- Pelton, W. H., Rijo, L. & C.M.JR., S. (1978a): Inversion of two-dimensional resistivity and induced-polarization data. *Geophysics*: **43**, 788-803.
- Pelton, W. H., Ward, S. H., Hallof, P. G., Sill, W. R. & Nelson, P. H. (1978b): Mineral discrimination and removal of inductive coupling with multifrequency IP. *Geophysics*: **43**, 588-609.
- Reynolds, J. M. (1997). *An Introduction to Applied and Environmental Geophysics*. John Wiley & Sons Ltd.
- Sambridge, M. & Mosegaard, K. (2002): Monte Carlo Methods in Geophysical Inverse Problems. *Reviews of Geophysics*: **40**.
- Seigel, H. O. (1959): Mathematical Formulation and type curves for induced polarization. *Geophysics*: **24**, 547-565.
- Slater, L. (2007): Near surface electrical characterization of hydraulic conductivity: From petrophysical properties to aquifer geometries - A review. *Surveys in Geophysics*: **28**, 169-197.
- Slater, L. D. & Lesmes, D. (2002): IP interpretation in environmental investigations. *Geophysics*: **67**, 77-88.
- Taranola, A. (2005): *Inverse Problem Theory and Methods for Model Parameter Estimation*. SIAM, Philadelphia. 1st Edition.
- Thorling, L., Brusch, W., Ernsten, V., Hansen, B., Laier, T., Larsen, F., Mielby, S., Sørensen, B. (2015): *Grundvand – Status og udvikling 1989-2013*. GEUS.

- Titov, K., Komarov, V., Tarasov, V. & Levitski, A. (2002): Theoretical and experimental study of time domain-induced polarization in water-saturated sands. *Journal of Applied Geophysics*: **50**, 417-433.
- Vanhala, H. (1997): Mapping oil-contaminated sand and till with the spectral induced polarization (IP) method. *Geophysical Prospecting*: **45**, 303-326.

Appendixes

A.1: Proposer algorithms

A.2: MATLAB scripts

A.3: Comparison of proposer algorithms

A.4: Ghorbani *et al.* (2007)

A.5: Acquisition range

A.6: Three-layer model

A.7: Correlation matrixes

A.8: Field data

Conference abstract

A.1 Proposer algorithms

Two different proposer algorithms have been used in this thesis. The algorithms are implemented into a MCMC code in AarhusInv, where they compute a model proposal for the next model in a Markov chain.

The predefined variables are the step length constant, k , and the maximum perturbation, $MaxStep$, which constrains the length of the steps.

Covariance scaled proposer algorithm

```
!Draw a random number from a normal (Gaussian) distribution for each element in the model vector:
do i=1,N
  perturbation(i)= random_normal
End do
!Compute the perturbation:
perturbation=matmul(L, perturbation)*k
!Constrain the perturbation:
perturbation =min(perturbation,MaxStep)
perturbation=max(perturbation, - MaxStep)
!Compute new model:
mnew(:)=mcurrent(:)+perturbation(:)
```

Figure A.1: Proposer algorithm with a step length constant, k , which is scaled by the linearized estimated covariance matrix by means of the Cholesky decomposition, L . The predefined variables are k and a model perturbation maximum, $MaxStep$. The algorithm is written in Fortran and is implemented in AarhusInv by C. Kirkegaard from Aarhus University.

Gaussian proposer algorithm

```
!Draw a random number from a normal (Gaussian) distribution for each element in the model vector:
do i=1,N
  perturbation(i)= random_normal
End do
!Compute new model:
mnew(:)=mcurrent(:)+perturbation(:)*k
```

Figure A.2: Gaussian proposer algorithm that proposes the next model in a Markov chain, m_{new} . A step length constant, k , must be defined before the algorithm is applied. The algorithm is written as part of this thesis.

A.2 MATLAB scripts

Several MATLAB⁴ scripts have been made in connection with this thesis. The scripts import and plot the output files from the MCMC algorithm in AarhusInv. The scripts are included on the enclosed USB stick together with examples of the file types used for inversion of DCIP data. In the following, the MCMC data files are introduced and three main MATLAB scripts are presented.

MCMC file

When a 1D DCIP dataset has been inverted with the MCMC code, an output file, *.mcmc*, is written. The file contains one row for each iteration completed in the inversion, a column for each Cole-Cole parameters (ρ , m_0 , τ , C and thickness), and a two columns with residuals: A data residual and a total residual which also includes the residual on constrains and prior information.

PlotMCMC.m

The MATLAB script *PlotMCMC.m* loads the *.mcmc* file, computes the standard deviation factors (STDFs), plots the marginal probability distributions for each model layer, plots cross-plots of all the Cole-Cole parameters, and computes the correlation matrix containing the Pearson's correlation coefficient.

Load data

The *.mcmc* file is loaded into MATLAB in the matrix *data*.

Compute standard deviation factors

The \log_{10} is used to impose linearity on the Coe-Cole parameters. The STDFs are computed with the use of the MATLAB function *std*, which computes the standard deviation

$$STDF = 10^{std(\log_{10} data)}.$$

Plot marginal posterior probability distributions and cross-plots

The MATLAB script calls a function, *plotting_mcmc.m*, which plots the marginal posterior probability distribution of each Cole-Cole parameter. The MATLAB function *hist* divides the values of each Cole-Cole parameter into a predefined number of bins and plots them as histograms.

The function *plotting_mcmc.m* also plots the cross-plots of the Cole-Cole parameters. The function *plot2Dhist* is used to divide the 2D cross-plot into a predefined number of bins and calculate how many models fall in each bin. Hereafter, the function *contourf* plots contours of the 2D histograms, which illustrates the probability distributions.

⁴ MATLAB version R2015b. The MathWorks Inc., Natick Massachusetts, 2015.

Correlation matrix

The MATLAB function *corrcoef* computes the Pearson's correlation coefficient of the data matrix. The correlation matrix is plotted with *imagesc*, which puts a color to the values in the matrix.

PlotMCMC_Profile.m

The MATLAB script, *PlotMCMC_Profile.m*, loads the *.mcmc* file and computes the STDFs and the correlation matrix just as *PlotMCMC.m*. The script then plots the distribution of each Cole-Cole parameter in different subplots. The distributions are plotted for all layers of the model in the same plots. The distributions are plotted as density clouds by plotting a see-through line for each model using the function *line* and adding a transparent factor, *alpha*, to the color of the line.

Plot_hisfit.m

The MATLAB script *Plot_hisfits.m* loads the *.mcmc* file and computes histograms for the marginal distributions of the posterior probability and fits a curve to the histograms to show the shape of the distribution. The script calls the MATLAB function *histfit*, which fits the curve to the histograms. A minor change has been made to the function to make the resulting distribution curves comparative even if a different number of models is accepted to the *.mcmc* files. This is done by normalizing the curves by their own integrated volume, so the volume below all curves is one.

A.3 Comparison of proposer algorithms

The figures below show marginal posterior probability distribution of Cole-Cole parameters computed using a covariance scaled and a Gaussian proposer algorithm. The colors indicate how many iterations the MCMC algorithm has made to produce the different distributions. When more iterations are added without changing the shape of the distributions, the Markov chain has converged.

Number of proposed models:

---500 ---50,000 ---5,000,000
---5000 ---500,000 ---50,000,000

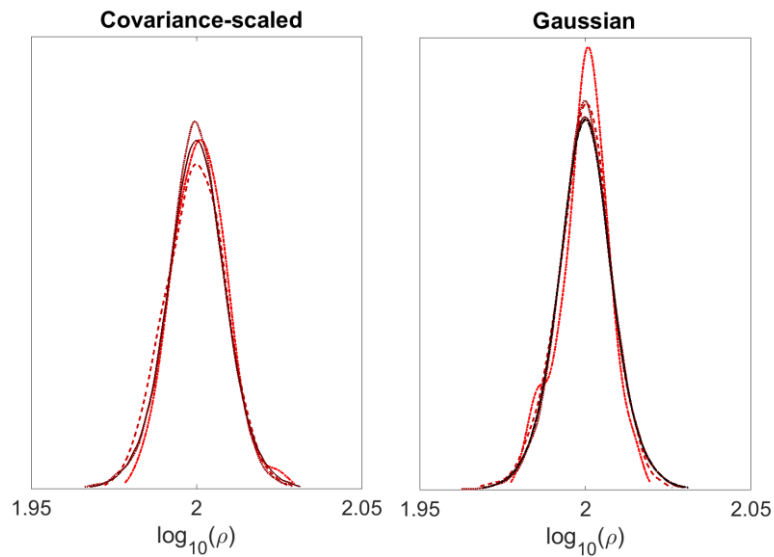


Figure A.3: Marginal probability distribution for the resistivity, ρ [Ωm], computed with two different proposer algorithms: A covariance scaled (left) and a Gaussian proposer (right).

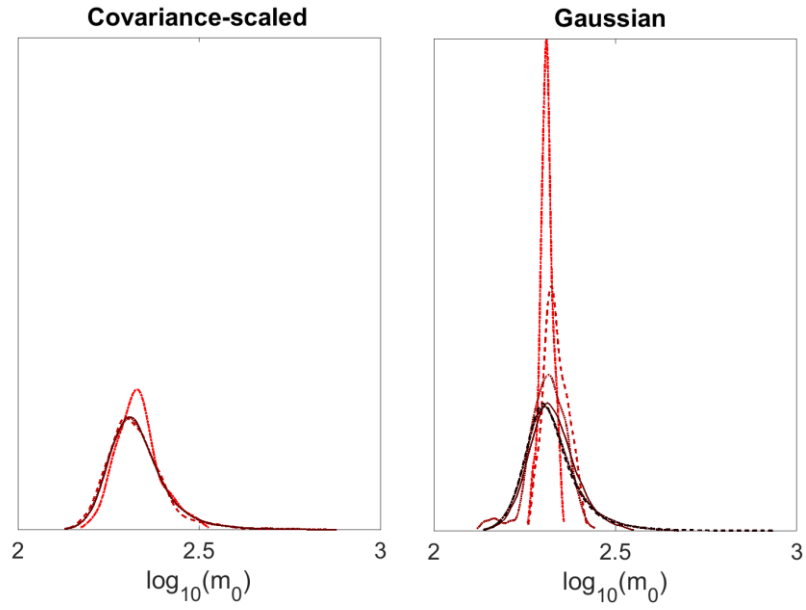


Figure A.4: Marginal probability distribution for the chargeability, m_0 [mV/V], computed with two different proposer algorithms: A covariance scaled (left) and a Gaussian proposer (right). The colors are explained in Figure A.3.

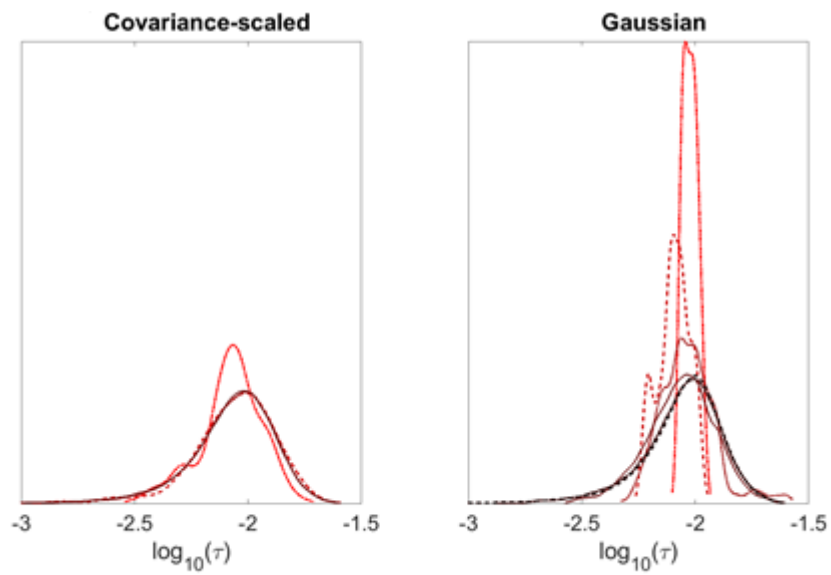


Figure A.5: Marginal probability distribution for the time constant, τ [s], computed with two different proposer algorithms: A covariance scaled (left) and a Gaussian proposer (right). The colors are explained in Figure A.3.

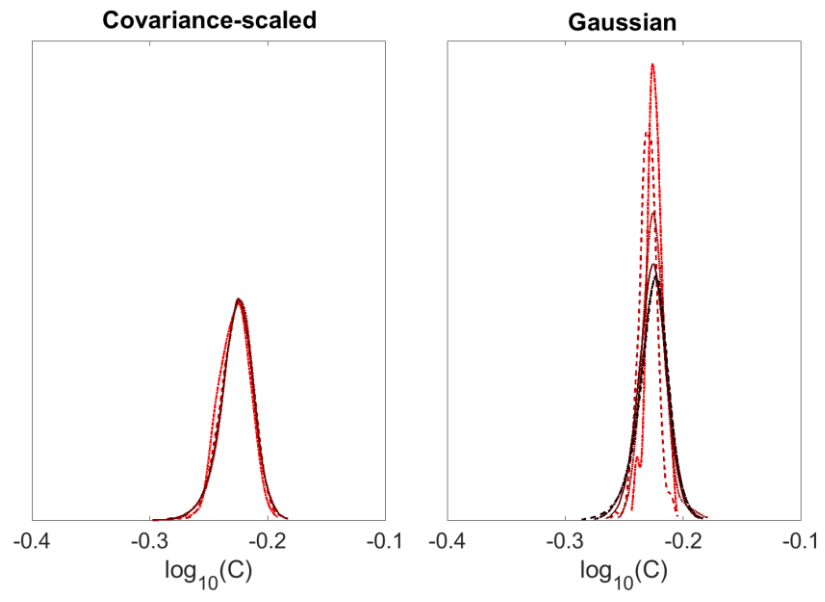


Figure A.6: Marginal probability distribution for the frequency exponent, C , computed with two different proposer algorithms: A covariance scaled (left) and a Gaussian proposer (right). The colors are explained in Figure A.3.

A.4 Ghorbani *et al.* (2007)

The figures below show the results of a MCMC analysis of four models (defined in Table 4.1) previously analyzed by Ghorbani *et al.* (2007). The MCMC results, in terms of the posterior probability distributions, are here compared to the results from Ghorbani. Figure A.7 shows the synthetic forward response of the four models.

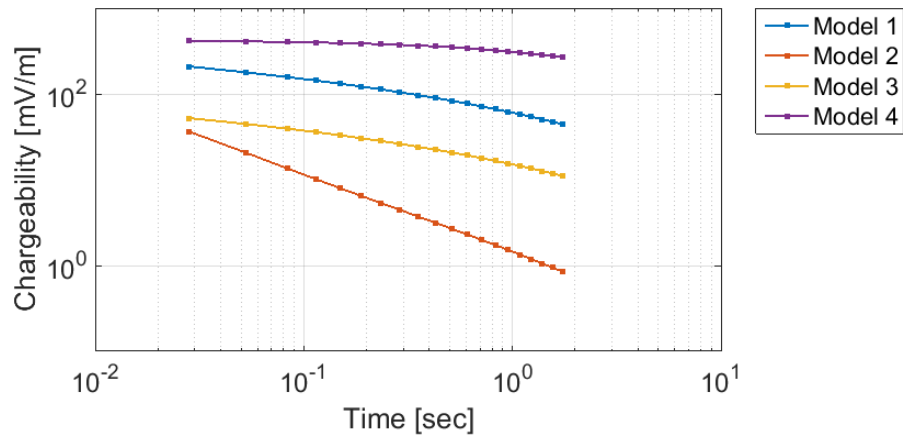
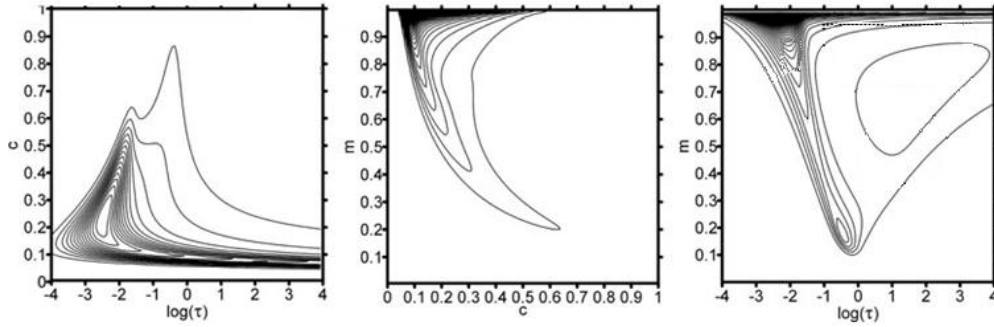


Figure A.7: IP decays for Model 1-4 (Table 4.1). The forward responses are computed in AarhusInv without adding any noise to the synthetic data.

Model 1

The following figure shows the results from Model 1, which has the parameters: $\rho = 100 \Omega\text{m}$, $m_0 = 800 \text{ mV/V}$, $\tau = 0.01 \text{ s}$, and $C = 0.25$.

Results from Ghorbani et al. (2007):



Results from MCMC inversion:

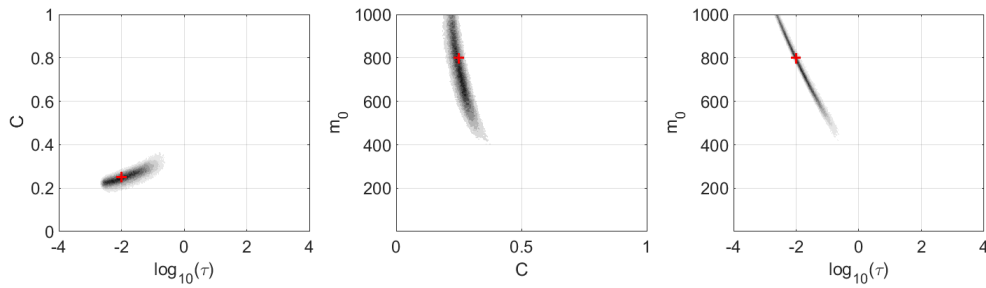


Figure A.8: Comparison of inversion results from Model 1 (Table 4.1) produced by Ghorbani *et al.* (2007) (top) and produced for this thesis (bottom). The red mark is the true model value. τ is presented with the base-10 logarithm for both studies.

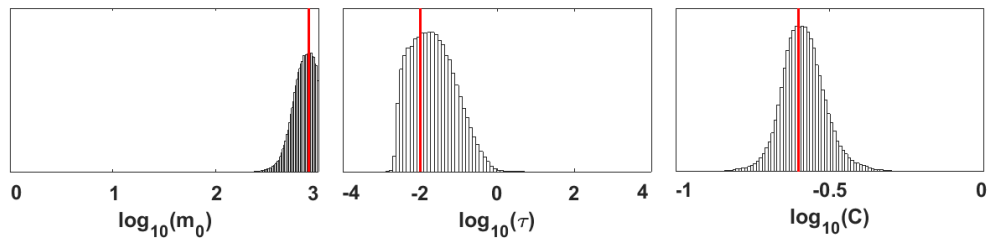
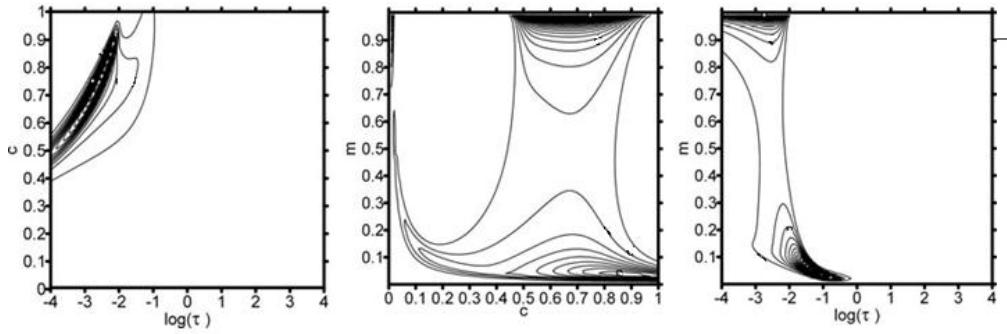


Figure A.9: Marginal posterior probability distributions of Model 1 (Table 4.1) produced with the MCMC algorithm. The red line is the true model value.

Model 2

The following figures show the results from Model 2, which has the parameters: $\rho=100 \Omega$, $m_0=200 \text{ mV/V}$, $\tau=0.01 \text{ s}$, and $C=0.75$.

Results from Ghorbani et al. (2007):



Results from MCMC inversion:

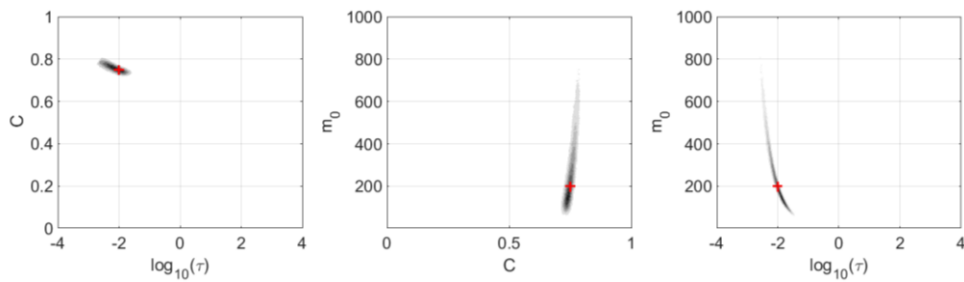


Figure A.10: Comparison of inversion results of Model 2 (Table 4.1) produced by Ghorbani *et al.* (2007) (top) and produced for this thesis (bottom). The red mark is the true model value. τ is presented with the base-10 logarithm for both studies.

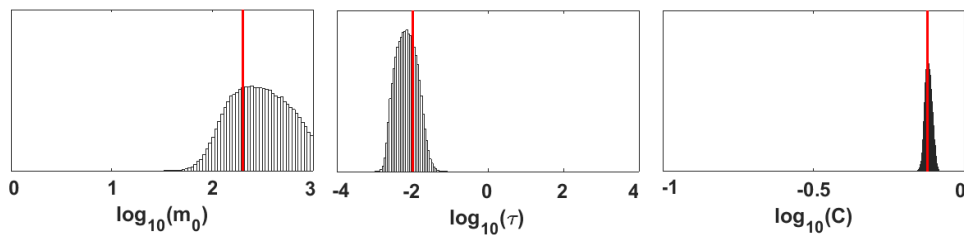
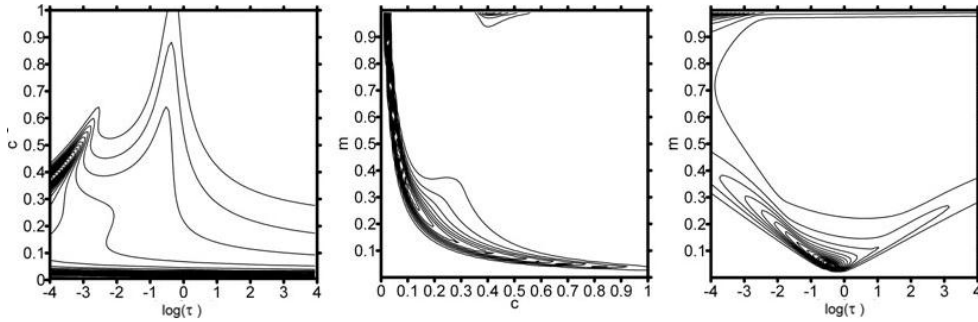


Figure A.11: Marginal posterior probability distributions of Model 2 (Table 4.1) produced with the MCMC algorithm. The red line is the true model value.

Model 3

The following figures show the results from Model 3, which has the parameters: $\rho = 100 \Omega\text{m}$, $m_o = 200 \text{ mV/V}$, $\tau = 0.01 \text{ s}$, and $C = 0.25$.

Results from Ghorbani et al. (2007):



Results from MCMC inversion:

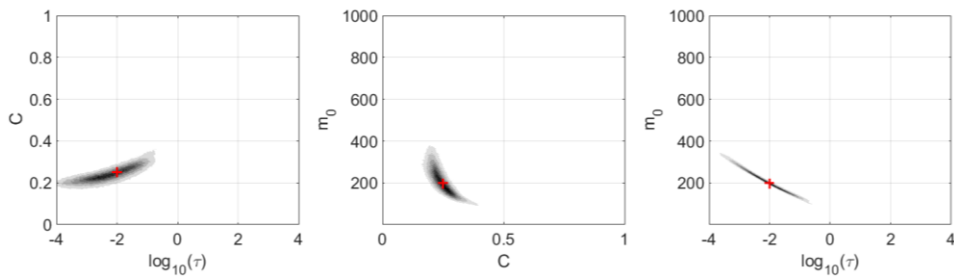


Figure A.12: Comparison of inversion results of Model 3 (Table 4.1) produced by Ghorbani *et al.* (2007) (top) and produced for this thesis (bottom). The red mark is the true model value. τ is presented with the base-10 logarithm for both studies.

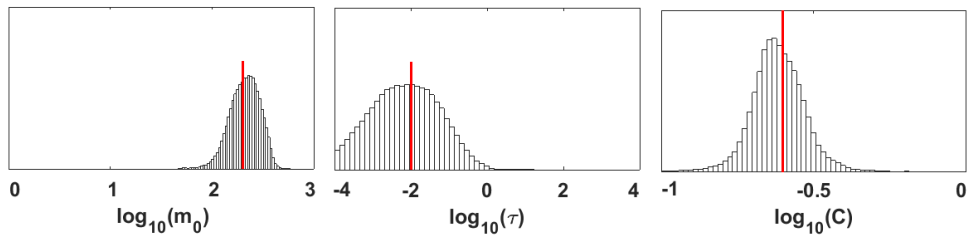
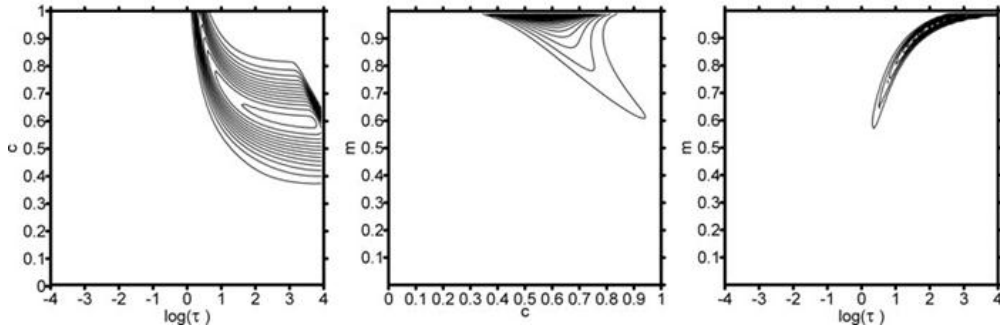


Figure A.13: Marginal posterior probability distributions of Model 3 (Table 4.1) produced with the MCMC algorithm. The red line is the true model value.

Model 4

The following figures show the results from Model 4, which has the parameters: $\rho = 100 \Omega\text{m}$, $m_o = 800 \text{ mV/V}$, $\tau = 10 \text{ s}$, and $C = 0.75$.

Results from Ghorbani et al. (2007):



Results from MCMC inversion:

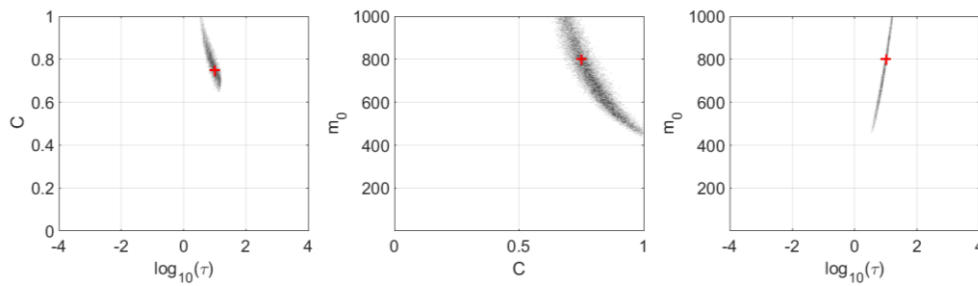


Figure A.14: Comparison of inversion results of Model 4 (Table 4.1) produced by Ghorbani *et al.* (2007) (top) and produced for this thesis (bottom). The red mark is the true model value. τ is presented with the base-10 logarithm for both studies.

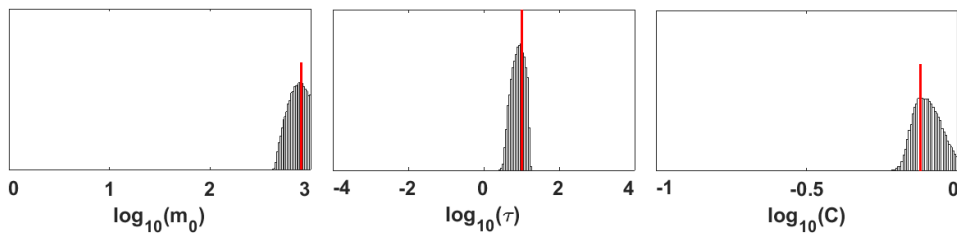


Figure A.15: Marginal posterior probability distributions of Model 4 (Table 4.1) produced with the MCMC algorithm. The red line is the true model value.

A.5 Acquisition range

The figures below are zooms of Figure 5.17 and Figure 5.18 in Section 5.4, which illustrate the consequence of applying different acquisition ranges when measuring DCIP data.

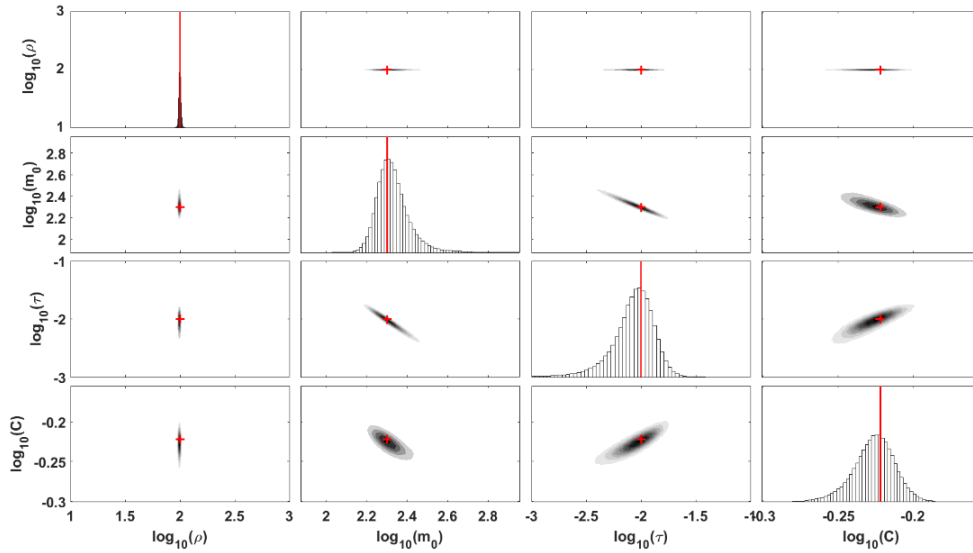


Figure A.16: Enlargement of Figure 5.17. The true model has the parameters: $\rho = 100 \Omega\text{m}$, $m_0 = 200 \text{ mV/V}$, $\tau = 0.01 \text{ s}$, and $C = 0.6$. See reference figure for further descriptions.

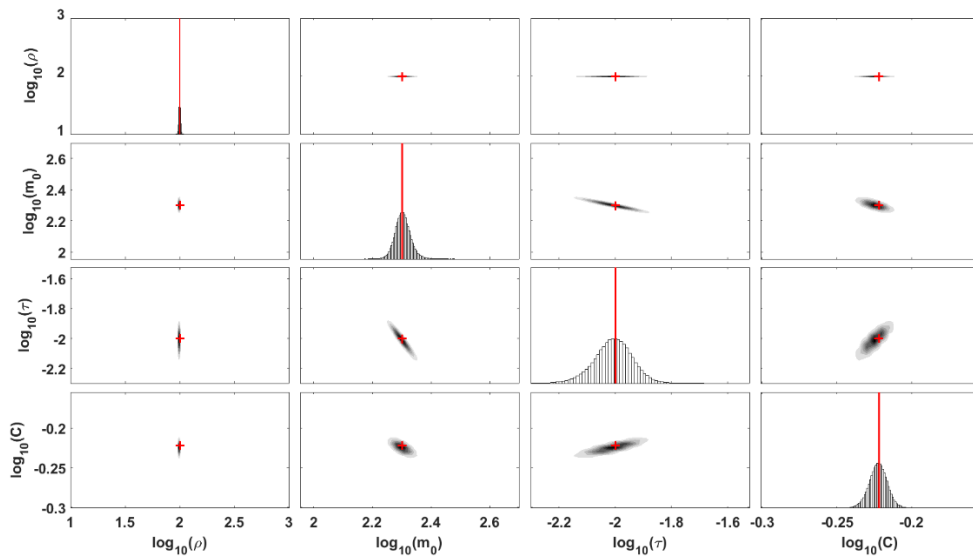


Figure A.17: Enlargement of Figure 5.18. The true model has the parameters: $\rho = 100 \Omega\text{m}$, $m_0 = 200 \text{ mV/V}$, $\tau = 0.01 \text{ s}$, and $C = 0.6$. See reference figure for further descriptions.

A.6 Three-layer model

Synthetic data were generated from the three-layer model described in Table 4.4. The dataset was then inverted with three different settings. The results are described in Model A, Model B and Model C below.

Model A: Marginal distributions

Model A was inverted with the standard gate settings described in Table 3.2. The main results are presented in Section 5.5.1, but shown here is a zoom of the posterior probability distributions of the Cole-Cole parameters. Figure A.18 shows the marginal distributions of all three layers with the same scaling, so the distributions can be compared. Zooms of the distributions together with the cross-plots between the Cole-Cole parameters are presented for layer one, two and three in Figure A.19, Figure A.20, and Figure A.21 respectively.

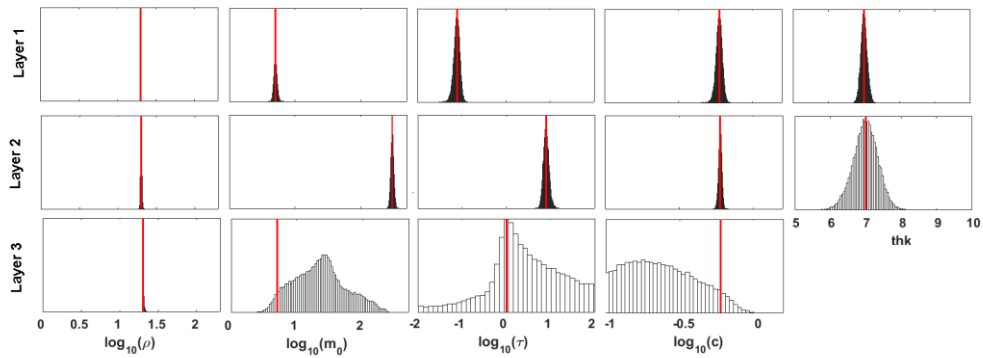


Figure A.18: Marginal posterior probability distributions of the Cole-Cole parameters (ρ [Ωm], m_0 [mV/V], τ [s], C [-], and thickness, thk [m]) of a three-layer model, Model A, described in Table 4.4. The red line is the true model value.

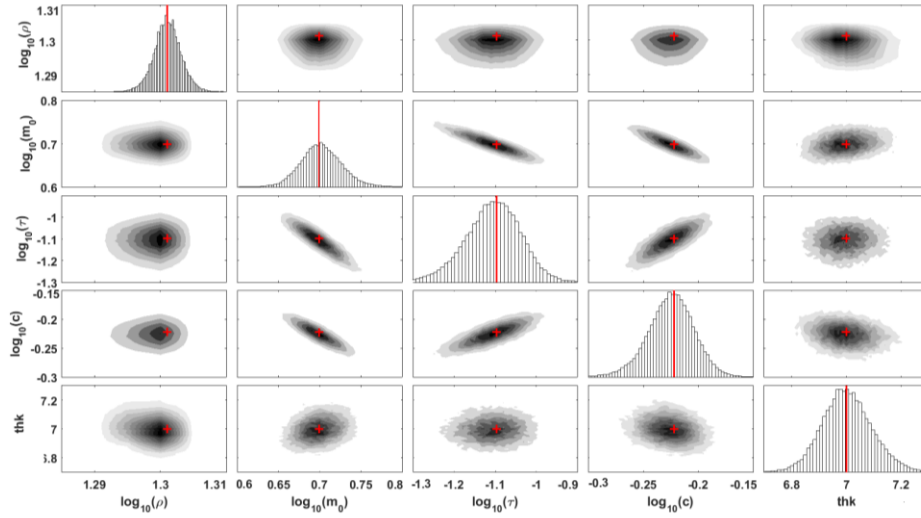


Figure A.19: Posterior probability distributions of the Cole-Cole parameters (ρ [Ωm], m_0 [mV/V], τ [s], C [-], and thickness, thk [m]) of layer one in Model A (Table 4.4). The diagonal shows the marginal distributions and the off-diagonals are the cross-plot between the parameters. The true model is indicated in red.

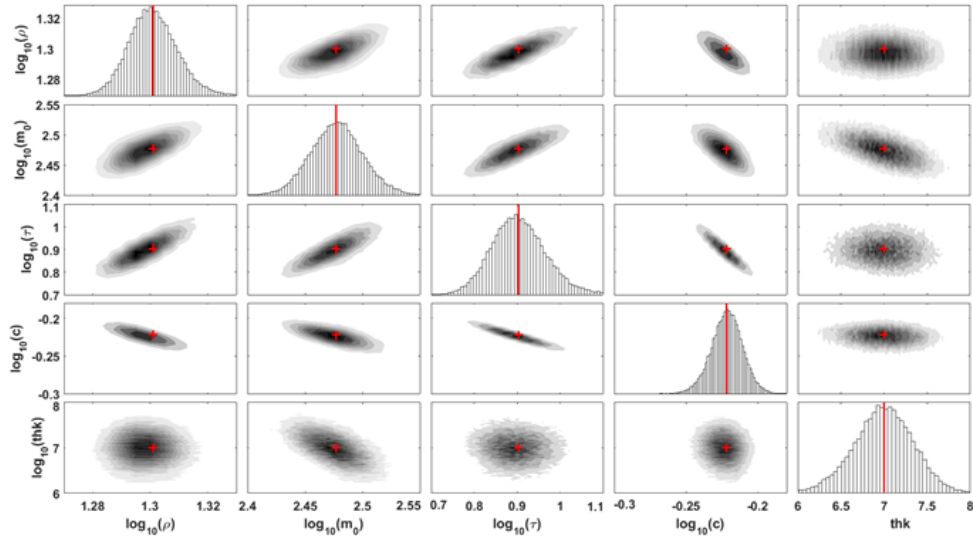


Figure A.20: Posterior probability distributions of the Cole-Cole parameters (ρ [Ωm], m_0 [mV/V], τ [s], C [-], and thickness, thk [m]) of layer two in Model A (Table 4.4). The diagonal shows the marginal distributions and the off-diagonals are the cross-plot between the parameters. The true model is indicated in red.

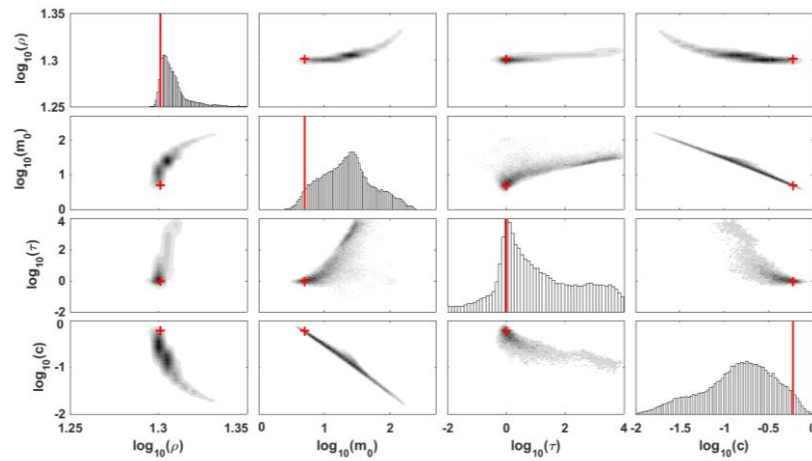


Figure A.21: Posterior probability distributions of the Cole-Cole parameters (ρ [Ωm], m_0 [mV/V], τ [s], and C [-]) of layer three in Model A (Table 4.4). The diagonal shows the marginal distributions and the off-diagonals are the cross-plot between the parameters. The true model is indicated in red.

Model B: Small C

The posterior probability densities of Model B are shown in Figure A.22, the correlation matrix in Figure A.23, and the computed standard deviation factors in Table A.1.

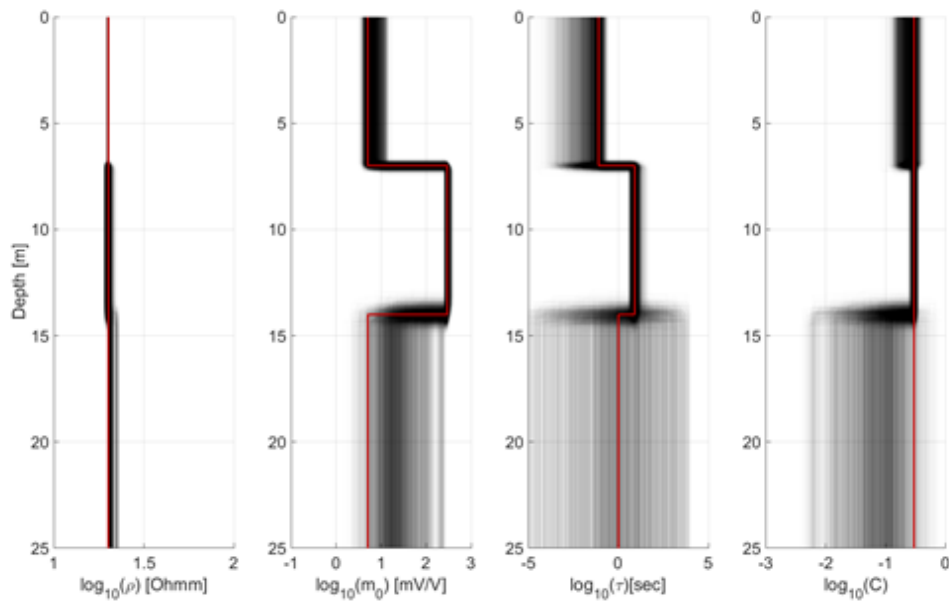


Figure A.22: Posterior probability densities of the Cole-Cole parameters of the three-layer model, Model B (Table 4.4). The red line is the true model.

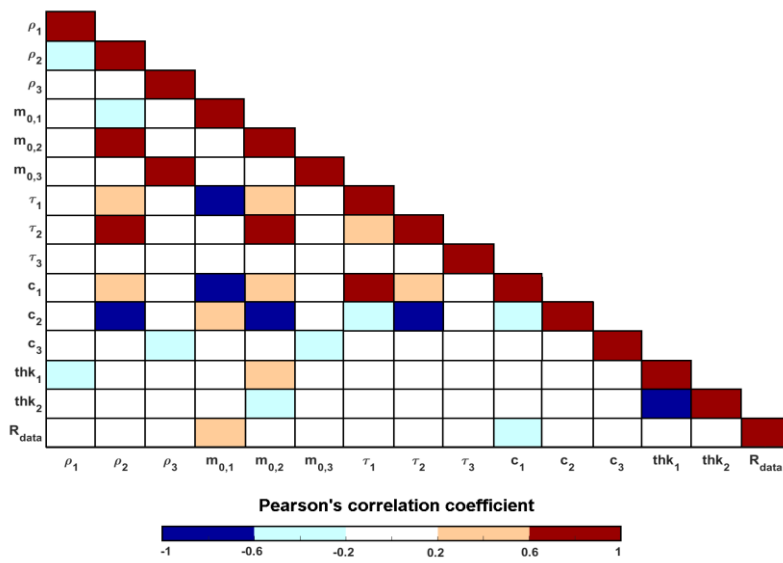


Figure A.23: Correlation matrix for Model B (Table 4.4). Red colors indicate a positive correlation between the Cole-Cole parameters and the blue colors indicate a negative correlation.

	<i>STDF</i> (ρ)	<i>STDF</i> (m_0)	<i>STDF</i> (τ)	<i>STDF</i> (C)	<i>STDF</i> (thk)
Layer 1	1.00	1.37	5.46	1.31	1.01
Layer 2	1.02	1.07	1.43	1.06	1.06
Layer 3	1.02	2.67	159.82	2.78	

Table A.1: Standard deviation factors (STDFs) computed from the MCMC inversion results of Model B (Table 4.4).

Model C: Small acquisition range

The posterior probability densities of Model C are shown in Figure A.24, the correlation matrix in Figure A.25, and the computed standard deviation factors in Table A.2.

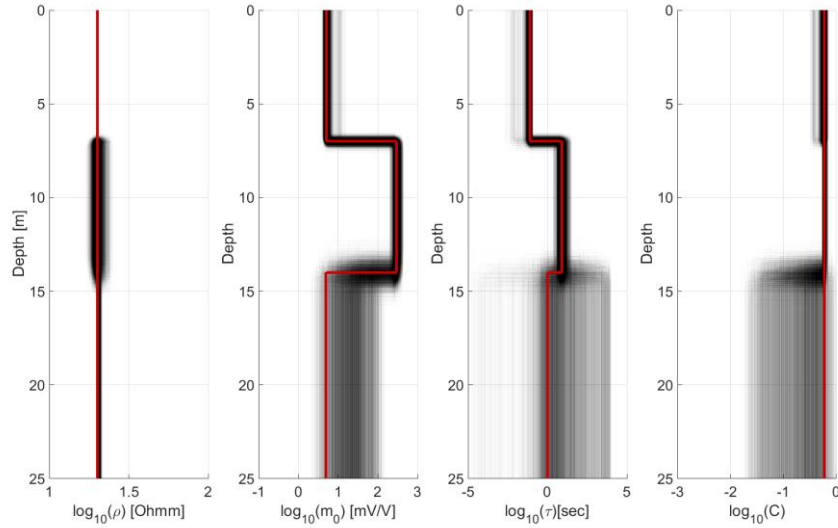


Figure A.24: Posterior probability densities of the Cole-Cole parameters of the three-layer model, Model C (Table 4.4). The red line is the true model.

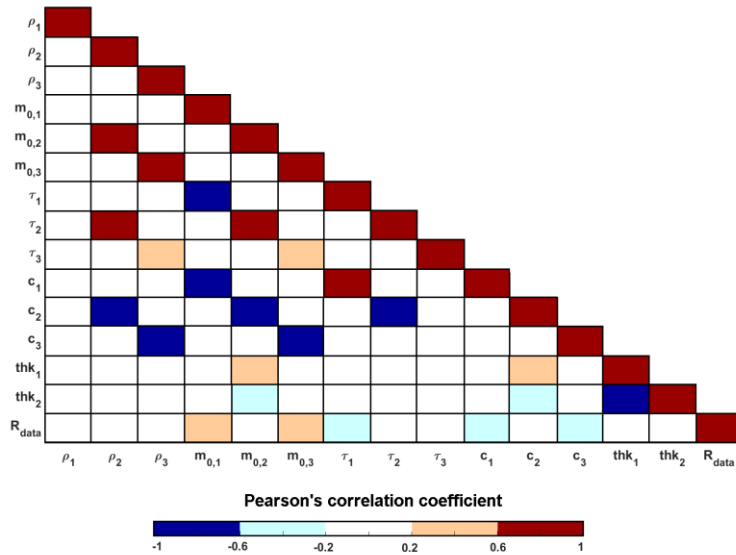


Figure A.25: Correlation matrix for Model C (Table 4.4). Red colors indicate a positive correlation between the Cole-Cole parameters and the blue colors indicate a negative correlation.

	STDF(ρ)	STDF(m_0)	STDF(τ)	STDF(C)	STDF(thk)
Layer 1	1.00	1.18	1.55	1.11	1.02
Layer 2	1.06	1.14	1.55	1.04	1.09
Layer 3	1.01	2.40	35.41	2.57	

Table A.2: Standard deviation factors (STDFs) computed from the MCMC inversion results of Model B (Table 4.4).

A.7 Correlation matrixes

In the following, correlation matrixes of the MCMC inversions results presented in Section 5.7 are shown. The results are used in the discussion of this thesis, where the aim is to find general tendencies in the correlations of the Cole-Cole parameters.

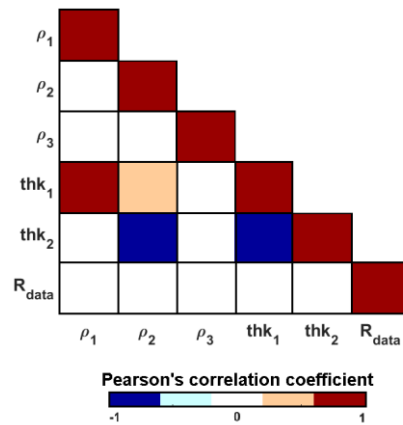


Figure A.26: Correlation matrix for the Cole-Cole parameters determined from Figure 5.36, which is a DC inversion result of a model with a high resistivity equivalence. The matrix holds the correlation coefficients between all the Cole-Cole parameters. Blue colors indicate an anti-correlation and red colors a positive correlation.

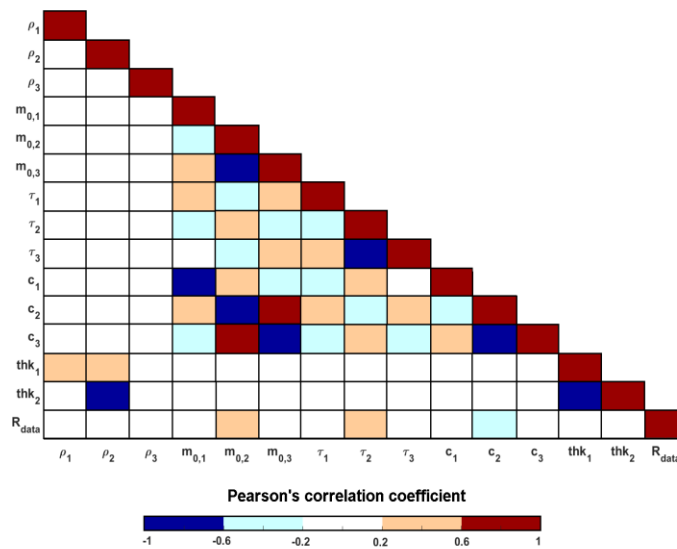


Figure A.27: Correlation matrix for the Cole-Cole parameters determined from Figure 5.37, which is a DCIP inversion result of a model with a high resistivity equivalence. The matrix holds the correlation coefficients between all the Cole-Cole parameters. Blue colors indicate an anti-correlation and red colors a positive correlation.

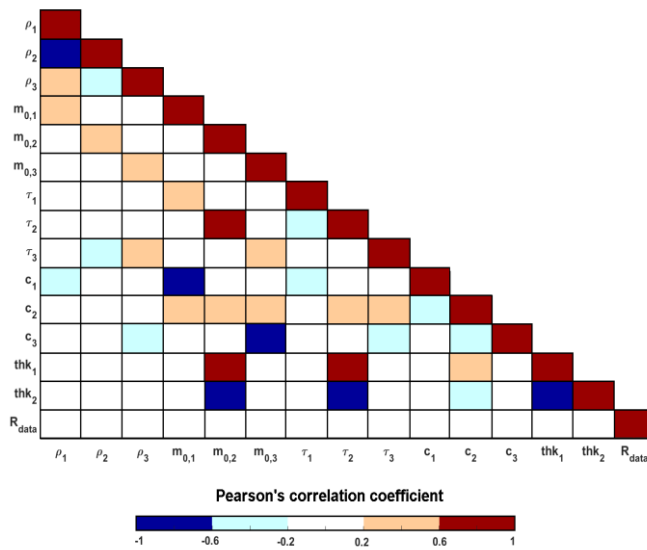


Figure A.28: Correlation matrix for the Cole-Cole parameters determined from Figure 5.38, which is a three-layer model with the Cole-Cole parameters: $\rho = 20 \Omega m$, $m_0 = [50, 500, 50] \text{ mV/V}$, $\tau = 1 \text{ s}$, and $C = 0.6$. The matrix holds the correlation coefficients between all the Cole-Cole parameters. Blue colors indicate an anti-correlation and red colors a positive correlation

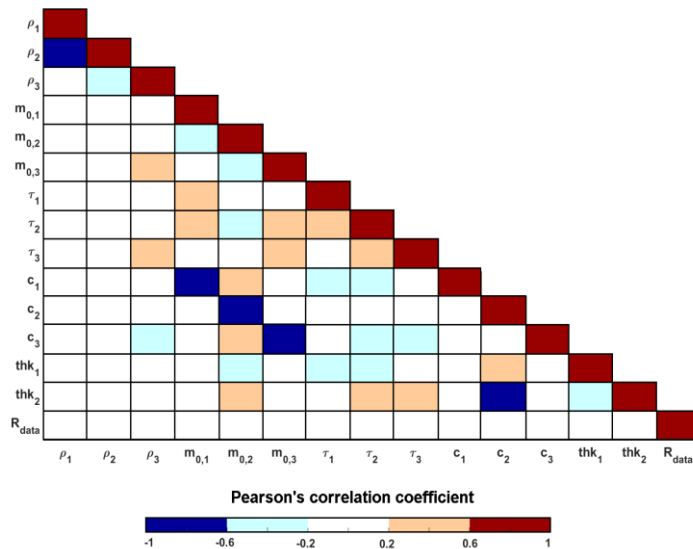


Figure A.29: Correlation matrix for the Cole-Cole parameters determined from Figure 5.40, which is a three-layer figure with the Cole-Cole parameters: $\rho = 20 \Omega m$, $m_0 = 50 \text{ mV/V}$, $\tau = [1, 0.1, 1] \text{ s}$, and $C = 0.6$. The matrix holds the correlation coefficients between all the Cole-Cole parameters. Blue colors indicate an anti-correlation and red colors a positive correlation

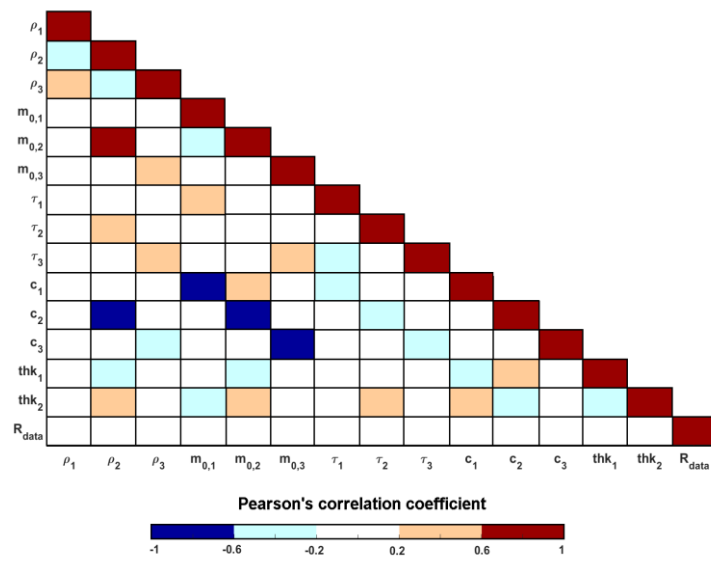


Figure A.30: Correlation matrix for the Cole-Cole parameters determined from Figure 5.42, which is a three-layer model with the Cole-Cole parameters: $\rho = 20 \Omega m$, $m_0 = 50 \text{ mV/V}$, $\tau = 0.1 \text{ s}$, and $C = [0.6, 0.1, 0.6]$. The matrix holds the correlation coefficients between all the Cole-Cole parameters. Blue colors indicate an anti-correlation and red colors a positive correlation

A.8 Field data

A 2D DCIP dataset has been measured at Samsø as part of the GEOCON project. A 1D model is taken from the dataset and inverted with four layers with the MCMC algorithm. The figures below show the marginal posterior probability distributions and cross-plot of the Cole-Cole parameters.

Figure A.31 shows the distributions of all four layers with the same scaling, so the uncertainties of the distribution can be compared. Figure A.32 to Figure A.35 show the enlarged distributions of each layer together with the cross-plots of the Cole-Cole parameters.

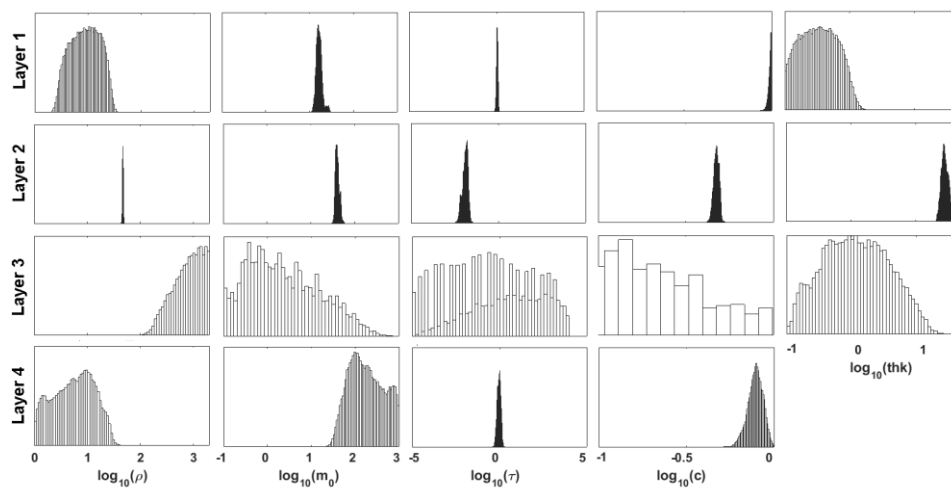


Figure A.31: Marginal posterior probability distributions of the Cole-Cole parameters (ρ [Ωm], m_0 [mV/V], τ [s], C [-], and thickness, thk [m]) for a four-layer model. The results are obtained from MCMC inversion of filed data from Samsø.

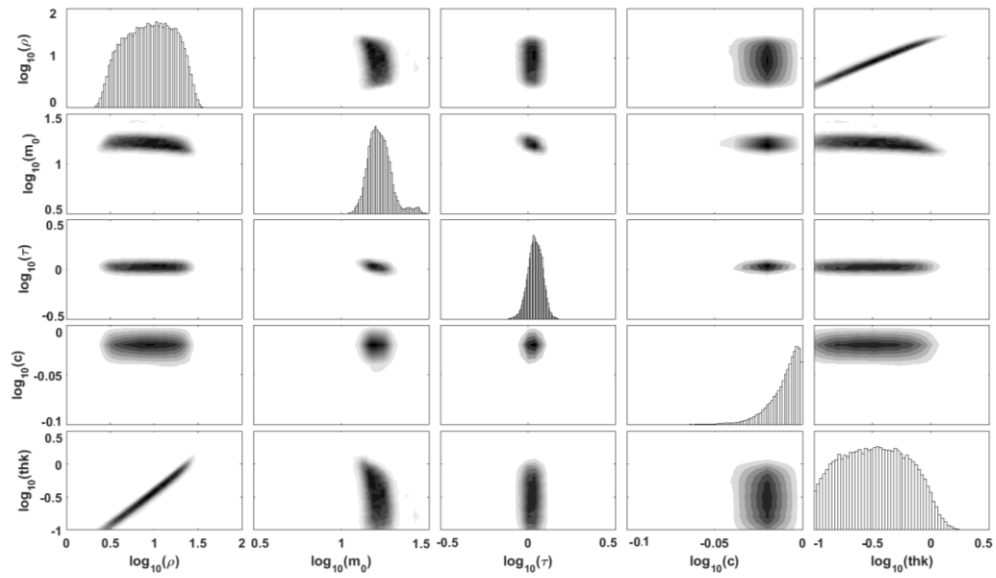


Figure A.32: MCMC inversion results of layer one from field data from Samsø. The diagonals show the marginal posterior probability distributions of the Cole-Cole parameters (ρ [Ωm], m_0 [mV/V], τ [s], C [-], and thickness, thk [m]) and the off-diagonals are the density of the cross-plots.

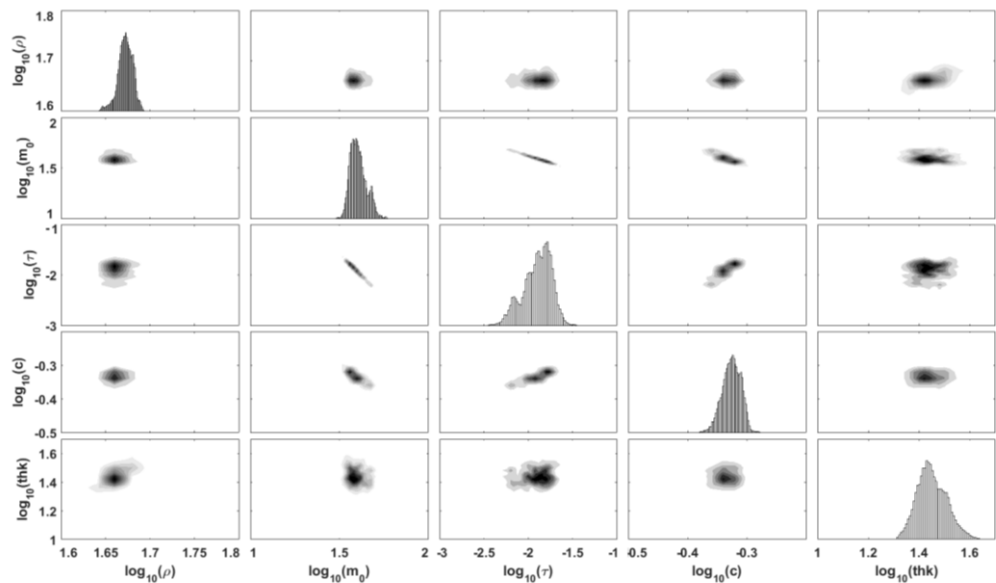


Figure A.33: MCMC inversion results of layer two from field data from Samsø. The diagonals show the marginal posterior probability distributions of the Cole-Cole parameters (ρ [Ωm], m_0 [mV/V], τ [s], C [-], and thickness, thk [m]) and the off-diagonals are the density of the cross-plots.

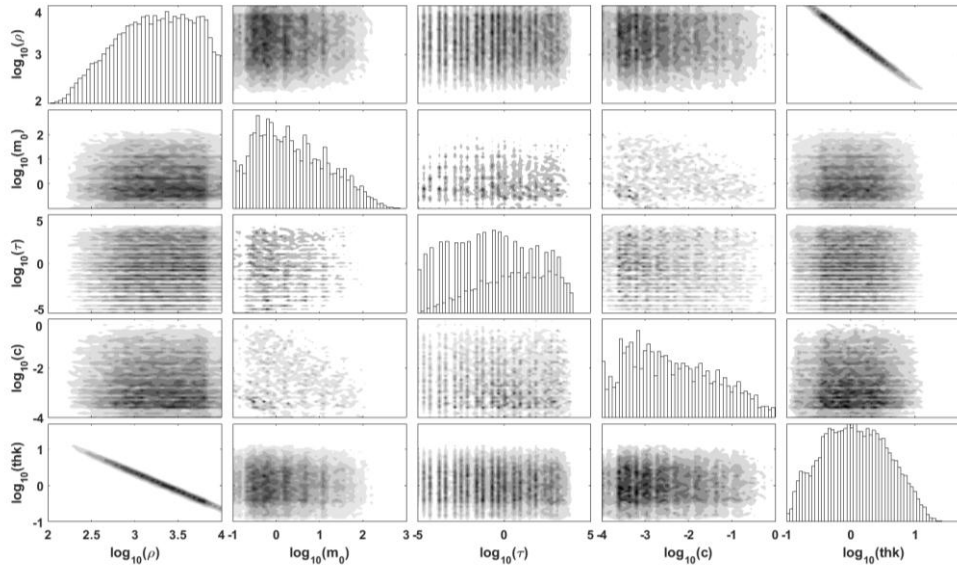


Figure A.34: MCMC inversion results of layer three from field data from Samsø. The diagonals show the marginal posterior probability distributions of the Cole-Cole parameters (ρ [Ωm], m_0 [mV/V], τ [s], C [-], and thickness, thk [m]) and the off-diagonals are the density of the cross-plots.

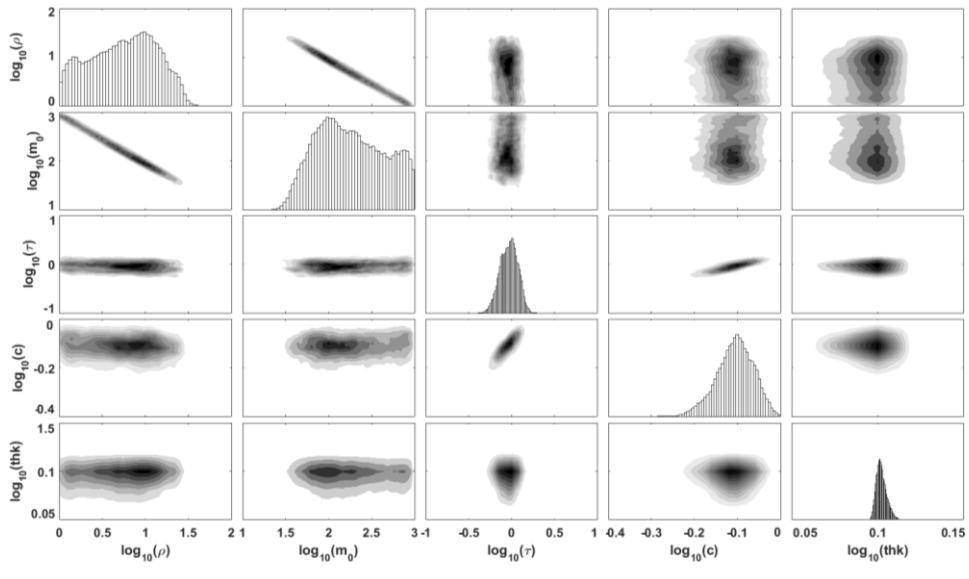


Figure A.35: MCMC inversion results of layer four from field data from Samsø. The diagonals show the marginal posterior probability distributions of the Cole-Cole parameters (ρ [Ωm], m_0 [mV/V], τ [s], C [-], and thickness, thk [m]) and the off-diagonals are the density of the cross-plots.

Conference abstract

Madsen, L. M., Kirkegaard, C., Fiandaca, G., Christiancen, A. V., Auken, E.. (2016): An Analysis of Cole-Cole parameters for IP data using Markov chain Monte Carlo. Proceedings for the 4th International Workshop on Induced Polarization, Aarhus, Denmark 2016.